PACIFIC EARTHQUAKE ENGINEERING RESEARCH CENTER

Models for the Cyclic Resistance of Silts and Evaluation of Cyclic Failure during Subduction Zone Earthquakes

Armin W. Stuedlein
Ali Dadashiserej
Amalesh Jana

School of Civil and Construction Engineering
Oregon State University, Corvallis, Oregon

PEER Report No. 2023/01

Pacific Earthquake Engineering Research Center
Headquarters at the University of California, Berkeley

PEER 2023/01
April 2023

Models for the Cyclic Resistance of Silts and Evaluation of Cyclic Failure during Subduction Zone Earthquakes

Armin W. Stuedlein

Ali Dadashiserej

Amalesh Jana

School of Civil and Construction Engineering
Oregon State University, Corvallis, Oregon

PEER Report 2023-01
Pacific Earthquake Engineering Research Center
Headquarters at the University of California, Berkeley
April 2023

ABSTRACT

This report describes several advances in the cyclic failure assessment of silt soils with immediate and practical benefit to the geotechnical earthquake engineering profession. First, a database of cyclic loading test data is assembled, evaluated, and used to assess trends in the curvature of the *CRR-N* (cyclic resistance ratio - the number of equivalent cycles) relationship. This effort culminated in a plasticity index-dependent function which can be used to estimate the exponent *b* in the power law describing cyclic resistance, and may be used to estimate the cyclic resistance of silt soils as well as the number of equivalent loading cycles anticipated for subduction zone earthquakes. Statistical models for the cyclic resistance ratio and cyclic strength ratio are presented in this report. The SHANSEP (Stress History and Normalized Soil Engineering Properties)-inspired functional form of these models have been trained and tested against independent datasets and finalized using a combined dataset to provide reasonable estimates of resistance based on the available data. These models can be used to provide provisional estimates of the *CRR-N* and cyclic strength ratio power laws for cyclic shear strain failure criteria ranging from 1 to 10%, within certain stated limitations.

The ground motion records within the NGA Subduction Project which have been released to the public to-date are implemented to examine the role of subduction zone earthquake characteristics on the number of equivalent loading cycles for a wide range of soils with exponents *b* ranging from 0.05 (moderate plasticity silt and clay) to 0.35 (dense sand). This analysis shows that the number of loading cycles for a given magnitude subduction zone earthquake is larger than those previously computed, whereas the corresponding magnitude scaling factors for use with the Simplified Method span a smaller range as a result of the ground motion characteristics. Owing to the large variability in the computed equivalent number of loading cycles, consideration of the uncertainty is emphasized in forward analyses.

The work described herein may be used to estimate cyclic resistance of intact non-plastic and plastic silt soils and corresponding factor of safety against cyclic failure for a range in cyclic shear strain failure criteria, to plan cyclic laboratory testing programs, and to calibrate models for use in site response and nonlinear deformation analyses in the absence of site-specific cyclic test data. As with any empirical approach, the models presented herein should be revised when additional, high-quality cyclic testing data become available.

Keywords: silts, cyclic failure, cyclic softening, liquefaction, cyclic resistance, subduction zone earthquakes

ACKNOWLEDGMENTS AND DISCLAIMER

This research study was funded by the Pacific Earthquake Engineering Research (PEER) Center, under Contract No. 1175-NCTRSA. Additional research funding and in-kind contributions to this study were provided by the Cascadia Lifelines Program (CLiP) and its member agencies, the Oregon Department of Transportation (ODOT), the Port of Portland (PoP), both of which are CLiP Member Agencies, and the National Science Foundation (NSF) which supported a portion of this work through Grant No. CMMI 1663654.

Much of the data developed by the authors is available for download using the collection of Jupyter notebook tools, *ngl_tools*, available at DesignSafe-CI at https://www.designsafe-ci.org/rw/user-guides/tools-applications/hazard-apps/next-generation-liquefaction/. Additional data will be made available through this web portal as refinements to the NGL databases continue.

Professor T. Matthew Evans contributed significantly to many of the supporting studies forming the basis for this work and has provided valuable review comments regarding portions of this study; his contributions are warmly acknowledged. We also thank the individuals who have helped to facilitate this work, including Tom Wharton, P.E., Susan Ortiz, P.E., G.E., and Dr. Kira Glover-Cutter. The authors thank Sam Christie, P.E., G.E. of Kleinfelder, Inc., for use of available cyclic testing data produced to, and Dr. Sam Sideras of Shannon & Wilson, Inc., for use of data generated at Oregon State University in, support of civil infrastructure project requirements. The authors also thank Jonathan P. Stewart of the University of California, Los Angeles for helpful discussions regarding the role of ground motion characteristics on equivalent loading cycles, which informed the ground motion record screening procedures reflected herein.

This report was revised June 2023 to remove an incorrect statement regarding the development of Eq. (5.9) and improve the description of the basis for development. The regression model for the cyclic strength ratio was trained on cyclic strengths corrected to a loading frequency of 1 Hz.

CONTENTS

LIST OF TABLES

LIST OF FIGURES

1 INTRODUCTION

1.1 OVERVIEW

Despite the previous recognition that cyclically-induced strength loss is possible for non-plastic to plastic silts and plastic clays, the factors associated with the assessment of liquefaction or cyclic softening of these materials has received less attention relative to liquefaction phenomena of non-plastic granular soils. The scale of damage possible due to liquefaction-induced ground failure may have served to draw greater attention to improving liquefaction triggering models and the corresponding consequences. Yet, cyclic softening of silts and clays may also lead to catastrophic damage, as observed in the 1999 Kocaeli and 1999 Chi Chi earthquakes (Bray and Sancio 2006; Chu et al. 2008). Non-plastic silts and low to moderate plasticity silts and clays are commonly found in population centers which naturally tend to form along rivers and within the corresponding alluvial floodplains. In many seismically-active regions, the alluvium is characterized as young to moderately-aged and sensitive to seismic loading. Such is the case for Western Oregon and Southwest Washington within the Willamette and Columbia River valleys, in addition to the coastal estuaries and deltas along the Washington and Oregon coasts and the Puget Sound Lowlands. Significant development has occurred within and along these areas of Oregon and Washington, and the determination of the cyclic resistance of these soils represents a high priority given the potential for economic loss following a Cascadia Subduction Zone interface earthquake or rupture of the crustal faults identified in the US Geological Survey National Seismic Hazard Maps.

A long-range study of the seismic response of the silts distributed within Western Oregon and Southwest Washington, initiated at Oregon State University, has developed sufficient cyclic testing data of silts carefully retrieved from sites distributed throughout the region, and coupled with available data in the literature and provided by industry partners, to serve as the basis for models that facilitate estimation of the cyclic resistance of these materials in the absence of site-specific laboratory test data. These models will assist in providing the practitioner with preliminary estimates of seismic risk due to liquefaction or cyclic softening, planning of site-specific laboratory cyclic testing, and calibration of site response and numerical deformation analyses. Further, the Next Generation Attenuation (NGA) Subduction Project database of ground motions also allows for revisiting magnitude scaling factors for both liquefaction triggering and cyclic softening assessments, as well as determination of the number of equivalent cycles associated with subduction zone earthquakes of given magnitude, the latter of which is critical for direct and indirect assessments of *cyclic failure* as described in this report. Seismically-induced liquefaction is fundamentally linked to the generation of excess pore pressure, u_e, equal in magnitude to the mean effective stress, p', though commonly set equal to the vertical effective stress, σ'_{v0}, acting on a given "element" of soil within a deposit. A significant portion of the intact silt specimens studied in this report exhibited liquefaction at large shear strains, where u_e exceeded 95% of the vertical effective consolidation stress, σ'_{vc}, acting on the specimen and demonstrated a corresponding loss of shear stiffness to zero or near-zero minimum tangent shear modulus during cyclic shear (Stuedlein et al. 2023). However, this report does not differentiate between those specimens which exhibited liquefaction or cyclic softening, but rather focuses on the cyclic resistance offered by a specimen with its corresponding material and state characteristics at a given shear strain amplitude (i.e., a pre-defined cyclic failure criterion). The magnitude of excess pore pressure is of less interest than the potential deformation that might be associated with given loading intensity (i.e., the cyclic stress ratio) and duration (i.e., the number of uniform loading cycles). We have therefore adopted the term *cyclic failure* to describe the number of cycles associated with a given shear strain amplitude at a given intensity, irrespective of the hysteretic characteristics which might be associated with particular mode of cyclic response (e.g., liquefaction, cyclic softening).

The reader should recognize that our understanding of silt responses to ground motions will continue to evolve as additional laboratory cyclic test and case history data become available and the models proposed herein refined. Finally, no model should be viewed as a substitute for site-specific testing when design evaluations for critical infrastructure are of concern. Although the uncertainty in the proposed models has been characterized and the ranges in independent variables where data is scarce identified, it is critical to recognize early in the design process where cyclic failure may pose a concern and engage in laboratory investigations to increase the understanding of the consequences of a given seismic hazard.

1.2 ORGANIZATION OF THIS REPORT

This report is organized into seven sections and three appendices. Section 2 introduces the laboratory test program undertaken on specimens retrieved from thin-walled tubes at sites where silt soils were present. Section 3 presents the results of oedemetric compression tests conducted to determine the stress history, monotonic, constant-volume, shear strength under the direct simple shear stress path and interpreted within the SHANSEP framework, and representative cyclic direct simple shear tests to quantify the stress-controlled, constant volume, cyclic resistance of soil samples. Section 4 describes the database used for preliminary training and testing of statistical models, and developing models to estimate the cyclic resistance ratio and cyclic strength ratio of silty soils, and a parameter that dictates the number of equivalent loading cycles for a given earthquake magnitude, presented in Section 5.

Section 6 leverages the recently released NGA Subduction Project database of ground motions suitable for use with seismic hazards of the Cascadia Subduction Zone to propose new magnitude scaling factors and corresponding equivalent number of cycles for earthquake magnitudes ranging from 6.0 to 9.12. Section 6 also discusses how the statistical models and equivalent number of cycles proposed in Sections 5 and 6, respectively, can be used in engineering practice for the purpose of design level evaluations, guiding site-specific laboratory cyclic testing, and conducting preliminary site response and numerical deformation analyses. Examples are provided describing how cyclic failure assessments may be conducted within the general Simplified Method framework. Section 7 concludes this report and is followed by the bibliography and supporting appendices.

2 LABORATORY TESTING PROGRAM

2.1 CYCLIC DIRECT SIMPLE SHEAR APPARATUS

The SSH-100 monotonic and cyclic direct simple shear (DSS) device manufactured by Geotechnical Consulting and Testing Systems (GCTS) was used in this study. This testing system consists of hydraulically-actuated servo-controlled shear and normal load actuators and pneumatically servo-controlled cell and back pressures. Due to the general use of constant-volume testing without back-pressure saturation, described by Dyvik et al (1987), Jana and Stuedlein (2021), and Dadashiserej et al. (2022a), a pressure cell was not used in the monotonic and cyclic DSS tests. The device has a fixed top cap and a sliding bottom base mounted on low-friction linear bearings. The normal and shear loads are applied through a pair of specially-designed aluminum loading frames. The apparatus can test cylindrical specimens with diameter of 70 mm confined with a series of stacked rings which restricts lateral deformation of the specimen during the test.

The cyclic DSS apparatus in this study is outfitted with a pair of bender element (BE) and piezoelectric disc (PD) transducers for body wave measurements (compression wave, V_p; shear wave, V_s). V_p measurement provides an indirect indication of the degree of saturation, S_r, for comparison to *in-situ* conditions, whereas V_s measurements allow evaluation of specimen quality and monitoring of changes to soil fabric following sampling and shearing (Landon et al. 2007, El Sekelly et al. 2016, Jana and Stuedlein 2021, Dadashiserej et al. 2022b).

2.2 CHARACTERIZATION OF SILT SPECIMENS

A comprehensive laboratory testing program was conducted on intact specimens prepared from thin-walled tube samples obtained from seven different tests sites (i.e., A, B, C, D, E, F, and G) as summarized in Table 2.1. The soils from Sites A, B, D, E, and F were described by Stuedlein et al. (2023), whereas soils from Sites C and G were developed by the authors for industry partners to support project requirements. In order to extend the existing dataset, cyclic test results provided by different geotechnical consulting firms on intact soils from three different sites were reviewed and included in the dataset (i.e., Sites H, I, and J; Table 2.1). Specimens were cyclically loaded using a frequency of 0.1 Hz, except Test Series I (f = 1 Hz); the *CRR*s for this test series were therefore corrected to 0.1 Hz to provide a common basis for model development by reducing the *CRR* by 9%, as described by Idriss and Boulanger (2008). Chapter 4 describes additional specimens drawn from the literature. Intact samples obtained directly by the writers were recovered in accordance with ASTM D1587/1587M (ASTM 2015) using the mud rotary drilling technique, an Osterberg piston sampler, and specially-fabricated thin-walled stainless steel Shelby tubes with machine-beveled inside cutting edges similar to that described by Wijewickreme et al. (2019). Intact samples obtained by consulting firms were generally recovered using mud rotary drilling and standard Shelby tubes; the type of sampler used varied.

Tubes recovered by the writers were sealed and transported in an upright condition and stored in climate-controlled environment until extrusion and specimen preparation. Prior to extrusion, the tubes were cut into two to three segments to minimize the travel distance of the soil sample upon extrusion. Specimens were trimmed from soil at top of the tube following extrusion in the same direction of travel as that of the soil during sampling to prevent shear stress reversal along the interface with the tube interior (Bray and Sancio 2006). The soil samples tested in this study are generally classified as silty sand (SM) to nonplastic silt (ML), low-plasticity silt (ML) to clay (CL), and high plasticity silt (MH), per the Unified Soil Classification System (USCS), with PI ranging from 0 to 39 (Table 2.1), average fines, silt, and clay contents range from 35 to 97%, 54 to 83%, and 12 to 17%, respectively.

2.3 EXPERIMENTAL TEST PROCEDURES

The laboratory testing program in this study consisted of the assessment of intact sample quality, evaluation of stress history and compressibility, constant-volume, monotonic DSS strength, and cyclic resistance. All laboratory tests by the authors were conducted on intact specimens prepared from thin-walled tube sample at nearly-saturated and fully-saturated conditions, as inferred from compression wave velocities, V_p > 700 m/s (Stokoe and Santamarina 2000, Stokoe et al. 2016) and gravimetric water contents.

2.3.1 Constant-Rate-of-Strain (CRS) Consolidation Tests

Constant rate of strain (CRS) consolidation tests with measurement of excess pore pressure, u_e, and without back-pressure saturation were conducted on representative intact specimens to determine the preconsolidation stress, σ'_p, overconsolidation ratio, OCR, and the compression and recompression indices, C_c and C_r, respectively. A strain rate of 0.45 - 0.75%/hr was selected to avoid exceeding u_e measured at the bottom of the specimen from threshold value of 15% during or according the test (ASTM D4186/4186M, ASTM 2012).

2.3.2 Constant-Volume Monotonic Direct Simple Shear Tests

Constant-volume monotonic DSS tests were conducted using the SSH-100 direct simple shear device with retrofitted platens to accommodate sensors for body wave measurements, described in detail by Dadashiserej et al. (2022b). Specimens for monotonic tests were consolidated using two approaches: (1) consolidation under vertical effective stress, σ'_{vc}, equal to the estimated *in-situ* vertical effective stress, σ'_{v0}, using recompression technique (Bjerrum and Landva 1966), and (2) the SHANSEP technique in which σ'_p deduced from results of CRS tests was exceeded by a large margin followed by unloading to the desired σ'_{vc} (Ladd 1991). After completion of the primary consolidation under σ'_{vc}, the load was maintained constant for at least ten times longer than the primary consolidation time to complete one cycle of secondary compression, followed by monotonic shearing with a strain rate of 5%/hr.

Table 2.1 Details of test sites and material characterization.

Description	Site ID									
	A	**B**	**C**	**D**	**E**	**F**	**G**	**H**	**I**	**J**
Location	**Columbia River Longview, WA**	**Willamette River Corvallis, OR**	**Tacoma, WA**	**Columbia River Portland, OR**	**Columbia River Portland, OR**	**Willamette River Wilsonville, OR**	**Willamette River Portland OR**	**Anchorage, AK**	**Newport, OR**	**Victoria, BC**
Number of Stress-Controlled Cyclic Tests	8	11	6	16	27	17	4	3	3	4
Range in Sample Depth (m)	2.4 - 3.2	2.4 - 9.3	5.3 - 9.1	9.1 - 11.2	7.3 - 12.0	6.2 - 10.1	14.6 - 15.2	3.5 - 7.9	3.0 - 9.6	4.7 - 6.8
Natural Water Content, w_n (%)	44 - 59	38 - 62	40 - 44	75	39 - 92	28 - 43	44	23 - 31	37 - 62	14 - 24
Liquid Limit, *LL* (%)	39 - 51	39 - 48	35 - 40	70	38 - 81	28 - 50	35 - 40	32	76	NA
Plasticity Index, *PI* (%)	10 - 19	11 - 16	9	14 - 39	10 - 28	0 - 20	10 - 11	0 - 12	0 - 29	1 - 23
Vertical Effective Consolidation Stress, σ'_{vc} (kPa)	32 - 36	50 - 160	80 - 100	98 - 112	95 - 215	150 - 160	160	60 – 105	78 - 411	82 - 105
Overconsolidation Ratio, *OCR*	3.0 - 4.2	1.4 - 2.0	1.5 - 1.6	1.6 - 2.2	1.0 - 2.2	1.0 - 2.7	1.2	1.9 - 2.6	1.0 - 1.6	4

2.3.3 Constant-Volume, Stress-Controlled Cyclic Direct Simple Shear Tests

Constant-volume, stress-controlled, cyclic DSS tests were conducted on intact specimens at the estimated *in-situ* stress state conditions. Additional cyclic DSS tests were carried out on mechanically-induced, normally consolidated (MC-NC, σ'_p exceeded) specimens to investigate the effect of stress history on cyclic response. Following the completion of primary consolidation under $\sigma'_{vc} = \sigma'_{v0}$ and sufficient time for secondary compression and body wave velocity measurements, the specimens were sheared with uniform sinusoidal shear stress cycles, τ_{cyc}, with a maximum amplitude determined in terms of cyclic stress ratio, $CSR = \tau_{cyc} / \sigma'_{vc}$, with loading frequency, f, of 0.1 Hz. The cyclic phase continued to generate a minimum single amplitude shear strain, γ, of 3.75%. Shear strains commonly exceeded this minimum amplitude.

3 EXPERIMENTAL TEST RESULTS AND DISCUSSION

The results of laboratory tests on intact specimens are used to inform the development of statistical models to estimate cyclic resistance herein; thus, a brief description of pertinent results follows. The test designations in Tables 3.1, 3.2 and Tables A1 and A2 (Appendix A) indicate the test site and borehole or test panel from which each sample has been retrieved, and the test type conducted. For example, Test A-UT-CRS (Table 3.1) indicates that a constant rate of strain (CRS) consolidation test has been conducted on a specimen prepared from a sample retrieved from the UT Test Panel of Site A.

3.1 CONSTANT-RATE-OF-STRAIN CONSOLIDATION TEST

Figure 3.1 presents the typical one-dimensional compression response of representative intact specimens prepared from soil samples retrieved from various test sites. Unloading-reloading excursions were conducted to determine C_c, C_r, σ'_p, and also to aid assessments of sample quality using the approach proposed by DeJong et al. (2018). The compression curves for specimens with higher *PI* exhibit sharp transition in behavior following the yield, well-defined σ'_p, and larger compressibility than nonplastic to low plasticity specimens, which exhibited more rounded compression curves, consistent with observations by Boone (2010). For example, Specimen E-2-CRS with $PI = 28$ is characterized with $C_c = 1.046$, significantly larger than the low plasticity E-1-CRS with *PI* of 12 and $C_c = 0.276$ (Fig. 3.1c). The average of σ'_p determined from work-energy based method (Becker et al. 1987) and Casagrande construction (Casagrande 1936) ranges from 95 to 427 kPa for the specimens evaluated, as summarized in Table 3.1. Given the range in sampling depth and corresponding estimated σ'_{v0}, the *OCR* of specimens tested range from lightly-overconsolidated ($OCR = 1.2$, Site G) to moderately-overconsolidated ($OCR = 4.2$, Site A).

Specimen quality was evaluated using strain energy-based criteria proposed by DeJong et al. (2018) for low plasticity silts. The ratio of initial recompression index, C_{ri} $(= \Delta e/\Delta \log \sigma'_v)$, to C_c, C_{ri}/C_c, and ratio of strain-energy based recompression index, C_{rw} $(= \Delta e/\Delta \log \sigma'_v)$ to strain-energy based compression index, C_{rw}/C_{cw}, were calculated and summarized in Table 3.1. Based on criterion proposed by DeJong et al. (2018), high quality specimens are associated with compression ratio of smaller than 0.15, whereas specimens with compression ratio ranging from 0.15 to 0.4 are considered as moderate quality. The compression ratios calculated in Table 3.1 correspond to specimens with high quality, with only two of 15 specimens exhibiting $C_{rw}/C_{cw} > 0.2$.

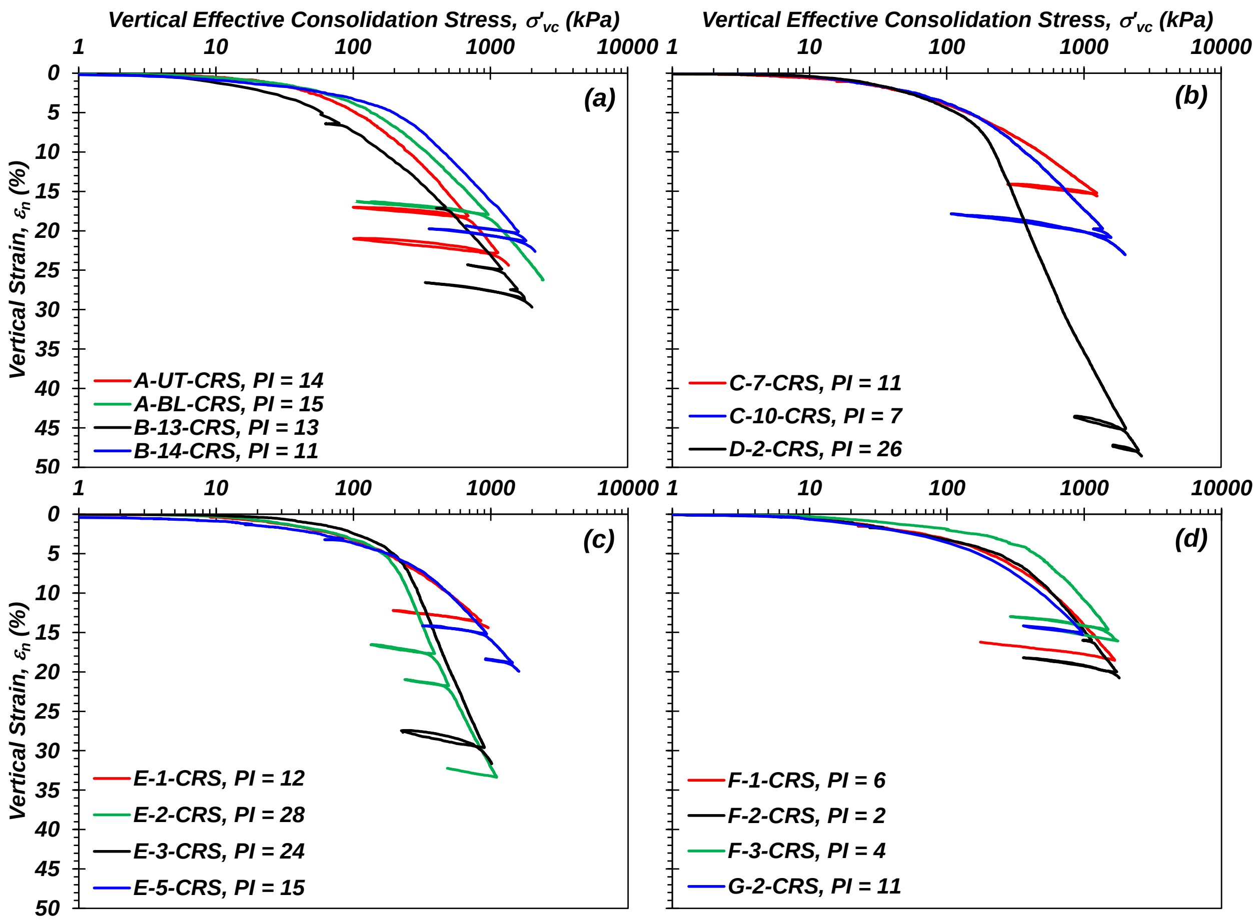

Figure 3.1 One-dimensional compression response under constant-rate-of-strain (CRS) consolidation tests conducted on intact specimens from: (a) Sites A and B, (b) Sites C and D, (c) Site E, and (d) Sites F and G.

Table 3.1 Summary of consolidation parameters and compression ratios to evaluate sample quality.

Test Designation	*In-Situ* Vertical Effective Stress, σ'_{v0} (kPa)	*In-Situ* Pre-consolidation Stress, σ'_p [1] (kPa)	Over-consolidation Ratio OCR	C_{ri}	C_c	C_{ri}/C_c	C_{rw}	C_{cw}	C_{rw}/C_{cw}
A-UT-CRS	36	112	3.1	0.055	0.646	0.085	0.011	0.096	0.115
A-BL-CRS	32	134	4.2	0.031	0.379	0.083	0.007	0.069	0.105
B-13-CRS	50	95	1.9	0.080	0.412	0.194	0.021	0.076	0.276
B-14-CRS	160	250	1.5	0.050	0.410	0.122	0.015	0.084	0.179
C-7-CRS	80	122	1.5	NA[2]	NA	NA	NA	NA	NA
C-10-CRS	155	100	1.6	NA	NA	NA	NA	NA	NA
D-2-CRS	112	224	2.0	0.130	1.110	0.120	0.020	0.194	0.100
E-1-CRS	95	190	2.0	0.041	0.276	0.147	0.015	0.055	0.269
E-2-CRS	100	200	2.0	0.073	1.046	0.069	0.015	0.139	0.111
E-3-CRS	107	225	2.1	0.111	1.662	0.067	0.016	0.169	0.092
E-5-CRS	125	275	2.2	0.052	0.403	0.130	0.016	0.084	0.194
F-1-CRS	120	314	2.6	0.058	0.404	0.144	0.015	0.084	0.181
F-2-CRS	150	360	2.4	0.055	0.432	0.128	0.014	0.093	0.153
F-3-CRS	158	427	2.7	0.036	0.419	0.087	0.010	0.091	0.105
G-2-CRS	188	160	1.2	NA	NA	NA	NA	NA	NA

[1] Average of Casagrande construction and Becker et al. (1987) strain-energy based methods.
[2] Not available.

3.2 CONSTANT-VOLUME MONOTONIC DIRECT SIMPLE SHEAR TESTS

Figure 3.2 presents the monotonic DSS response of intact specimens consolidated using recompression and SHANSEP technique reported by for several of the study sites (reported by Stuedlein et al. 2023), in terms of normalized shear stress-shear strain (τ_h/σ'_{vc} -γ) responses, effective stress paths, and variation of normalized undrained shear strength, $s_{u,DSS}/\sigma'_{vc}$, with *OCR*, where $s_{u,DSS}$ is defined as shear stress corresponding to γ = 15%. Intact specimens tested from Site B exhibit nearly perfectly plastic τ_h/σ'_{vc}-γ response, while specimens from Sites D-2, E-1, and E-3 exhibit strain hardening responses. Specimens with *OCR* < 2.2 exhibited contractive responses for the entirety of the pre-failure stress path, whereas specimens with larger *OCR* exhibit initially dilative behavior followed by contraction towards failure (except E-1-M4). Figs. 3.2c, 3.2f, 3.2i, and 3.2l presents the variation of $s_{u,DSS}/\sigma'_{vc}$ with *OCR* for specimens from Sites B, D, E, and F. The deduced SHANSEP parameters indicate some degree of variability from site-to-site, but fall generally in the range provided by Ladd (1991). Detailed information regarding the constant-volume, monotonic DSS test results are provided in Table A1.

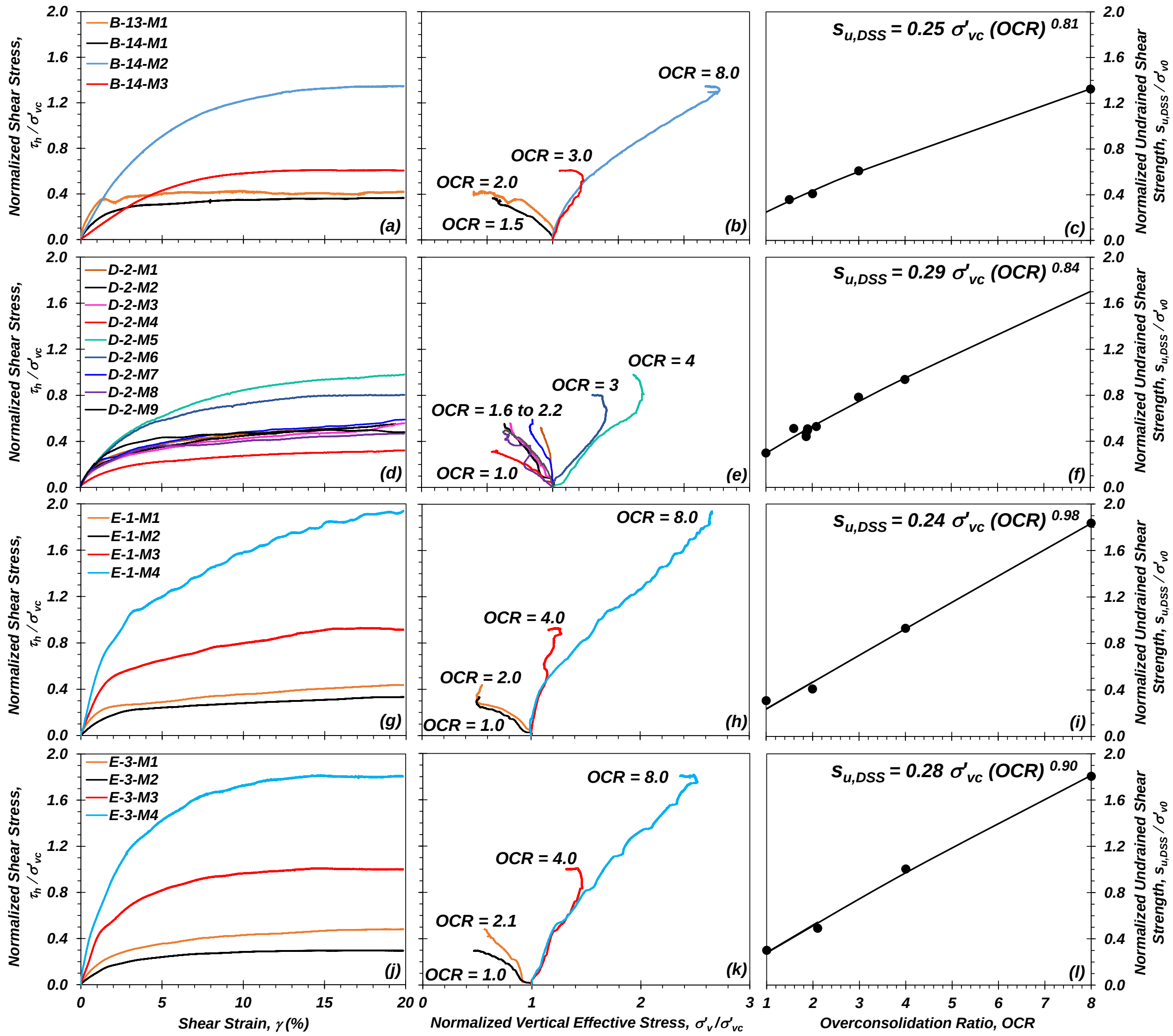

Figure 3.2 Monotonic undrained DSS response of intact specimens of silt, including: (a, d, g, and j) the normalized shear stress-shear strain responses, (b, e, h, and k) effective stress paths, and (c, f, i, and l) SHANSEP representation of undrained shear strength: (a - c) Site B, (d - f) Site D, (g – i, j - l) Site E (after Stuedlein et al. 2023).

3.3 CONSTANT-VOLUME, STRESS-CONTROLLED CYCLIC DIRECT SIMPLE SHEAR TESTS

3.3.1 Typical Stress-Strain Responses and Excess Pore Pressure Generation

The cyclic testing program in this study was designed and executed to identify the most significant factors contributing to the cyclic resistance of intact silt with emphasis on the role of soil indices, stress history, and loading amplitude on cyclic response. The outcome of this experimental program aided to improve the understanding cyclic response of silt and develop regression models to estimate the cyclic resistance of silt. Figure 3.3 presents examples of the cyclic response of intact specimens from Sites B, D, E, and F in terms of the normalized shear stress-shear strain, *CSR*-γ hysteresis, effective stress paths, and the accumulation of γ and excess pore pressure ratio, r_u, with number of loading cycles, *N* (after Stuedlein et al. 2023). During constant-volume DSS tests the changes in magnitude of r_u (r_u = 1-σ'_v/σ'_{vc}, where σ'_v is vertical effective stress) is specified from changes in σ'_v relative to σ'_{vc} (Dyvik et al. 1987).

Specimen B-14-8 (*PI* = 13, *OCR* = 1.5, *FC* = 81%; Table A2) consolidated under σ'_{v0} = 160 was subjected to *CSR* = 0.24 which resulted in γ = 3 and 3.75% at 22.2 and 26.2 cycles, respectively ($N_{\gamma=3\%}$ = 22.2 and $N_{\gamma=3.75\%}$ = 26.2; Figs. 3.3a and 3.3c). The generation of excess pore pressure is identified from migration of stress path towards the origin (Fig. 3.3b), which is about 64% at the end of *N* = 22.2 with $r_{u,max}$ = 96% (Fig. 3.3d) at the end of the cyclic phase (N_{max} = 38). The cyclic mobility type response is observed and interpreted from incremental accumulation of shear strain (Fig. 3.3c), excess pore pressure, degradation of shear stiffness with low to zero transient shear stiffness at shear stress close to zero (Fig. 3.3a), and without abrupt loss of strength (Castro and Poulos 1977, Boulanger et al. 1998, Sanin and Wijewickreme 2006).

Specimen F-2-5 (*PI* = 0, *OCR* = 2.4, *FC* = 36%; Table A2) was cyclically- sheared under σ'_{v0} = 150 kPa and *CSR* = 0.22 which resulted in $N_{\gamma=3\%}$ of 4.2 and $N_{\gamma=3.75\%}$ of 5.2, respectively, with corresponding $r_{u,max}$ = 98% (Figs. 3.3e and 3.3h). Although Specimen B-14-8 was sheared under larger *CSR* than Specimen F-2-5, it exhibited higher cyclic resistance ($N_{\gamma=3\%}$ = 22.2 versus $N_{\gamma=3\%}$ = 4.2), which can be attributed to the dominant effect of its larger *PI*, which overshadowed the lower *OCR* and density. It is notable that the hysteretic behavior of Specimens B-14-8 and F-2-5 can be qualitatively and quantitatively identified as sand-like at large γ (> 5%; Stuedlein et al. 2023), as characterized by narrow stress-strain hysteresis loops, transient zero or near-zero shear stiffness, and significant dilation prior to and following shear stress reversal (Figs. 3.3a and 3.3e). However, the hysteretic behavior of specimens may not be classified as sand-like at commonly-used cyclic strain failure criteria of γ = 3 or 3.75%. The evolution in hysteretic behavior with increasing *N* during cyclic tests suggests that the distinction between sand-like and clay-like behavior should be evaluated considering the earthquake magnitude (i.e., duration of loading, *N*) and the corresponding induced γ and r_u. Stuedlein et al. (2023) address usage of quantitative hysteretic metrics to assist in behavioral-based and inherent susceptibility of soils to liquefaction, and suggested that intensity and duration of cyclic loading are two important factors which can affect the evaluation of hysteretic soil behavior.

Figures 3.3i, 3.3j, 3.3k, and 3.3l present the cyclic response of specimen D-2-19 (*PI* = 26, *OCR* = 1.9, *FC* = 99%) consolidated under σ'_{v0} = 119 kPa and loaded with *CSR* = 0.36 to result in $N_{\gamma=3\%}$ = 0.8, γ_{max} = 18% after *N* = 19, and corresponding limited $r_{u,max}$ = 83%. The high *PI* for this specimen resulted in the limited $r_{u,max}$ relative to Specimens B-14-8 and F-2-5, with broader hysteresis loops and without transient, near-zero shear stiffness (Fig. 3.3i). Specimens D-2-19 (*OCR* = 1.9, *PI* = 26, *e* = 2.24) and E-5-3 (*OCR* = 2.2, *PI* = 15, *e* = 0.94) subjected to similar *CSR*s exhibited identical cyclic resistance interpreted in terms of $N_{\gamma=3\%}$. It appears that the effect of the larger *PI* on $N_{\gamma=3\%}$ for Specimen D-2-19 has been offset by the net dominant effect of higher density and *OCR* of Specimen E-5-3. Table A2 summarizes the results of constant-volume, stress-controlled cyclic DSS testing program interpreted in terms of $N_{\gamma=3\%}$ as well as different shear strain failure criterion which will be used in developing statistical regression models in the next sections.

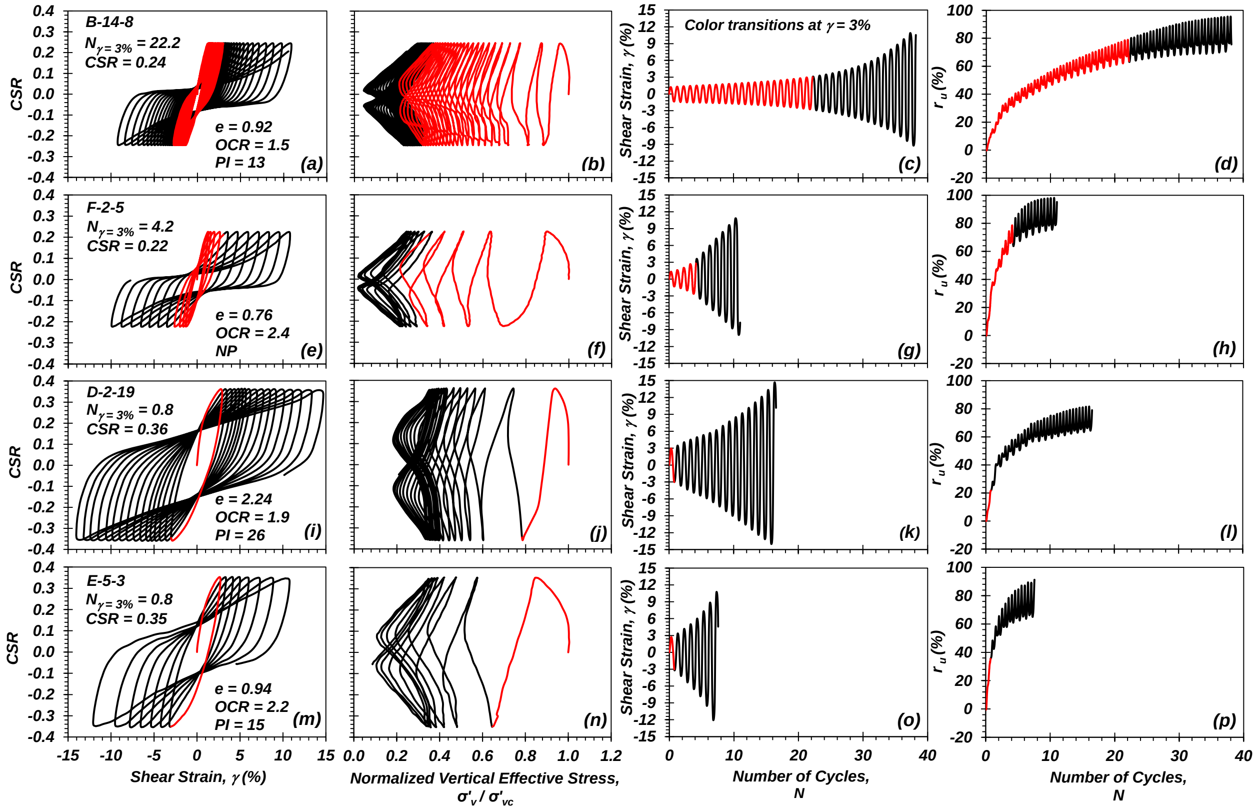

Figure 3.3 Constant-volume, stress-controlled, cyclic response of intact specimens indicating the: (a, e, i, and m) cyclic shear stress-shear strain, *CSR* - γ hysteresis, (b, f, j, and n) effective stress path, (c, g, k, and o) the accumulation of shear strain, γ, with number of loading cycles, *N*, and (d, h, l, and p) generation of excess pore pressure, r_u with *N*: (a - d) Specimen B-14-8, (e - h), Specimen F-2-5, (i - l) Specimen D-2-19, and (m - p) Specimen E-5-3 (after Stuedlein et al 2022).

3.3.2 Variation of Cyclic Resistance with Number of Loading Cycles

Figures 3.4a and 3.4b presents the variation of the cyclic resistance ratio, *CRR*, versus *N* to generate $\gamma = 3\%$ ($N_{\gamma=3\%}$), the cyclic failure criterion adopted in the Simplified Method for cyclic softening of silts and clays proposed by Idriss and Boulanger (2008), for the specimens tested along with selected results reported by Dahl et al. (2014). The *CRR* for the intact specimens tested in this study, characterized with $1 \leq OCR \leq 4.2$ and $0 \leq PI \leq 39$, is sensitive to stress history and plasticity. Power-law expressions are commonly used to represent the data in Figs. 3.4a and 3.4b and quantify the cyclic resistance ratio, $CRR = a \cdot N^{-b}$, defined as the *CSR* required to generate $\gamma = 3\%$, were determined using ordinary least squares (OLS) regression to facilitate comparison among the various soils. In the power law expression, coefficient *a* is the magnitude of *CRR* at $N = 1$ and exponent *b* is the slope of the *CRR-N* curve in logarithmic space, which controls the number of equivalent loading cycles, N_{eq}, associated with a given earthquake magnitude, M_w (Boulanger and Idriss 2015). Exponent b = 0.135 has been proposed for plastic, fine grained soils for use within the Simplified Method for cyclic softening (Idriss and Boulanger 2008) based on a limited dataset which could be compiled at the time. However, the results of this study indicated that the exponent b ranges from 0.05 to 0.15 for the intact fine-grained soils with the given ranges in *OCR* and *PI* tested (Table 3.2), and cannot be well-approximated with b = 0.135. The implication of this finding is that the N_{eq} and magnitude scaling factors, *MSF*, proposed for the fine-grained soils may differ from those proposed by Idriss and Boulanger (2008). The power-law coefficients and exponents (i.e., a and b), along with the corresponding coefficients of determination, R^2, for the fitted power-law expressions corresponding to $N_{\gamma=3\%}$ are provided in Table 3.2.

Comparison of the cyclic resistance of intact specimens in Figs. 3.4a and 3.4b indicates that for a given *N*, increases in *OCR* results in increases in *CRR*. For example, for specimens retrieved from Site E-5 (Table A2) and G-2 (Table A3) for the associated narrow range of *PI* and *e*, an increase in *OCR* from 1.2 (i.e., G-2) to *OCR* = 2.2 (i.e., E-5) resulted in an increase in 20 and 32% increase *CRR* corresponding to *N* ranging from 1 to 147 (Figure 3.4b). For comparable σ'_{v0} and *OCR*, an increase in *PI* increases the cyclic resistance. For example, for specimens retrieved from Site E and 1 <*N* < 160: an increase in *PI* from 15 (i.e., E-5, σ'_{v0} = 125 kPa, *OCR* = 2.2) to 28 (i.e., E-2, σ'_{v0} = 100 kPa, *OCR* = 2.0) improves the cyclic resistance by 6% to 34% corresponding to *N* ranging from 1 to 160 (Figure 3.4b). In addition, the *CRR* of specimens tested from Site B-13 with *PI* ranging from 14 to 16 and *OCR* of 1.9 (Fig. 3.4a) is similar to the results of cyclic DSS tests conducted on specimen with average *PI* of 18 (i.e., $7 \leq PI \leq 26$) and *OCR* = 2 reported by Dahl et al. (2014). Furthermore, for $1 \leq N \leq 80$ the *CRR* of intact silt specimens from site F-2 with average *PI* of 3 and *OCR* of 2.4 (Fig. 3.4b) is 30 to 37% greater than those with *PI* of 2 and *OCR* of 1 reported by Dahl et al. (2014).

The observed differences for specimens with similar index and stress history characteristics may stem from different depositional environments, void ratios, particle morphology, aging effects, and implementation of different consolidation methods (i.e., recompression versus quasi-SHANSEP technique; Stuedlein et al. 2023) to replicate the existing *in-situ* stress state conditions (Idriss and Boulanger 2008, Dahl et al. 2010, Wijewickreme et al. 2019, Dadashiserej et al. 2022c). Nonetheless, the suite of cyclic testing data presented here can be used to identify global trends in cyclic resistance and the associated uncertainty which may represent these other factors, possibly more difficult to quantify in routine practice.

The cyclic strength of low to high plasticity fine-grained soils can be expressed as a unique function of their monotonic undrained shear strength, $s_{u,DSS}$, defined as the shear stress corresponding to the γ = 15%, for those specimens which exhibit strain hardening during monotonic shearing. Figs. 3.4c and 3.4d present the cyclic strength ratio, $\tau_{cyc}/s_{u,DSS}$, required to reach γ = 3% with *N*, adjusted to f = 1 Hz (representative of typical earthquake loading frequencies), based on observations that the cyclic strength increases by 9% for each logarithmic cycle increase in f (Lefebvre and LeBouef 1987, Zergoun and Vaid 1994, Lefebvre and Pfendler 1996, Boulanger et al. 1998, Idriss and Boulanger 2008). Power law expressions similar to that fit to *CRR* - *N* data above were used to represent the variation of $\tau_{cyc}/s_{u,DSS}$ - *N* in Figs. 3.4c and 3.4d.

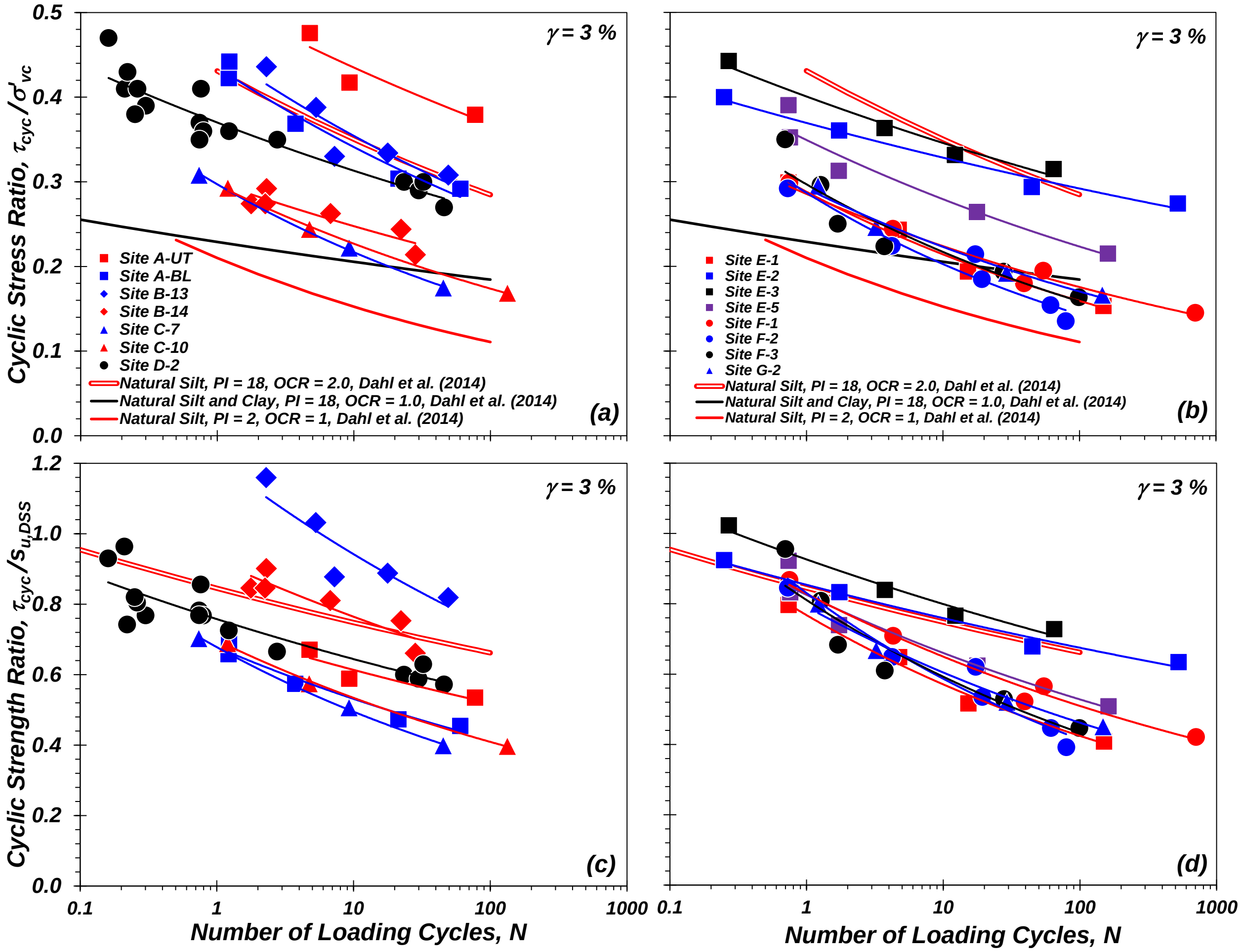

Figure 3.4 Comparison of the cyclic resistance of intact specimens from Sites A, B, C, and D (a and c), and Sites E, F, and G (b and d) indicating variation of: (a and b) cyclic stress ratio, *CSR*, and (c and d) cyclic strength ratio, $\tau_{cyc}/s_{u,DSS}$, with number of loading cycles, *N* to reach $\gamma = 3\%$.

For similar *OCR*s, $\tau_{cyc}/s_{u,DSS}$ generally increases with an increase in *PI*. For example, specimens from Site E-3 (*PI* = 25, *OCR* = 2.1) exhibited 26% greater cyclic strength than those from Site E- (*PI* =15 and *OCR* = 2.2) for *N* = 30 (Fig.3.4d). The variability in the relationship between $\tau_{cyc}/s_{u,DSS}$ with *PI* is explored in this study in later sections; however, Stuedlein et al. (2023) used a subset of the data in Figs. 3.4c and 3.4d to propose a relationship for $\tau_{cyc}/s_{u,DSS}$ with *PI* for *N* = 30, given by:

$$(\tau_{cyc}/s_u)_{N=30} = 0.54 \qquad 0 \le PI < 11 \tag{3.1a}$$

$$(\tau_{cyc}/s_u)_{N=30} = 0.030PI + 0.212 \qquad 11 \le PI < 18 \tag{3.1b}$$

$$(\tau_{cyc}/s_u)_{N=30} = 0.76 \qquad PI \ge 18 \tag{3.1c}$$

Table 3.2 Summary of fitted parameters for cyclic resistance ratio ($CRR - N$; f = 0.1 Hz) and cyclic strength ratio expressions $\tau_{cyc}/s_{u,DSS}$ (f = 1 Hz) for $N_{\gamma=3\%}$.

Test Designation	Vertical Effective Consolidation Stress, σ'_{v0} (kPa)	Over-consolidation Ratio, OCR	Plasticity Index, PI	$CRR - N$ Relationship			$\tau_{cyc}/s_{u,DSS} - N$ Relationship		
				Coefficient a	Exponent b	R^2	Coefficient a	Exponent b	R^2
A-UT-4		3.1	14						
A-UT-6	36	3.2	12	0.51	0.07	0.86	0.73	0.07	0.86
A-UT-7		3.0	15						
A-BL-2			10						
A-BL-3			11						
A-BL-4	32	4.2	11	0.44	0.11	0.97	0.68	0.11	0.97
A-BL-5			19						
A-BL-6			19						
B-13-15			16						
B-13-18			15						
B-13-19	50	1.9	14	0.45	0.11	0.81	1.21	0.11	0.81
B-13-20			15						
B-13-21			15						
B-14-7			13						
B-14-8			13						
B-14-9	160	1.5	11	0.30	0.08	0.82	0.92	0.08	0.82
B-14-14			15						
B-14-17			13						
B-14-22			13						
C-7-1			9						
C-7-2	80	1.5	9	0.30	0.14	1.00	0.68	0.14	1.00
C-7-3			9						
C-10-1			9						
C-10-2	100	1.6	9	0.30	0.12	1.00	0.70	0.12	1.00
C-10-3			9						
D-2-1	129	2.2	25						
D-2-2	114	1.7	22						
D-2-3	108	2.0	29						
D-2-5	100	2.1	14						
D-2-6	100	2.1	31						
D-2-7	100	2.1	31						
D-2-9	100	2.0	34						
D-2-10	118	2.1	34	0.37	0.07	0.89	0.76	0.07	0.83
D-2-11	118	2.1	39						
D-2-12	118	1.9	39						
D-2-13	118	1.9	28						
D-2-14	118	2.0	27						
D-2-15	105	1.9	28						
D-2-19	118	1.9	26						
D-2-27	122	2.0	21						
D-2-31	106	2.0	28						
E-1-1			12						
E-1-2		2.0	10	0.29	0.13	0.99	0.77	0.13	0.99
E-1-3			10						
E-1-4	95		12						
E-1-8			11						
E-1-9		1.0	11	0.24	0.13	0.99	0.85	0.13	0.99
E-1-10			11						
E-1-11			11						
E-2-1			26						
E-2-2	100	2.0	28	0.37	0.05	0.98	0.85	0.05	0.98
E-2-3			28						
E-2-4			28						
E-2-6			28						
E-2-7			28						
E-2-9	215	1.0	28	0.24	0.05	0.71	0.84	0.05	0.70
E-2-10			28						
E-2-11			28						
E-3-1			24						
E-3-2	107	2.1	27	0.40	0.06	0.97	0.93	0.06	0.97
E-3-3			27						
E-3-4			24						
E-5-1			15						
E-5-2			15						
E-5-3	125	2.2	15	0.35	0.10	0.96	0.83	0.10	0.96
E-5-4			15						
E-5-5			15						
E-5-6			15						

Table 3.2 (continued) Summary of fitted parameters for cyclic resistance ratio ($CRR - N$) and cyclic strength ratio expressions $\tau_{cyc}/s_{u,DSS}$ for $N_{\gamma=3\%}$.

F-1-1 F-1-2 F-1-3 F-1-4 F-1-5	120	2.6	NP	0.29	0.11	0.98	0.83	0.11	0.98
F-2-1 F-2-2 F-2-3 F-2-4 F-2-5 F-2-6	150	2.4	6 6 3 3 NP NP	0.29	0.15	0.92	0.83	0.15	0.92
F-3-1 F-3-2 F-3-3 F-3-4 F-3-5 F-3-7	158	2.7	11 11 4 4 4 20	0.30	0.14	0.91	0.81	0.14	0.91
G-2-1 G-2-2 G-2-4 G-2-5	160	1.2	10 10 11 11	0.29	0.12	0.98	0.79	0.12	0.98

4 DATABASE FOR THE DEVELOPMENT AND VALIDATION OF STATISTICAL MODELS DESCRIBING THE CYCLIC RESISTANCE OF SILTS

The Simplified Method (Seed and Idriss 1971) provides a means to quantify a factor of safety against cyclic failure using a selected cyclic failure criterion, which requires measurements or estimates of cyclic resistance. Estimates of cyclic resistance are required in the absence of site-specific cyclic laboratory test data providing the requisite CRR - N or $\tau_{cyc}/s_{u,DSS}$ - N curves. In addition, identifying the shear strain-dependent cyclic resistance can be useful as different projects may consider different failure criteria or set thresholds on allowable deformations. Unfortunately, models to estimate CRR - N or $\tau_{cyc}/s_{u,DSS}$ - N curves for low and medium plasticity silts are not presently available. Such models require a dataset sufficiently broad to produce robust and reliable statistical estimates. The dataset developed for the silts of Western Oregon and Southwest Washington described in Section 3 provides an opportunity for the development of statistical models, which forms the main focus for this study, as described herein.

The statistical models presented in the following section consists of three distinct cases using differing amounts of data as follows: (1) data used to initially train a statistical model, termed the *training dataset*; (2) data used to validate the general expressions of the initially trained statistical model, designated the *testing dataset*; and, (3) the *combined dataset* which consists of the *training* and *testing dataset*s, combined for the purposes of training the most robust, statistically-determined model parameters (i.e., coefficients, exponents, and intercepts). The available cyclic test data was interpreted to provide the cyclic resistance over a wide range in cyclic shear strain failure criteria, including $N_{\gamma=1\%}$, $N_{\gamma=2\%}$, $N_{\gamma=3\%}$, $N_{\gamma=3.75\%}$, $N_{\gamma=5\%}$, $N_{\gamma=8\%}$, and $N_{\gamma=10\%}$, to provide estimation of the strain-dependent cyclic resistance of the materials represented in the database for forward use in a performance-based earthquake engineering design framework.

For simplicity and ease of use, a preferred statistical model for cyclic resistance should maintain the same functional form for all strain amplitudes. The identification and evaluation of the preferred functional form, determined using the independent *training dataset*, is described in detail for $N_{\gamma=3\%}$ owing to the broad acceptance of 3% shear strain amplitudes as a cyclic shear strain failure criterion. In this manner, the trained model could be used to establish the accuracy, uncertainty, and robustness in the prediction of cyclic resistance for specimens in the independent *testing dataset*. Once deemed acceptable, the final regressed model parameters associated with the identified functional form of the statistical model was then trained on the *combined dataset* for different magnitudes of N_{γ}.

Figure 4.1 presents the variation of amount of data available in the *training*, *testing*, and *combined datasets* for a given cyclic shear strain failure criterion used as the basis for development of statistical models for *CRR* and $\tau_{cyc}/s_{u,DSS}$. The amount of data available reduces sharply following the $N_{\gamma>3.75\%}$ which affects the quality of the model estimates for $N_{\gamma>3.75\%}$. Thus, there will remain a significant need to: (1) continue to collect and evaluate high-quality cyclic laboratory test data, and (2) continue cyclic loading beyond the typical cyclic failure criteria of 3 and 3.75%. The *training dataset* is summarized in Table A2 and consists of maximum of 83 (for $N_{\gamma<3.75\%}$) high-quality constant-volume, stress-controlled, cyclic DSS tests conducted on intact silt specimens. The *testing dataset* summarized in Table A3 and includes a maximum of 45 (corresponding to $N_{\gamma=3.75\%}$) constant-volume, stress-controlled, cyclic DSS conducted on intact specimens retrieved from low to high plasticity silt and clay deposits from western end of Potrero Canyon in Los Angeles County reported by Dahl et al. (2014) and Fraser River Delta at the province of British Columbia, Canada reported by Sanin (2010) and Soysa (2015). In order to increase the amount of data available for testing tentative statistical models and a lack of sufficient tests conducted on intact silty soils that are reported in the literature, the results of tests conducted on specimens from Sites A-BL, C-10, and G-2 (Table A2) were included in the *testing dataset* to improve representation of the range in certain variables (e.g., *OCR*, *PI*) for which a trained model can be independently evaluated.

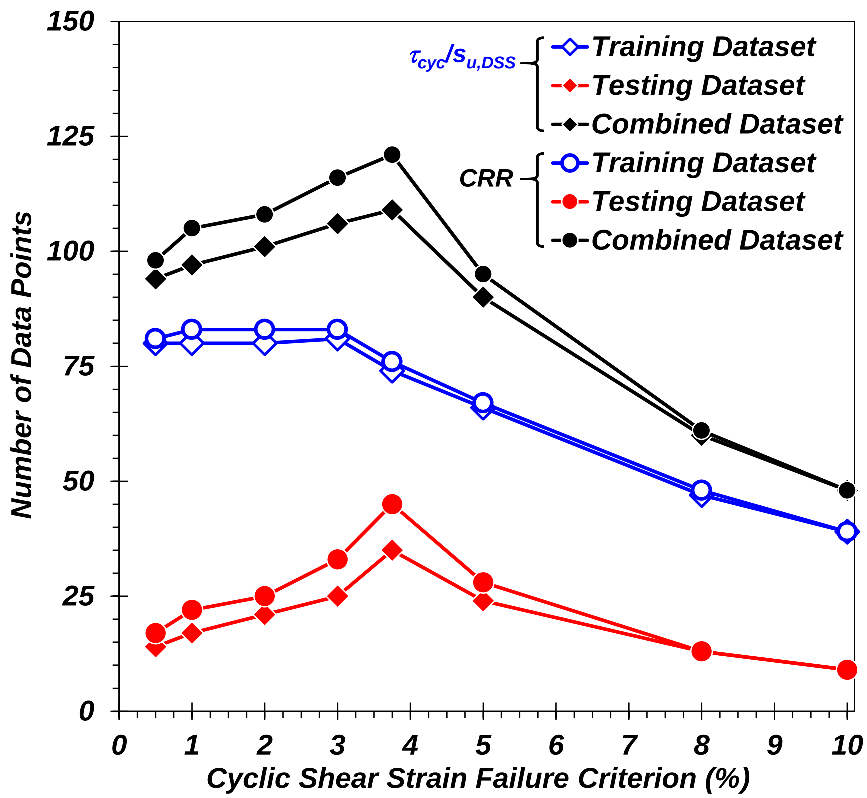

Figure 4.1 Variation of the number of data pairs included in the *training*, *testing*, and *combined datasets*, with cyclic shear strain failure criterion.

Figure 4.2 presents the range in soil properties represented within the *training*, *testing*, and *combined datasets* in terms of the plasticity index, *PI*, fines content, *FC*, and overconsolidation ratio, *OCR*. The intact specimens were characterized with *PI* varying from 0 to 39 and 0 to 34, *FC* from 29 to 100% and 35 to 100%, and *OCR* ranging from 1 to 4 and 1 to 4.2 for the *training* and *testing datasets*, respectively. The fitted coefficient *a* and exponent *b* for the *CRR* - *N* and $\tau_{cyc}/s_{u,DSS}$ - *N* power-law relationships for *training* and *testing datasets* corresponding to $N_{\gamma=3\%}$ are summarized in Tables 3.2 (i.e., Section 3.3.2) and 4.1, respectively. Note that in some cases, insufficient cyclic laboratory test data were available in the *testing dataset* to determine suitable power law coefficients and exponents; therefore, these data are not represented in Table 4.1. Table A3 provides the full *testing dataset*, which includes those data available for specific cyclic shear strain failure criteria which are used in the development of cycle- and strain-dependent *CRR* $\tau_{cyc}/s_{u,DSS}$ models in Sections 5.3 and 5.4, respectively.

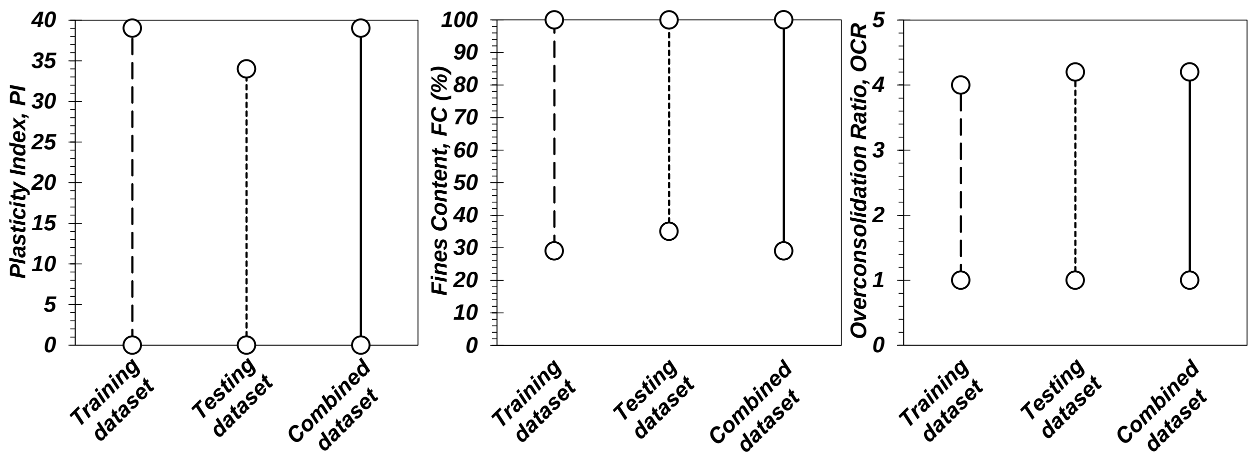

Figure 4.2 Range in soil properties for *training*, *testing*, and *combined datasets*: (a) plasticity index, *PI*, (b) fines content, *FC*, and (c) overconsolidation ratio, *OCR*.

Table 4.1 Summary of fitted coefficients and exponents for cyclic resistance ratio (*CRR* – *N*) and cyclic strength ratio ($\tau_{cyc}/s_{u,DSS}$ – *N*) expressions for the laboratory tests in the *testing dataset* where sufficient data existed, and corresponding to $N_{\gamma=3\%}$.

Test Designation	*OCR*	*PI*	*CRR-N* Relationship			τ / $s_{u,DSS}$ – *N* Relationship		
			Coefficient *a*	Exponent *b*	R^2	Coefficient *a*	Exponent *b*	R^2
PC-A-01	1.0	18						
PC-A-02	1.0	17						
PC-A-03	1.0	27	0.23	0.05	0.90			
PC-A-04	1.0	26						
PC-A-05	1.0	23				0.85	0.05	0.90
PC-A-06	1.0	13						
PC-A-07	2.0	24						
PC-A-08	2.0	12	0.43	0.09	1.00			
PC-A-09	2.0	9						
PC-A-10	2.0	15						
PC-B-01	1.0	0						
PC-B-02	1.0	0						
PC-B-03	1.0	0	0.21	0.14	1.00		NA[1]	
PC-B-04	1.0	0						
PC-B-05	1.0	0						
PC-B-06	1.0	1						
A-BL-2		10						
A-BL-3		11						
A-BL-4	4.2	11	0.44	0.11	0.97	0.68	0.11	0.97
A-BL-5		19						
A-BL-6		19						
C-10-1		9						
C-10-2	1.6	9	0.30	0.12	1.00	0.70	0.12	1.00
C-10-3		9						
G-2-1		10						
G-2-2	1.2	10	0.29	0.12	0.98	0.79	0.12	0.98
G-2-4		11						
G-2-5		11						

[1] Not available.

5 STATISTICAL REGRESSION MODELS FOR THE CYCLIC RESISTANCE OF SILT

5.1 GOAL OF MODEL DEVELOPMENT

The Simplified Method used to evaluate the cyclic resistance of sand-like soils (Seed and Idriss 1971; Youd et al. 2001; Boulanger & Idriss 2014) has been proposed for use in the evaluation of cyclic softening of clay-like soil (Boulanger and Idriss 2007, Idriss and Boulanger 2008). However, the amount of data used to set preliminary recommendations for the Simplified Method for cyclic softening assessment is relatively low, and therefore the reliability of this procedure and the confidence in its application are less established than that for liquefaction triggering. Specifically, the Simplified Method for cyclic softening has relied upon on cyclic results of six natural plastic soils:

- Intact block samples of St. Alban clay that were classified as CL with *PI* of 20 and *OCR* = 2.2 (Lefebvre and Pfendler 1996);
- Resedimented samples of Boston Blue clay that were characterized as CL with *PI* of 21 and *OCR* ranging from 1 to 2 (Azzouz et al. 1989);
- Intact block samples of gray marine Cloverdale clay that were classified as CL and CH with *PI* of 24 and *OCR* of 1 (Zergoun and Vaid 1994);
- Intact samples of marine Drammen clay classified as CH with *PI* = 27 and laboratory-induced *OCR* of 1 and 4 (Andersen et al. 1988);
- Intact samples of marine Itsukaichi clay that were characterized as MH with *PI* of 73 and *OCR* = 1 (Hyodo et al. 1994); and,
- Intact samples of CWOC silt that were characterized as ML with *PI* of 12 and *OCR* = 2 (Woodward-Clyde 1992).

These six natural soils were paired with laboratory test results of two fine-grained tailings to form the basis for the Simplified Method for cyclic softening assessment.

The database of laboratory cyclic tests conducted in this study (Fig. 3.4; Tables A2 and A3) indicate that the cyclic resistance ratio (*CRR*) and the exponent *b* (i.e., the slope of the *CRR*- *N* curve in logarithmic space) of low and moderate plasticity silts for $N_{\gamma=3\%}$ vary across a wide range and are not well-approximated by a single value of *b*. The implication of this finding is that the equivalent number of cycles, N_{eq}, used for the assessment of cyclic softening of clays as well as magnitude scaling factors, *MSF*, proposed for clays may not be suitable for silts.

Further, it is of interest to eventually assess the cyclic resistance of fine-grained soils in terms of the performance-based earthquake engineering (PBEE) framework, as different projects have different thresholds of risk and allowable deformation. Accordingly, incorporation of a refined Simplified Method for cyclic failure into the PBEE framework would link the computed factor of safety against cyclic failure to the selected failure strain threshold and corresponding permanent displacements. Development of statistical regression models for a range in cyclic shear strain failure criteria may provide a suitable means to assess the risk for cyclic failure within Simplified Method, inform a site-specific test program, and to calibrate the advanced constitutive models for numerical dynamic analysis in absence of site-specific laboratory testing program.

5.1.1 General Factors Contributing to the Cyclic Resistance of Fine-Grained Soil

The results of the laboratory testing programs represented in the current database (e.g., Sanin and Wijewickreme 2006; Dahl et al. 2014, 2018; Wijewickreme et al. 2019; Jana and Stuedlein 2021; Dadashiserej et al. 2022a, 2022b, 2022c, 2022d; Stuedlein et al. 2023 and contributing consultant project files) suggest that the overconsolidation ratio, *OCR*, mineralogy, plasticity index, *PI*, fines content, *FC*, and void ratio, *e*, are the most important factors contributing to the cyclic resistance of plastic soil deposits. The importance of each of these factors in the variation of exponent *b*, *CRR*, and $\tau_{cyc}/s_{u,DSS}$ at $N_{\gamma=3\%}$, as the commonly-used cyclic shear strain failure criterion, are investigated and are generalized to different magnitudes of cyclic shear strain failure criteria in the following sections.

5.1.2 General Procedure for Statistical Model Development

The modeling approach used in this study was conducted in a staged manner starting with inspecting the relative importance of the selected governing factors (i.e., predictor variables; *OCR*, *PI*, *FC*, and *e*) on the response variables (i.e., exponent *b*, *CRR*, and $\tau_{cyc}/s_{u,DSS}$) for $N_{\gamma=3\%}$ over the *training dataset*. Univariate scatter plots provide an appropriate means to identify overall trends between predictor and response variables in terms of lack of correlation, weak to strong linear correlation, or nonlinear correlation. Once the initial trends are identified, statistical modeling may then proceed using multiple linear or nonlinear regression analysis, as appropriate. This study implemented the software package *R*[1] to evaluate the performance, statistical rigor, accuracy, and uncertainty of the various regression models.

In general, the robustness of the regression models and their performance was assessed in terms of the following statistical metrics:

- **Sum of square errors, SSE**, equal to the sum of the squared differences between model predicted and laboratory-based values. The smaller the SSE, the better the estimate provided by the model;

---

[1] R Core Team (2022). R: A language and environment for statistical computing. R Foundation for Statistical Computing, Vienna, Austria.URL https://www.R-project.org/.

- **Standard error, SE**, for any given fitted regression parameter, which is the estimate of the standard deviation of the errors in the fitted parameter;
- **Residual standard error, RSE**, for a given regression model, equal to the square root of the residual sum of squares divided by the number of the degrees of freedom of the residuals (defined as the difference between the model prediction and the observation);
- **Average bias, $\bar{\lambda}$**, for a given regression model is defined as average ratio of measured and predicted responses (whereas individual ratios are the point or sample bias, λ). $\bar{\lambda}$ = 1.0 indicates an unbiased model *on average*. The average bias is best interpreted in conjunction with a measure of dispersion in the sample bias;
- **Coefficient of variation in the sample bias, COV_λ**, is defined as the ratio of the standard deviation of the sample biases and $\bar{\lambda}$. The smaller the COV_λ, the lower the dispersion or variability in the model estimate;
- **Coefficient of multiple determination, R^2**, equal to the proportion of variation in the response variable explained by the variation in the predictor variable, equal to $(COV(X,Y)/SD_X * SD_Y)^2$, where X and Y are predictor and response variables, respectively, $COV(X,Y)$ is the covariance between X and Y, and SD_X and SD_Y indicate the standard deviation of variables X and Y, respectively; and,
- ***p*-value**, equal to the probability of obtaining a statistical test result that is at least as extreme as obtained in a given statistical test provided the null hypothesis underlying the statistical test is correct (Wasserstein & Lazar 2016). In other words, the *p*-value tests the null hypothesis for each predictor that the corresponding fitted parameter is equal to zero (no effect). A low *p*-value (typically < 0.05) indicates that the null hypothesis can be rejected with a confidence of 95% and is commonly used to interpret that the fitted parameter is statistically significant.

The potential for multicollinearity between each pair of predictors, which occurs when one predictor in a regression model can be linearly predicted by other predictors with a considerable degree of accuracy, was examined by calculating the variance inflation factor (James & Izien 2014), VIF, for each predictor variable. The VIF allows for identification of predictor variables that may be correlated with one another, which violates the assumption of independence of predictor variables, and serves to reduce the statistical strength of regression models. Additionally, removal of correlated predictor variables serves to provide less complicated statistical models. As a rule of thumb, VIFs larger than five indicate the possible existence of strong multicollinearity between predictor variables (James & Izien 2014).

Once independent and statistically significant predictor variables have been identified, regression models of various levels of complexity are evaluated in a stepwise procedure to identify the strongest prediction using the fewest number of variables with the simplest functional form by monitoring the variations in R^2 and the p-values of predictor variables. The statistical strength of any given regression model is then quantified using R^2, $\bar{\lambda}$, and $COV_{\bar{\lambda}}$ for comparison of performance across the various models identified. Once a model is finalized based on the *training dataset* for $N_{\gamma=3\%}$, the final model was examined over independent *testing dataset* for $N_{\gamma=3\%}$ to establish accuracy and uncertainty of the model predictions, assess robustness, and confirm suitability of the model to generalize for different magnitudes of N_γ. If deemed acceptable, the functional form of the selected regression model is then retrained using the *combined dataset* for different magnitudes of N_γ to obtain the final model with the most robust parameters.

5.2 STATISTICAL MODEL FOR ESTIMATION OF *CRR* POWER LAW EXPONENT *b*

5.2.1 Initial Investigation of Possible Predictor Variables

Soil variables including the *OCR*, *FC*, *PI*, and *e* have been identified as the most relevant parameters that govern the cyclic response of nonplastic to medium-plasticity silty soils. The effect of *FC* was ignored for the available data due to: (1) the interdependency identified between *PI* and *FC*, and (2) the fact that the fines fraction (*FC* > 50%) provides the dominant stress-carrying matrix controlling soil behavior (Thevanayagam and Martin 2002; Mitchell and Soga 2005; Boulanger and Idriss 2006; Bray and Sancio 2006; Simpson and Evans 2015; Armstrong and Malvick 2016) for the majority of the specimens tested.

Figure 5.1 presents the variation of exponent *b* from the *training dataset* for $N_{\gamma=3\%}$ with respect to *e*, *PI*, and *OCR*, suggesting that there is a relatively strong correlation between *b* and *e* and *PI*, as characterized by the relatively large R^2 (Figs. 5.1a and 5.1b). The scatter plot comparing *b* and *OCR* indicates no discernible linear trend ($R^2 = 0.01$), suggesting that *OCR* may not be a suitable variable in the linear model explaining the variation of *b* (Fig. 5.1c). These observations were confirmed by investigation of the univariate correlation of *e*, *OCR*, and *PI* to *b* using a simple linear model with fitting coefficient a_0 and intercept a_1. Table B1 (Appendix B) summarizes the analyses conducted on simple univariate linear regression models in terms of the estimated regression coefficients and intercepts, residual standard error (i.e., RSE), and corresponding p-values for testing the null hypothesis. The results suggest that there is a statistically significant linear relationship between *e* and *PI* versus *b*, interpreted from calculated small p-values for the hypothesis tests (i.e., p-value < 0.05) and relatively large R^2. Conversely, the calculated high p-value of 0.768 and low R^2 for the linear model with *OCR* as a predictor indicates that *OCR* does not serve to explain the variation of exponent *b*.

PI and *e* were identified as statistically-significant predictors of exponent *b*; however, the use of both of these variables within a single multivariate linear regression model must be contingent on their independence. Figure 5.2 presents the variation of the *PI* versus *e* for the laboratory tests conducted on intact specimens in the *training dataset* and indicates a strong correlation characterized by an R^2 of 0.77. In addition, the results of multicollinearity analysis between *e* and

PI are summarized in Table B2, where the VIF is calculated for the multiple linear regression model using PI and e as predictors:

$$b = a_0 \cdot PI + a_1 \cdot e + a_2 \tag{5.1}$$

where a_0 and a_1 are the fitted coefficients and a_2 is the fitted intercept. The VIF values calculated for PI and e in Eq. (5.1) equal 5.36 and confirms the lack of independence between e and PI, which may be anticipated from basic soil mechanics; that is, as the clay content increases, the prevalence for large void ratios associated with platy- and rod-shaped clay minerals increases, leading to larger void ratios.

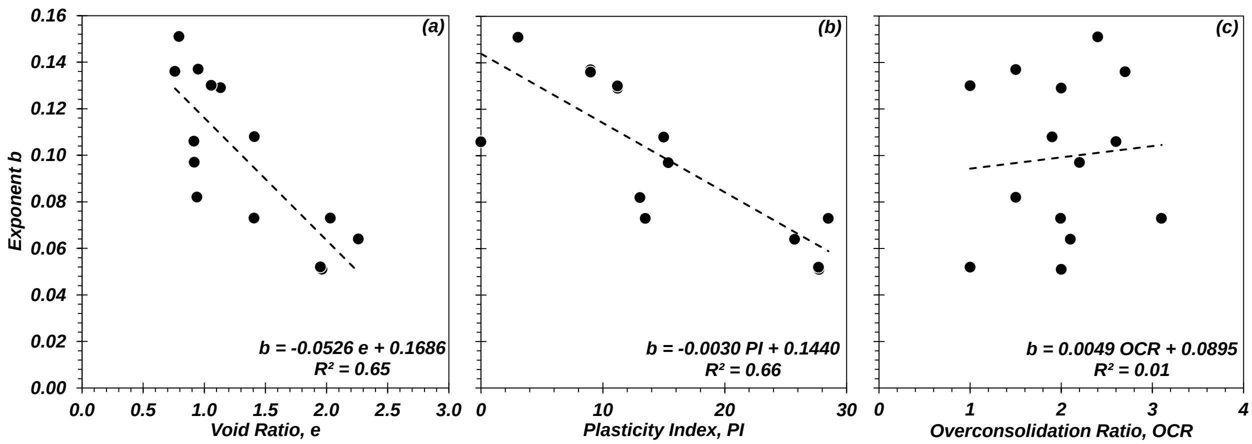

Figure 5.1 Variation of exponent *b* with respect to: (a) void ratio, *e*, (b) plasticity index, *PI*, and (c) overconsolidation ratio, *OCR*.

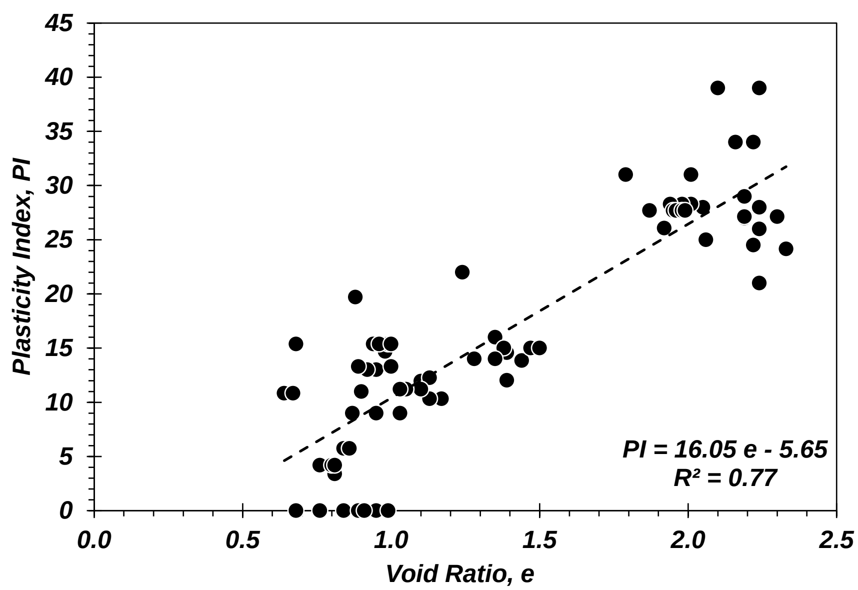

Figure 5.2 Variation of plasticity index, *PI*, versus void ratio, *e*, for the *training dataset*.

Therefore, the univariate linear model implementing *PI* as a single predictor is considered further, given by:

$$b = a_0 \cdot PI + a_1 \tag{5.2}$$

where a_0 and a_1 are fitted coefficient and intercept, respectively. The statistical analysis conducted on Eq. (5.2) is summarized in Table B2 for comparison of statistical strength to Eq. (5.1), which shows that although model of Eq. (5.2) is simpler (with *PI* as a single predictor), it performs equally well as the more complicated bivariate model of Eq. (5.1) in estimation of exponent *b*, interpreted through the similar RSE and R^2. Note that the larger R^2 of Eq. (5.1) does not necessarily mean it is more robust since: (1) predictors used in Eq. (5.1) are not independent, and (2) generally adding an extra predictor (dependent or independent) to the model results in increases in R^2, thus an additional statistical metric (e.g., $\overline{\lambda}$, $COV_{\overline{\lambda}}$) is necessary to evaluate the model performance. The final functional form of the univariate regression model to estimate exponent *b* for $N_{\gamma=3\%}$ is described below.

5.2.2 Validation of the Functional Form of the Exponent *b* Model

The results of the statistical analyses described in the previous section indicated that *e* and *PI* are the most relevant parameters that explain variations in exponent *b* for the soils represented within the *training dataset*. The analyses also demonstrated that the linear combination of these parameters should be used due to the existing correlation between *e* and *PI* (Fig. 5.2; Table B2: VIF > 5). In this regard, numerous trial regression models with a single predictor consisting of linear and nonlinear combinations of *e* and *PI* were examined to identify the strongest model associated with the simplest transformations of the predictor and response variables. In the following, the most appropriate model with the highest accuracy is introduced and evaluated against the independent *testing dataset* for $N_{\gamma=3\%}$.

Given the ability to determine Atterberg limits from more widely-available, disturbed split-spoon samples, a model that requires *PI* as a single predictor variable was deemed desirable (i.e., did not require intact tube samples to determine the void ratio). Numerous regression models with *PI* as the single predictor variable were evaluated using the ordinary least squares (OLS) method and the software package *R*. Equation (5.3) was identified as the statistical model with the lowest SSE, $\overline{\lambda}$ nearest to 1.0, lowest $COV_{\overline{\lambda}}$, and largest R^2, among the various models evaluated:

$$b^* = a_0 \cdot (PI + 1) + a_1 \tag{5.3}$$

where b^* is the predicted exponent *b*, and a_0 and a_1 are the fitted coefficient and intercept, respectively. The use of the term (*PI* + 1) in Eq. (5.3) was not strictly necessary for achieving the most reliable statistical model for exponent *b*; however, this term is preferred owing to its use in subsequent nonlinear regression models for *CRR* (where *PI* = 0 presents numerical challenges), allows consistency between the suite of statistical models described herein, and does not impact the statistical rigor of the estimate b^*. Table 5.1 presents the fitted coefficient and intercept along with the corresponding SE, *t*-statistic (an estimate of precision in the fitted coefficient or intercept in terms of the standard normal variate), and the corresponding p-values. The fitted coefficient and intercept for the exponent b model are determined to be statistically significant as characterized by t-statistics larger than +/- 2 standard normal variates, and p-values significantly smaller than 0.05.

Table 5.1 Fitted elements and calculated statistical metrics for exponent *b* model over *training dataset* corresponding to $N_{\gamma=3\%}$.

Eq. #	Proposed Model	Fitted Parameters	Parameter Estimate	SE	*t*-statistic	*p*-value
Eq. (5.3)	$b^* = a_0 \cdot (PI + 1) + a_1$	a_0	-0.0030	0.00062	-4.78	4.48e-04
		a_1	0.1470	0.01142	12.88	2.20e-08

Figure 5.3a illustrates the accuracy of Eq. (5.3) to estimate exponent b through the comparison against the *training dataset*, consisting of 14 suites (i.e., n = 14) of stress-controlled cyclic tests of silts specimens sharing a narrow range in soil index properties and stress histories. The results indicate that the model provides unbiased estimates of exponent b on average (i.e., $\bar{\lambda}$ = 1.00), in general agreement with the experimental data used to train the model (R^2 = 0.66, COV_λ = 0.19). Figure 5.3b presents an investigation into model validation through the evaluation of the accuracy and uncertainty in the predicted exponent b through comparison to the independent *testing dataset* with n = 6. The results indicate that the proposed model maintained its prediction robustness with a larger R^2 = 0.85 than that of the *training dataset*, a slight tendency for overprediction ($\bar{\lambda}$ = 0.92) of b, and similar variability (COV_λ = 0.19). Note that the observed divergence between the measured and calculated b in Figure 5.3 stems in part from differences in soil fabric, inherent variability in the silt specimens, depositional environment, and other factors which are not captured by the proposed, univariate Eq. (5.3).

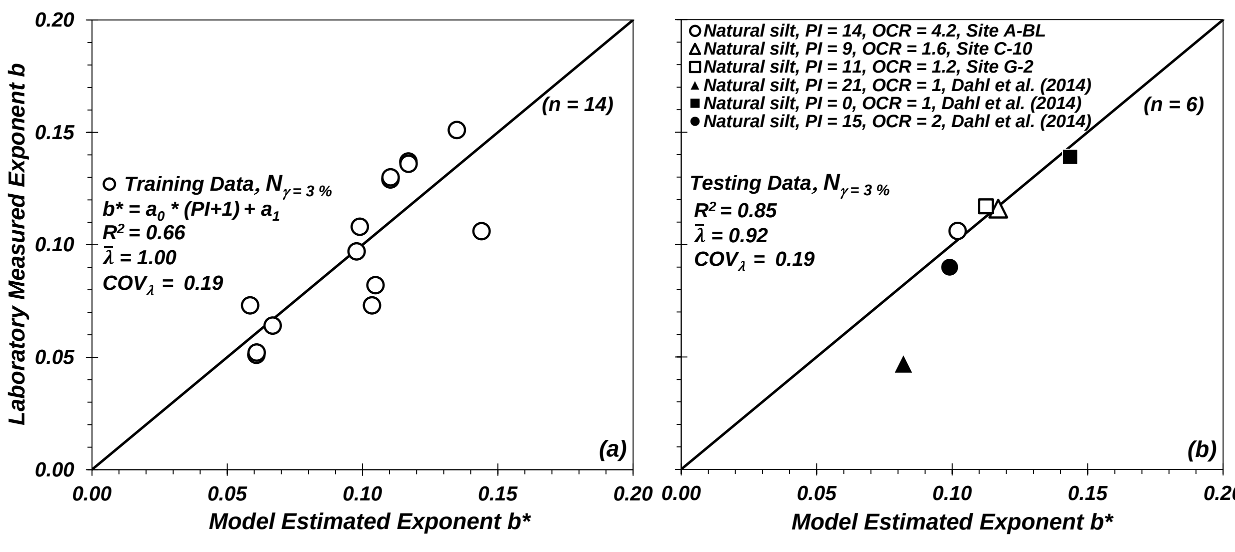

Figure 5.3 Comparison of the experimental and model-calculated exponent *b* for the: (a) *training dataset*, and (b) *testing dataset*.

5.2.3 Finalized Model for *CRR* Power Law Exponent *b*

Following validation of Eq. (5.3) against the *testing dataset*, its functional form was retrained using *combined dataset* for $N_{\gamma=3\%}$ with n = 20 to develop the model with the most robust fitted parameters. Table 5.2 summarizes the finalized fitted parameters for Eq. (5.3) and statistical metrics developed using the *combined dataset*. The results indicate that the contribution of the fitted coefficient and intercept is still statistically significant as characterized by large *t*-statistics and significantly small *p*-values.

Table 5.2 Fitted model parameters and statistical metrics for the finalized model for *CRR* power law exponent *b* trained using the *combined dataset* corresponding to $N_{\gamma=3\%}$.

Proposed Model[1]	Fitted Parameters	Parameter Estimate	SE	*t*-statistic	*p*-value
$b^* = a_0*(PI+1) + a_1$	a_0	-0.0031	0.00051	-6.17	8.03e-06
	a_1	0.1470	0.00868	16.94	1.66e-12

[1] Eq. (5.3) should be limited to $b \geq 0.05$

Figure 5.4 compares the estimate b^* calculated using the finalized fitted model parameters against the experimental *b* represented within the *combined dataset*, suggesting that the simple univariate Eq. (5.3) is able to provide a nearly unbiased ($\bar{\lambda}$ = 1.01), sufficiently accurate (R^2 = 0.69), estimate of exponent *b*, with variability that is lower than many available geotechnical models ($COV_{\bar{\lambda}}$ = 0.18). Note that the *combined dataset* includes just one suite of cyclic testing data characterized with b < 0.05 (i.e., [*PI*, *b*] = [21, 0.047]; Series PC-0A, Dahl et al. 2014) which represents a suite responsible for one of the larger model residuals (i.e., errors). Accordingly, it is recommended at this time to limit exponent $b \geq 0.05$ in the application of the proposed model until other data become available and the suitability of Eq. (5.3) can be reinvestigated.

Figure 5.5 presents the variation of b^*versus *PI*, restricted to $b \geq 0.05$. As shown in Figure 5.5, b^* reduces with *PI*; this indicates that as the clayey mineral content of a given specimen increases, the sensitivity of cyclic resistance to the number of loading cycles reduces, and hence the *CRR-N* curve becomes less curved (i.e., flatter). This is generally consistent with reduced sensitivity of the magnitude scaling factor proposed by Boulanger and Idriss (2015) with exponent *b*, as described in greater detail in Chapter 6. Furthermore, Eq. (5.3) and the finalized fitted model parameters together suggest that specimens with *PI* = 0 are characterized with *b* = 0.144. It is important to recognize that this estimate of *b* is suitable for silty sand (SM) with *FC* > 30% and nonplastic sandy silt (ML) with I_c > 2.6 (Stuedlein et al. 2023), and should not be applied to soils that are not consistent with the characteristics of the *combined dataset.* Further, the cone tip resistance of the soils within the *combined dataset* should be referenced (Stuedlein et al. 2023) for these nonplastic materials given that relative density has been shown to influence exponent *b* (Boulanger and Idriss 2015). Finally, it is recognized that uncertainty in b^* exists; the $COV_{\bar{\lambda}}$ for Eq. (5.3) can be used to estimate appropriate lower- and upper-bound estimates of b^* for sensitivity analyses.

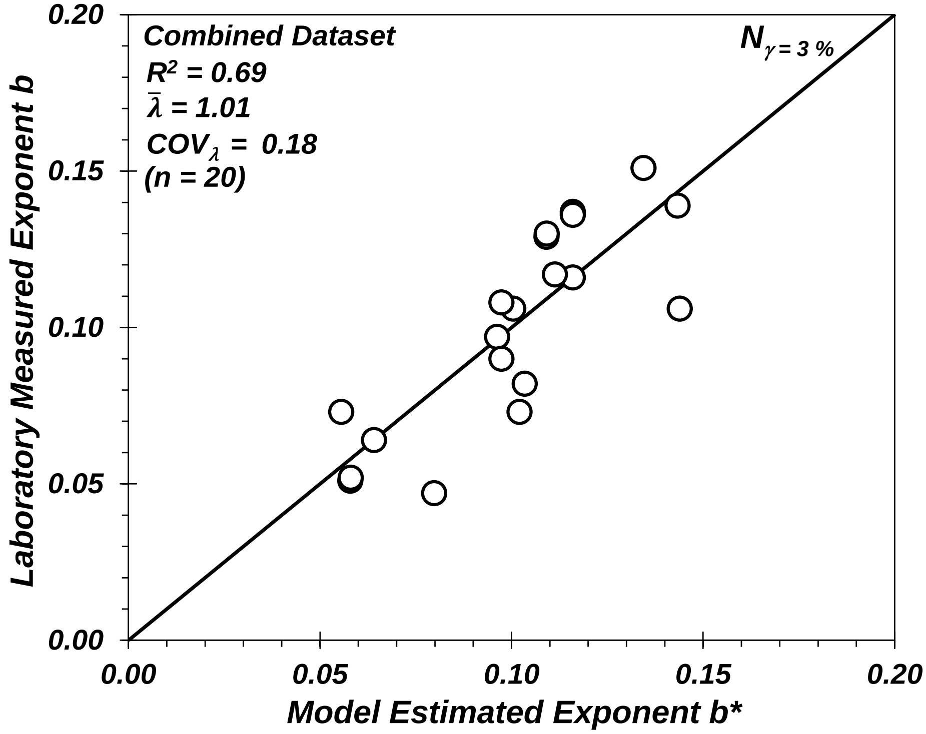

Figure 5.4 Comparison of the experimental and estimated exponent *b* fitted using the *combined dataset* and finalized, fitted model parameters (Table 5.2).

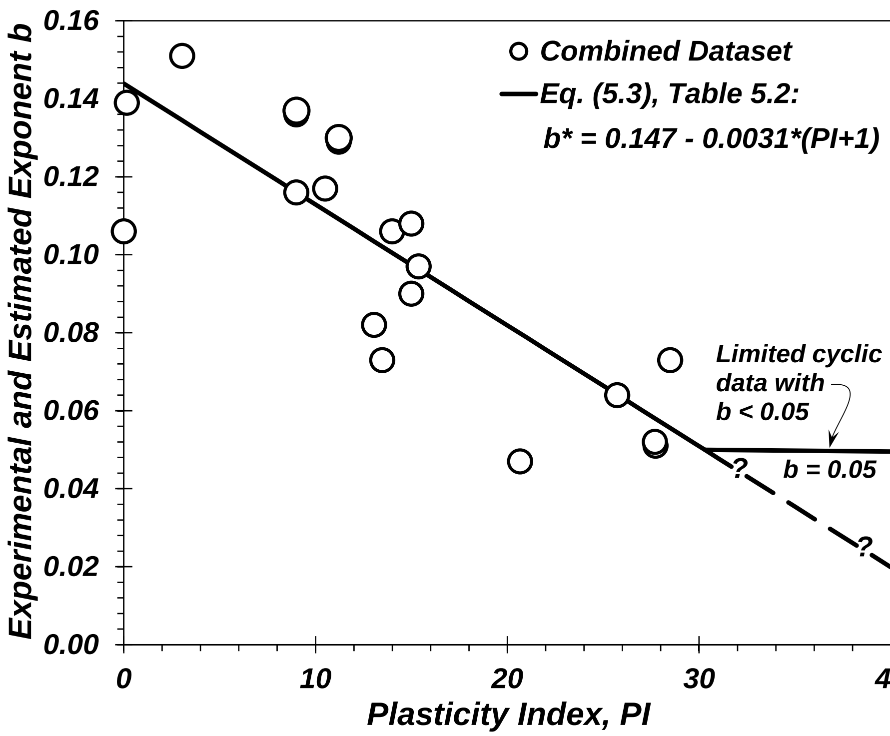

Figure 5.5 Variation of CRR power law exponent *b* and estimate *b with *PI* using Eq. (5.3) and finalized, fitted model parameters (Table 5.2).**

5.3 STATISTICAL MODELS FOR ESTIMATION OF THE CYCLE- AND STRAIN-DEPENDENT CYCLIC RESISTANCE RATIO (*CRR*)

In addition to the parameters (i.e., *e*, *OCR*, *PI*) governing cyclic resistance described in the previous section, it is necessary to consider the number of loading cycles, *N*, which has been correlated to earthquake magnitude (Seed et al. 1975, Idriss 1999, Boulanger and Idriss 2015). Owing to the dependence of the cyclic resistance ratio, *CRR*, to the maximum strain amplitude selected as a cyclic failure criterion, strain-dependent *CRR*s are likewise of interest. The development of a statistical model to capture *N* and γ is described herein. A detailed presentation of the statistical regression analyses is provided for the typical cyclic strain failure criterion of $\gamma = 3\%$ (i.e., *CRR*-*N* corresponding to $\gamma = 3\%$); identical statistical techniques were applied to other shear strain amplitudes following identification of the most-suitable regression model for $\gamma = 3\%$, the results of which are summarized herein.

5.3.1 Initial Investigation of Possible Predictor Variables

Figure 5.6 presents univariate scatter plots of the laboratory-based *CRR* represented within the *training dataset* for *CRR* corresponding to $N_{\gamma=3\%}$ versus *e*, *PI*, *OCR*, and *N*. Weak linear correlation exist between *e* and *CRR* and *PI*, weak nonlinear trend between *OCR* and *CRR*, and moderate nonlinear relationship between *N* and *CRR* as characterized by the corresponding R^2. Conclusions of contributions to *CRR* using univariate relationships are not appropriate in view of the interaction between the variables governing cyclic resistance, as explored further below, but simply provide the basis for the staged regression analysis conducted.

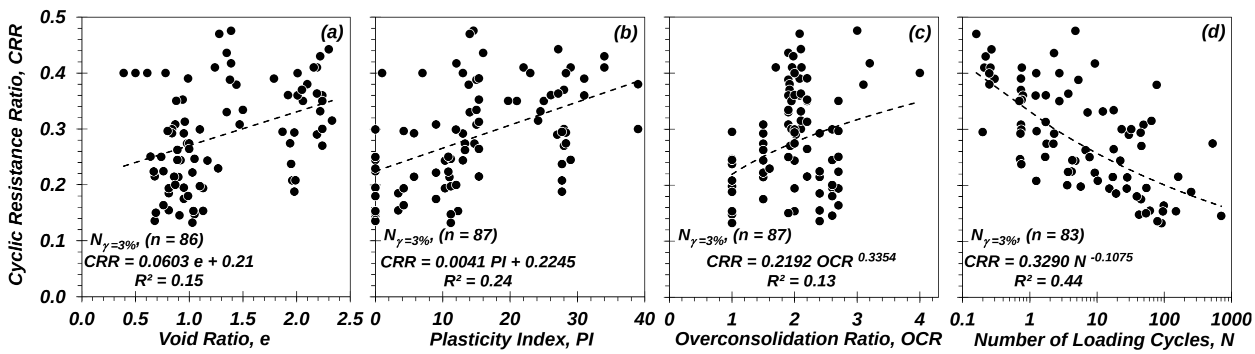

Figure 5.6 Variation of *CRR* within the *training dataset* with respect to: (a) void ratio, *e*, (b) plasticity index, *PI*, (c) overconsolidation Ratio, *OCR*, and (d) number of loading cycles, *N*.

The preliminary contribution of each predictor variable to *CRR* was examined separately using four univariate linear models with coefficient a_0 and intercept of a_1 with the results summarized in Table B3. The analysis indicates that although the observed correlations are weak to moderate, all of the predictor variables are statistically significant (i.e., *p*-value < 0.05). The scatter in Figure 5.6 and statistical significance suggests the potential for statistical interaction and that transformation of the predictor variables within nonlinear combinations can provide a stronger model with which to estimate *CRR*. The presence of multicollinearity between *e*, *PI*, *OCR*, and *N* was assessed using a single multivariate linear regression model, given by:

$$CRR = b_0 \cdot e + \ b_1 \cdot PI + b_2 \cdot OCR + b_3 \cdot N + b_4 \tag{5.4}$$

where b_0, b_1, b_2, and b_3 are the fitted coefficients and b_4 is the fitted intercept.

The calculated VIF for Eq. (5.4) are summarized in Table B4, and consistent with the correlation between *e* and *PI* (Fig. 5.2), the VIF of 4.21 and 4.17 returned for e and *PI* in Eq. (5.4) suggests the potential for multicollinearity to negatively impact the statistical robustness of a regression model implementing both of these predictor variables. Given the ease with which *PI* can be obtained (relative to void ratio), *e* was removed from Eq. (5.4) to produce a new multiple regression model and the VIF redetermined:

$$CRR = b_1 \cdot PI + b_2 \cdot OCR + b_3 \cdot N + b_4 \tag{5.5}$$

where b_1, b_2, and b_3 are the fitted coefficients and b_4 is the fitted intercept. The check against multicollinearity of predictor variables shown in Table B4 confirm that *PI*, *OCR*, and *N* are independent. Thus, *PI*, *OCR*, and *N* are selected for identification of a suitable, nonlinear function which can reliably produce *N*- and γ-dependent *CRR*.

5.3.2 Validation of the Functional Form for *CRR* Models for $N_\gamma = 3\%$

Numerous candidate regression models were examined using transformations and nonlinear combinations of the predictor variables to identify the simplest model with highest accuracy. The model exhibiting the best performance and which could leverage the trend in exponent *b* described in Section 5.2.3 was selected for development using the *training dataset* and validation using the *testing dataset* for assessment of suitability and finalization.

The SHANSEP framework (Ladd and Foott 1974) was identified as an appropriate starting point for a suitable nonlinear combination of predictor variables to be used in the regression model. For a given soil deposit characterized with a relatively narrow range in *PI*, the vertical effective stress-normalized undrained shear strength, s_u/σ'_{v0}, of a plastic soil can be expressed as a unique function of its *OCR* as follows:

$$\frac{s_u}{\sigma'_{v0}} = S \cdot OCR^m \tag{5.6}$$

where $S = s_u/\sigma'_{vc}$ for OCR = 1 and m is the slope of the s_u/σ'_{v0} versus OCR curve in semi-logarithmic space (Ladd 1991). Considering that Eq. (5.6) was developed to estimate the monotonic undrained shear strength of a given soil deposit characterized with a representative plasticity index, the following elements were considered during the development of a nonlinear regression model to estimate cyclic resistance:

- For a given *OCR*, s_u/σ'_{v0} is a unique function of *PI* (Ladd 1991). Therefore, it is appropriate to incorporate *PI* in a quasi-SHANSEP framework to predict the cyclic response of fine-grained soils with varying plasticity; and,
- The monotonic undrained shear strength, s_u, used in the SHANSEP framework could be replaced with $CRR = \tau_{cyc}/\sigma'_{v0}$, and the corresponding power-law in the form of $a \cdot N^{-b}$ can be incorporated in the right-hand side of Eq. (5.6).

By addressing the two elements listed above and replacing s_u/σ'_{v0} with τ_{cyc}/σ'_{v0} in Eq. (5.6) a potentially suitable functional form of a regression model can be expressed as follows:

$$CRR^* = c_0 * (PI+1)^{c_1} * OCR^{c_2} * N^{-b^*} \tag{5.7}$$

where $CRR^*$is the estimate of *CRR* for the number of loading cycles *N* to reach the cyclic shear strain failure criterion of $\gamma = 3\%$ (i.e., $N_{\gamma=3\%}$), c_0 is the fitted coefficient, c_1 and c_2 are fitted exponents, and $b^*$is the exponent *b* estimated using Eq. (5.3) as summarized in Table 5.2. The fitted parameters in Eq. (5.7) were calculated for $N_{\gamma=3\%}$ using the nonlinear least square (NLS) optimization function *nls* in software package *R* using the *training dataset*.

Table 5.3 presents the summary of the statistical analyses which indicate that the fitted parameters are statistically significant with *p*-values << 0.05. Furthermore, Eq. (5.7) confirms that *PI* affects both the magnitude of *CRR* at *N* = 1 and the curvature of the *CRR*-*N* relationship. Figure 5.7 presents the goodness-of-fit for the provisional estimates of CRR^* against the *CRR* for $N_{\gamma=3\%}$ contained in the *training dataset* (Fig. 5.7a) and validation of the trained model against the *CRR* contained within the independent *testing dataset* (Fig. 5.7b). Equation (5.7) provides relatively unbiased ($\bar{\lambda}$ = 1.01) estimates of *CRR* corresponding to $N_{\gamma=3\%}$ with R^2 = 0.74 and low variability as characterized by COV_λ = 0.17 for the *training dataset* (Fig. 5.7a). Prediction accuracy of the preliminary fitted model parameters ascertained using the independent *testing dataset* indicates slightly biased estimates ($\bar{\lambda}$ = 1.03) with lower variability (i.e., COV_λ = 0.13) and higher overall accuracy (R^2 = 0.85; Fig. 5.7b).

Table 5.3 Summary of performance of Eq. (5.7) for the estimation of *CRR* corresponding to $N_{\gamma=3\%}$ with respect to the *training dataset*.

Proposed Model	Fitted Parameter	Parameter Estimate	SE	*t*-statistic	*p*-value
$CRR^* = c_0 * (PI+1)^{c_1} * OCR^{c_2} * N^{-b^*}$	c_0	0.1880	0.0167	11.24	2.00E-16
	c_1	0.1101	0.0227	4.86	5.86E-06
	c_2	0.4321	0.0626	6.90	1.10E-09

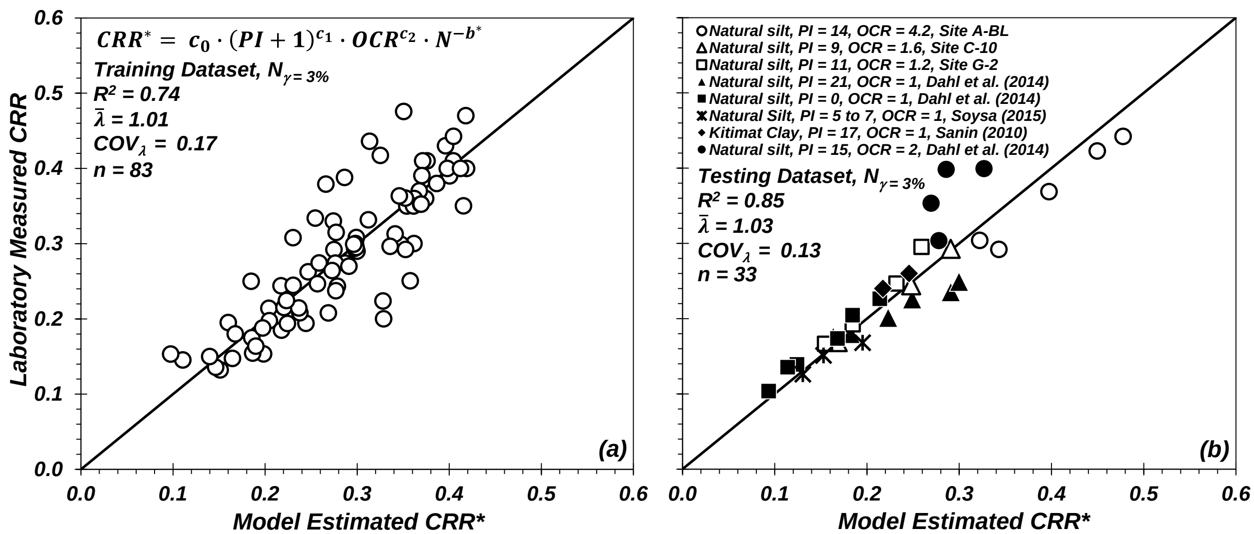

Figure 5.7 Comparison of the experimental *CRR* and estimated *CRR corresponding to $N_{\gamma=3\%}$ for the: (a) *training dataset*, and (b) *testing dataset.***

Some of the average bias observed following application of Eq. (5.7) to the *testing dataset* may be attributed to the *CRR* for specimens reported by Dahl et al. (2014), characterized with *PI* = 15 and *OCR* = 2 (Fig. 5.7b). The underestimation of *CRR* for these specimens might have developed due to differences between the consolidation method implemented by Dahl et al. (2014) and the majority of specimens included within the *training dataset*. The stress state for the majority of specimens in the *training dataset* had been developed using the recompression technique (i.e., consolidating specimen to the estimated *in-situ* vertical effective stress), selected owing to the use of high-quality specimens and observations that excessive consolidation strains that developed when the preconsolidation stress might be uncertain could lead to cyclic resistances which may not be representative of that in the source soil deposit (Stuedlein et al. 2023). The specimens reported by Dahl et al. (2014) were consolidated to vertical effective stresses larger than or equal to the preconsolidation pressure, resulting in a corresponding reduction in a void ratio, and an apparent increased cyclic resistance relative to that inferred from the CRR estimated from the provisionally-trained Eq. (5.7). The final set of fitted model parameters for Eq. (5.7) developed using the *combined dataset* is presented in Section 5.3.3, below.

5.3.3 Finalized Models for Cycle- and Strain-Dependent *CRR*

In the previous section, the functional form of Eq. (5.7) was validated using the independent *testing dataset* for $N_{\gamma=3\%}$. The results of analyses indicated that the model is robust, statistically significant, and sufficiently accurate to predict *CRR* for the silty soils targeted in this study. Thus, Eq. (5.7) was evaluated to obtain fitted model parameters using the *combined dataset* for the cyclic shear strain failure criteria of $N_{\gamma=0.5\%}$, $N_{\gamma=1\%}$, $N_{\gamma=2\%}$, $N_{\gamma=3\%}$, $N_{\gamma=3.75\%}$, $N_{\gamma=5\%}$, $N_{\gamma=8\%}$, $N_{\gamma=10\%}$ using the procedures described above. The fitted model parameters, standard errors, *t*-statistics, and *p*-values determined from the statistical analyses of Eq. (5.7) are summarized in Table 5.4. The fitted model parameters for the predictor variables (e.g., *PI, OCR*) are statistically significant over a wide range in N_γ, interpreted from large *t*-statistics and small *p*-values, justifying the general applicability of Eq. (5.7) over a large range in shear strain.

Table 5.4 Summary of the finalized fitted model parameters and associated statistical metrics for use with Eq. (5.7) for different cyclic shear strain failure criteria.

Cyclic Shear Strain Failure Criterion	Fitted Parameter	Parameter Estimate	SE	*t*-statistic	*p*-value
$N_{\gamma=1\%}$	a_{02}	0.1205	0.0108	11.20	2.00e-16
	a_{12}	0.1842	0.0268	6.87	5.09e-10
	a_{22}	0.4379	0.0502	8.73	5.21e-14
$N_{\gamma=2\%}$	a_{02}	0.1760	0.0124	14.24	2.00e-16
	a_{12}	0.1059	0.0210	5.05	1.91e-06
	a_{22}	0.4072	0.0425	9.58	5.38e-16
$N_{\gamma=3\%}$	a_{02}	0.1980	0.0115	17.22	2.00e-16
	a_{12}	0.0988	0.0178	5.54	1.99e-07
	a_{22}	0.4046	0.0365	11.09	2.00e-16
$N_{\gamma=3.75\%}$	a_{02}	0.1911	0.0113	16.98	2.00e-16
	a_{12}	0.1337	0.0184	7.25	4.69e-11
	a_{22}	0.3679	0.0340	10.84	2.00e-16
$N_{\gamma=5\%}$	a_{02}	0.2017	0.0131	15.40	2.00e-16
	a_{12}	0.1353	0.0206	6.58	2.79e-09
	a_{22}	0.3532	0.0398	8.87	5.52e-14
$N_{\gamma=8\%}$	a_{02}	0.2042	0.0162	12.65	2.00e-16
	a_{12}	0.1428	0.0244	5.86	2.30e-07
	a_{22}	0.3428	0.0459	7.47	4.71e-10
$N_{\gamma=10\%}$	a_{02}	0.2040	0.0191	10.66	6.73e-14
	a_{12}	0.1517	0.0282	5.37	2.62e-06
	a_{22}	0.3508	0.0593	5.92	4.13e-07

Figure 5.8 compares the performance to estimate the laboratory-observed *CRR* for soil specimens represented within the *combined dataset* using the final fitted parameters in Table 5.4 with Eq. (5.7) for various magnitudes of N_γ and corresponding to γ ranging from 1 to 10%. In general, relatively unbiased estimates of *CRR on average* are obtained for the selected range in shear strain, with $0.99 \leq \bar{\lambda} \leq 1.05$. Upon closer inspection, the fitted model parameters for smaller magnitudes of shear strain, $N_{\gamma\leq2\%}$ provide *CRR* estimates with lower accuracy and larger uncertainty than those estimated for $N_{\gamma>2\%}$. This may be largely attributed to the fact that silty soils with the range in index properties and stress history represented in the *combined dataset* can readily achieve

strains of 0.5 to 2% with relatively few cycles or a fraction of a loading cycle (depending on the *CSR*), in contrast to medium dense to dense clean sands, which require a significantly greater number of loading cycles before substantial stiffness deterioration develops. For example, 81 of 105 specimens with a wide range in properties (i.e., *OCR*, *PI*) generated γ = 1% in $N \leq 1$. This stems in part from the common goal of cyclic testing programs to achieve shear strains of *at least* 3% (i.e., the typical cyclic shear strain failure criterion), which necessitates application of *CSR*s that can trigger 3% shear strain in reasonable number of loading cycles ($1 \leq N \leq 300$), and thus small *N* are required trigger smaller magnitudes of shear strain. Therefore, statistical models will have difficulty parsing the role of variations in independent variables which may influence the variation in *CRR*. This observation explains in part some of the limitations of the statistical models, described in detail in Section 5.3.4.

The estimate of *CRR* improves with increases in shear strain amplitude, with nearly unbiased estimates of *CRR* on average ($0.99 \leq \overline{\lambda} \leq 1.01$) for $N_{\gamma>2\%}$. For example, for the cyclic shear strain failure criterion of γ = 5%, $N_{\gamma=5\%}$, the corresponding fitted parameters for Eq. (5.7) produces an R^2 = 0.78, $\overline{\lambda}$ = 1.00, COV_{λ} = 0.15 (Fig. 5.8). For ease of use in practice, equations for the shear strain-dependent model parameters (c_i) for Eq. (5.7) for use in estimating *CRR* for the selected shear strain amplitudes are presented in Section 5.3.4, below.

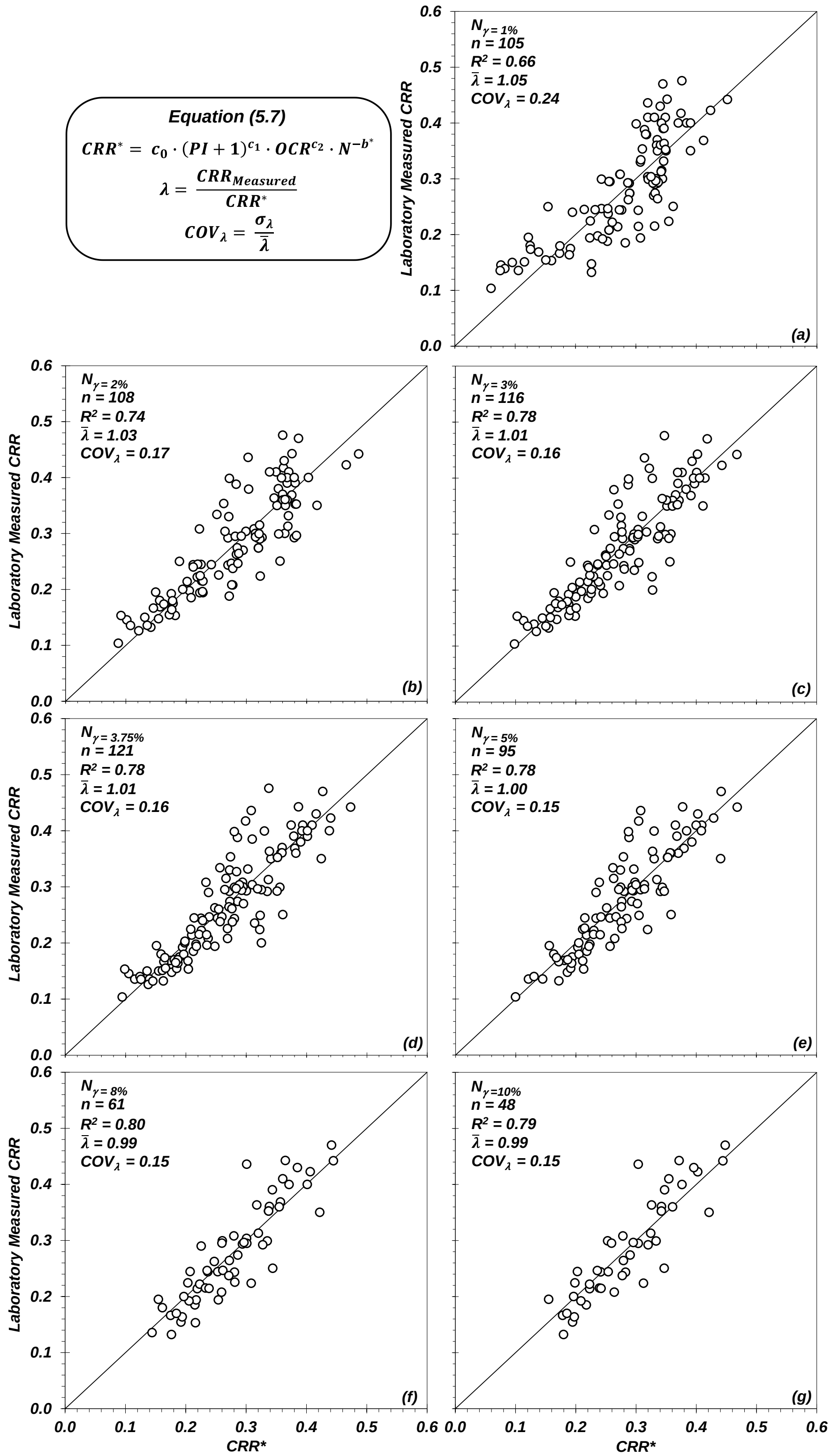

Figure 5.8 Comparison of the experimental *CRR* and model-estimated *CRR using the finalized, fitted model parameters (Table 5.4) for cyclic shear strain failure criteria of: (a) 1%, (b) 2%, (c) 3%, (d) 3.75%, (e) 5%, (f) 8%, and (g) 10%.**

5.3.4 Typical Trends and Limitations in *CRR* Estimates

The accuracy of the *CRR* estimated using Eq. (5.7) is influenced by the limitations in data availability at a particular shear strain magnitude, and the model formulation and underlying assumptions. The effect of data scarcity for certain independent model parameters is highlighted to guide appropriate use in practice. Figure 5.9 presents the empirical (sample) cumulative distribution functions (CDFs) for *PI*, σ'_{vc}, and *OCR* within the *combined dataset* used to generate CRR^* for each strain amplitude. The range in *PI* in the *combined dataset* is 0 to 39, with median *PI* = 11 for all cyclic shear strain failure criteria. Specimens which achieved $N_{\gamma=8\%}$ and $N_{\gamma=10\%}$ are the fewest regardless of *PI* (Fig. 5.9a). Nonplastic (*PI* = 0) specimens comprise 8 to 13% of the data depending on the cyclic shear strain failure criterion. Specimens with *PI* > 30 are even more scarce, representing about 5 to 8% of the total specimens for N_γ corresponding to γ ranging from 1 to 3.75%, reducing to 1.5 to 2% of total specimens as γ increases. Thus, use of Eq. (5.7) should be accompanied with the recognition that the accuracy of the *CRR* estimates may be poorest for high-*PI* silts (i.e., *PI* > 30).

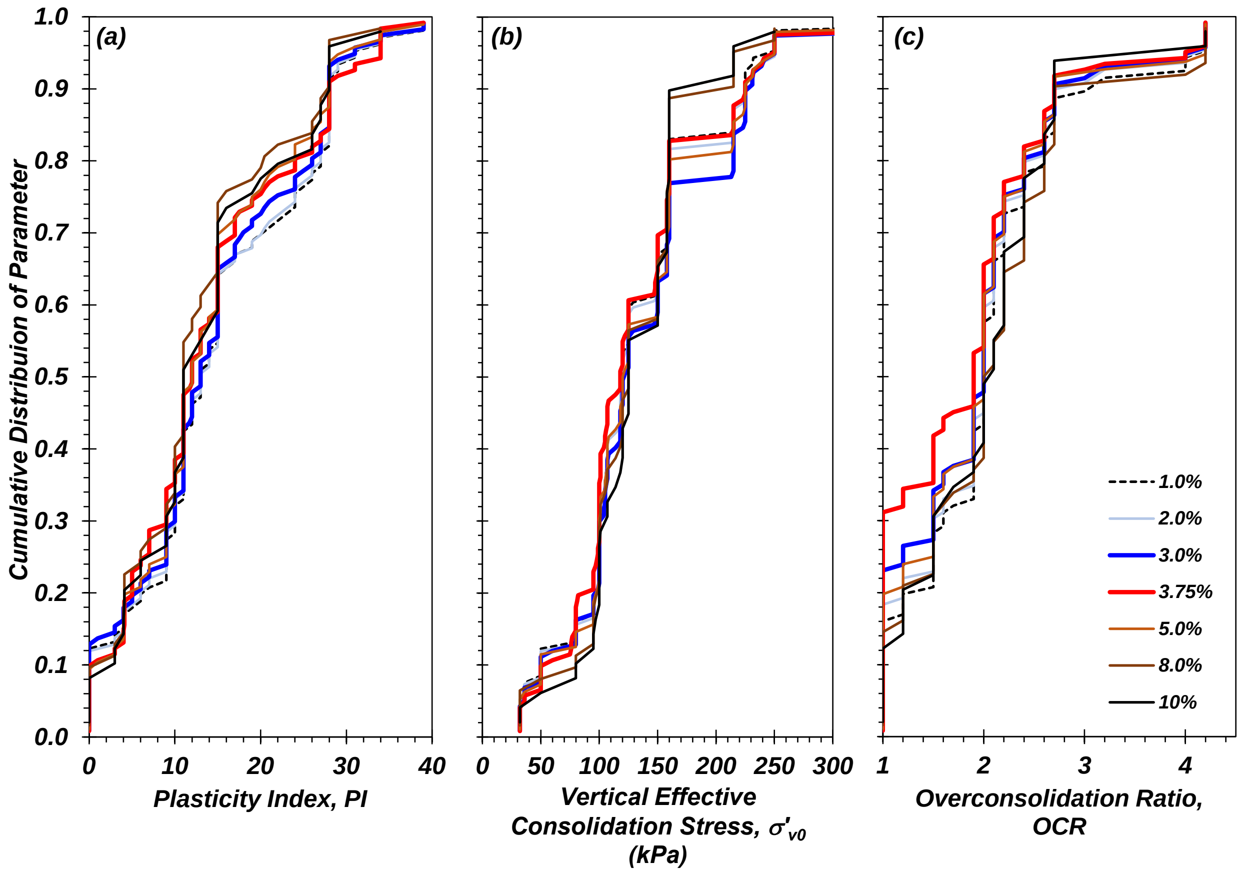

Figure 5.9 Distribution of relevant factors influencing the cyclic resistance of the soils within the *combined dataset*: (a) plasticity index, *PI*, (b) vertical effective consolidation stress, σ'_{vc}, and (c) overconsolidation ratio, *OCR*.

Furthermore, it should be noted that the effects of stress-dilatancy (i.e., high overburden stress effects) have not been explicitly treated in the development of these regression models, and are only included indirectly. The median σ'_{vc} represented in the *combined dataset* ranges narrowly from 118 to 125 kPa across all cyclic shear strain failure criteria, with minimum and maximum σ'_{vc} ranging from 32 to 450 kPa for CRR corresponding to γ = 1 to 5% and reducing to 32 to 250 kPa for larger γ (Fig. 5.9b). However, application of Eq. (5.7) to soils with σ'_{vc} greater than approximately 225 kPa should proceed with significant caution, particularly for cyclic shear strain failure criteria exceeding 5% due to: (1) the sharp reduction in data representation beyond this stress magnitude, and (2) the expectation that *CRR* will reduce beyond this threshold stress magnitude owing to increased contractive behavior expected as σ'_{vc} increases, based in part on observations noted in a forthcoming publication by the writers.

Figure 5.9c presents the CDF for *OCR* as a function of the cyclic shear strain failure criteria considered herein. The median *OCR* ranges narrowly between 1.9 and 2.1 across the range in cyclic shear strain failure criteria. Normally-consolidated, *NC*, soil specimens comprise 12 to 31% of the data considered in the two regression models, with relatively fewer *NC* specimens for smaller and more extreme cyclic shear strain failure criteria. In contrast, the *CRR* corresponding to γ = 3 and 3.75% provides the greatest representation of *NC* specimens. With approximately 90% of specimens characterized with an *OCR* of approximately 3.0 or smaller, caution should be used when estimating cyclic resistance for soils with *OCRs* larger than 3.0.

Comparison of the trends in the typical model estimates serve to further illustrate their appropriateness and/or potential shortcomings with Eq. (5.7). Figure 5.10a presents the variation of the estimated $CRR\text{-}N_{\gamma=3\%}$ curves for intact silts with different *PI*s and *OCR*s and for a cyclic shear strain failure criterion of γ = 3%. For a given $N_{\gamma=3\%}$, *CRR** increases with increases in *PI* and *OCR*, as expected. The curvature of the *CRR-N* curves estimated using Eq. (5.7) decreases with increases in *PI* in accordance with experimental evidence (Fig. 5.5; Eq. 5.3). Additionally, increases in *OCR* appear to produce the largest increase in *CRR*, confirmed through comparison of exponent c_2 on *OCR* (Table 5.4), which is the largest fitted exponent in the proposed models (*n.b.*, the magnitude of the exponent relates to its strength as a predictor variable). For example, the finalized fitted model parameters for Eq. (5.7) returns an increase in *CRR** of 32% as *OCR* increases from 1.5 to 3.0 and $N_{\gamma=3\%}$ = 30, respectively. Furthermore, the estimated *CRR* is sensitive to plasticity: *CRR** increases significantly from *PI* = 0 to *PI* = 10, but the incremental increase in *CRR** reduces with similar incremental increases in *PI*. The increase in cyclic resistance relative to the increase in *PI* over the range (0, 10) appears to contradict trends of the effect of *PI* on cyclic strength noted by Dahl et al. (2018) and Stuedlein et al. (2023a). However, the statistical interaction of *OCR* with *PI* on *CRR* was not explicitly considered by Dahl et al. (2018) and Stuedlein et al. (2023a), the lack of controlling for *OCR* appears to led to greater uncertainty in the *CRR* for the low *PI* range. Note that the exponent on *PI* (i.e., fitted parameter c_1) is less than half of that on *OCR* (i.e., c_2) over the range in cyclic shear strain failure criteria considered.

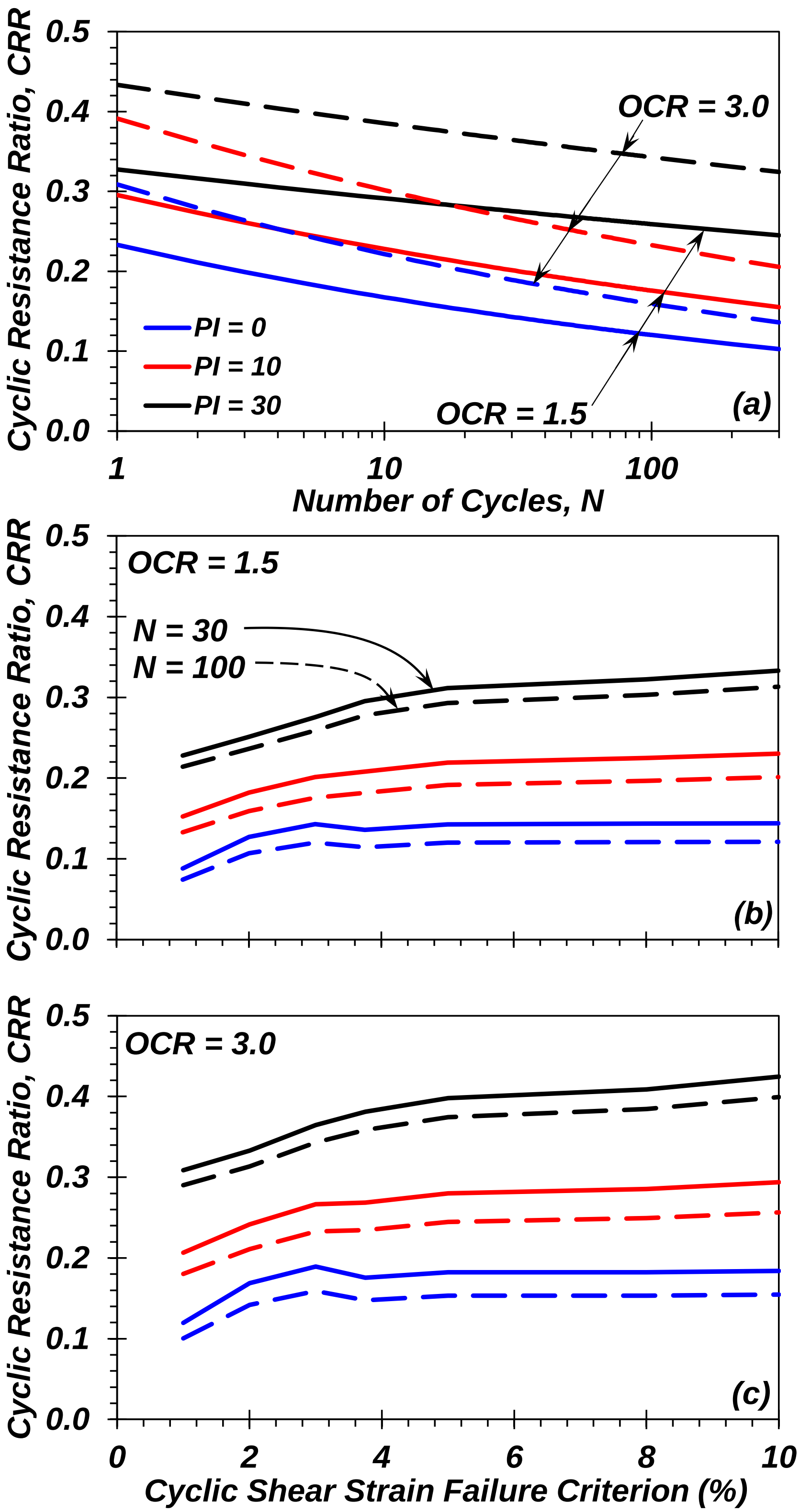

Figure 5.10 Variation of estimated cyclic resistance ratio, *CRR*, computed using Eq. (5.7) for $N_{\gamma=3\%}$ with (a) number of cycles, and cyclic shear strain failure criterion for (b) *OCR* = 1.5, and (c) *OCR* = 3.0 for *PI* of 0, 10, and 30.

Figure 5.10b and 5.10c present the variation in the *CRR* estimated for the various magnitudes of cyclic shear strain failure criteria at N = 30 and 100 and for *OCR* = 1.5 and 3.0, and *PI* of 0, 10, and 30. For given *PI* and *OCR*, the estimated *CRR* decreases with increasing N and increases with the shear strain amplitude representing cyclic failure, respectively. For example, for *OCR* = 1.5 and *PI* = 30, CRR^* estimated corresponding to $N_{\gamma=3\%}$ decreases from 0.275 to 0.259 as N increases from 30 to 100, whereas for N = 30, the estimated *CRR* increases from 0.275 to 0.322 as N_γ increases from 3 to 8% (Fig. 5.10b).

Whereas both models clearly capture the reduction in *CRR* with N across all *PI* and *OCR*, the effect of scarcity or under-represented input variables for nonplastic silts is clearly observed for cyclic shear strain failure criteria greater than 3%, where a reduction in the large-strain *CRR** is noted (Figs. 5.10b and 5.10c). There exists no phenomenological justification for the reduction in estimated *CRR* as the cyclic shear strain failure criteria exceeds 3% in stress-controlled cyclic DSS test results. The total amount of data available to fit Eq. (5.7) is maximum (n = 121) for γ = 3.75%, and reduces to just 48 specimens for γ = 10%. The number of nonplastic specimens subjected to γ > 3% reduces from 13% (at γ = 3%) of the total number to 10% or less for larger shear strains, with just four nonplastic specimens at γ = 10% in the *combined dataset*. Critically, there are no nonplastic specimens with *OCR* > 2.7 in the *combined dataset*. Thus, it appears that the lack of sufficient data for nonplastic specimens, and particularly those with large *OCR*s results in poor estimates of *CRR* developed using Eq. (5.7), with the impact to accuracy shared more or less equally between the two models. Although it is likely that the *CRR* at γ = 3% would provide an appropriate representation of the *CRR* at larger shear strains for a given *OCR* and N, use of these models where data is poor should proceed cautiously.

Note that Eq. (5.7) was trained on data representing a cyclic loading frequency of 0.1 Hz. The *CRR* can therefore be increased by 9% for application to ground motions with a typical predominant frequency of 1 Hz (Idriss & Boulanger 2008).

Table 5.5 presents regression equations for the shear strain-dependent model parameters c_0, c_1, and c_2 for use in estimating *CRR* for the selected shear strain amplitudes regressed against using Eq. (5.7). These equations were developed through ordinary least squares regression on the fitted model parameters tabulated in Table 5.4. Goodness-of-fit metrics for each equation are tabulated in Table 5.5 for inspection by the user, and achieve satisfactory fits for the selected shear strain amplitudes.

Table 5.5 Shear strain-dependent model parameters for use with Eq. (5.7) for the selected amplitudes of shear strain.

Fitted Parameter	Coefficient of Determination, R^2	Mean Bias, $\bar{\lambda}$	Coefficient of Variation in Bias, COV_λ	Sum of Squared Errors, SSE
$c_0 = \dfrac{0.581 \cdot \gamma^{2.159}}{1.99 + 2.831 \cdot \gamma^{2.159}}$	0.987	0.999	0.017	6.97E^{-05}
$c_1 = \dfrac{1.66E^5 + 4.66E^4 \cdot \gamma^{-5.84}}{1.115E^6 + 5.26E^{-5} \cdot \gamma^{\left(\frac{71.72}{\gamma} - 2.96\right)}}$	0.974	1.000	0.032	1.28E^{-04}
$c_2 = 0.343 + \dfrac{0.093 \cdot \gamma^{-3.42}}{3.06^{-3.42} + \gamma^{-3.42}}$	0.945	0.999	0.022	4.31E^{-04}

5.4 STATISTICAL MODEL FOR ESTIMATION OF CYCLIC STRENGTH RATIO ($\tau_{cyc}/s_{u,DSS}$)

5.4.1 Initial Investigation of Possible Predictor Variables

A relationship to estimate the cyclic strength ratio, $\tau_{cyc}/s_{u,DSS}$, for nonplastic to plastic silt at $N_{\gamma=3\%}$ corresponding to N = 30 and a corrected loading frequency of 1 Hz was described in Section 3.3.2 (Eq. 3.1; Stuedlein et al. 2023). Equation (3.1) can be used within the Simplified Method to quantify the cyclic resistance of soil at a particular N = 30, however, it is necessary to evaluate cyclic resistance of soils at the desired N corresponding to design earthquake magnitude, M_w. Thus, statistical models to provide estimates of $\tau_{cyc}/s_{u,DSS}$ for a wide range of N are developed herein for use in design practice.

Similar to the estimates of *CRR* developed in Section 5.3, *e*, *OCR* and *PI* are considered the main governing parameters that serve to predict the variation of $\tau_{cyc}/s_{u,DSS}$ with *N*. Figure 5.11 presents the variation of laboratory-based $\tau_{cyc}/s_{u,DSS}$ contained within the *training dataset* corresponding to $N_{\gamma=3\%}$ with respect to the identified parameters, indicating that there is a weak linear correlation between $\tau_{cyc}/s_{u,DSS}$ versus *e* and *OCR*, with R^2 of 0.10 and 0.04, respectively (Figs. 5.11a and 5.11c). The lack of correlation between $\tau_{cyc}/s_{u,DSS}$ and *OCR* is expected due to the strong positive correlation between $s_{u,DSS}$ with *OCR*. However, the scatter plots suggests that there is somewhat stronger linear correlation between $\tau_{cyc}/s_{u,DSS}$ versus *PI*, and a moderate nonlinear correlation between $\tau_{cyc}/s_{u,DSS}$ versus *N* when the specimens are considered in aggregate, with R^2 of 0.16 and 0.46, respectively (Figs. 5.11b and 5.11d).

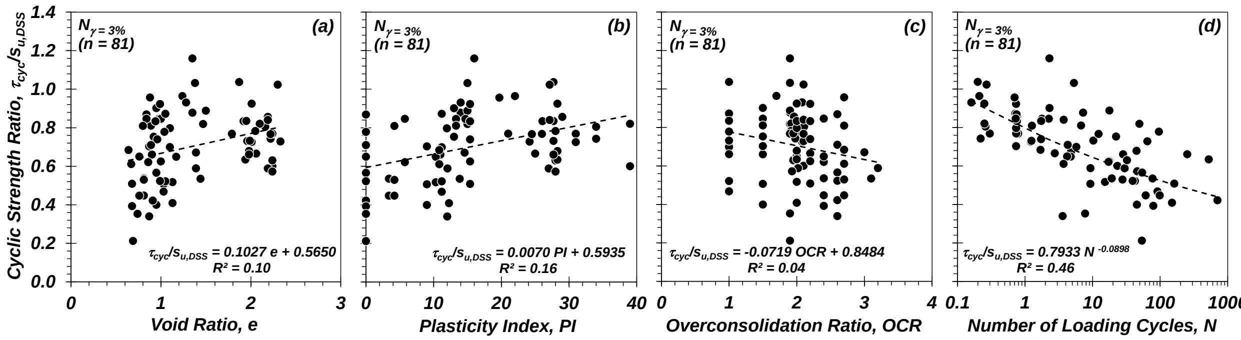

Figure 5.11 Variation of $\tau_{cyc}/s_{u,DSS}$ with respect to: (a) void ratio, *e*, (b) plasticity index, *PI*, (c) overconsolidation ratio, *OCR*, and (d) number of loading cycles, *N*.

The degree of statistical rigor of each predictor to estimate $\tau_{cyc}/s_{u,DSS}$ using the *training dataset* was investigated using linear regression against four different univariate linear regression models. Table B5 presents the statistical analysis of the univariate relationships plotted in Figure 5.11, which indicate that the contribution of all of predictors to $\tau_{cyc}/s_{u,DSS}$ is statically significant, except *OCR* (characterized with a *p*-value = 0.061). Preliminary investigations suggested that the void ratio should not be considered as an independent predictor in the proposed model for estimation of $\tau_{cyc}/s_{u,DSS}$ since: (1) *e* and *PI* are correlated as shown in Figure 5.2, and (2) *e* is generally correlated with monotonic undrained shear strength, and as such the effect of *e* on the $\tau_{cyc}/s_{u,DSS}$ is captured indirectly. Similar to the statistical regressions developed for *CRR*, the preliminary linear interpretations of correlation suggest further investigation using nonlinear combinations of selected predictor variables, as described below.

5.4.2 Validation of the Functional Form for Estimating Cyclic Strength Ratio for the Shear Strain Failure Criterion of 3% ($N_{\gamma=3\%}$)

The statistical analysis performed in Section 5.4.1 indicated that *PI* and *N* are independent parameters may serve to best explain the cyclic strength ratio for silty soils in the *training dataset*. Nonlinear combinations of all predictor variables (i.e., *e*, *PI*, *OCR*, and *N*) were statistically examined. Numerous trial statistical models indicated that the contribution of *OCR* in variation of $\tau_{cyc}/s_{u,DSS}$ is insignificant (i.e., *p*-value > 0.05) and it appears that *OCR* affects τ_{cyc} and $s_{u,DSS}$ in a way similar to that implied by SHANSEP representations, the effect of which would be cancelled by dividing τ_{cyc} with $s_{u,DSS}$ to employ as a response variable in the model. Therefore, *OCR* was disregarded as a predictor variable for $\tau_{cyc}/s_{u,DSS}$. Given that a power-law is able to represent the $\tau_{cyc}/s_{u,DSS}$ - *N* data (see for example Fig. 3.2 in Section 3.3.2), the functional form of the regression model implemented for *CRR* in Section 5.3 was modified for use in the estimation of $\tau_{cyc}/s_{u,DSS}$. Trial regression models to estimate $\tau_{cyc}/s_{u,DSS}$ were evaluated using the *training dataset* and the performance of selected candidates assessed against the *testing dataset* for $N_{\gamma=3\%}$.

Equation (5.7) was initially modified to estimate $\tau_{cyc}/s_{u,DSS}$ by excluding *OCR* and setting the exponent on *N* equal to a constant (the effect of which is explored below):

$$\frac{{\tau_{cyc}}^*}{s_{u,DSS}} = s_0 * (PI+1)^{s_1} * N^{s_2} \quad (5.8)$$

where $\tau_{cyc}^*/s_{u,DSS}$ is the predicted $\tau_{cyc}/s_{u,DSS}$, s_0 is the fitted coefficient and s_1 and s_2 are fitted exponents. The statistical significance of the independent predictor variables in Eq. (5.8) was evaluated using the NLS function in software package *R*. The results indicate that *PI* does not serve as statistically-significant predictor for $\tau_{cyc}/s_{u,DSS}$ in *training dataset*, characterized by *p*-value > 0.05. This finding is not consistent with the results of laboratory tests conducted as part of this study, which identified the clear role of *PI* on $\tau_{cyc}/s_{u,DSS}$ (Section 3.3.2; Eq. 3.1). Equation (5.8) was thus modified with various linear and nonlinear combinations of *PI* and *N* in bivariate linear and nonlinear models with varying levels of complexity. The significance of predictors and performance of each model were evaluated in a stepwise manner by monitoring selected statistical metrics (i.e., *p*-value, R^2, $\bar{\lambda}$, and COV_λ). The functional form identified as the most robust model to estimate $\tau_{cyc}/s_{u,DSS}$ is given by:

$$\frac{{\tau_{cyc}}^*}{s_{u,DSS}} = s_0 \left(\frac{N}{PI+1}\right)^{s_1} \quad (5.9)$$

where s_0 and s_1 are fitted coefficient and exponent, respectively. The statistical rigor of Eq. (5.9) and predictor variables was assessed using the NLS function and found to be statistically-significant considering the resulting *t*-statistics and *p*-values (Table 5.6).

Table 5.6 Summary of performance for Eq. (5.9) for the estimation of $\tau_{cyc}/s_{u,DSS}$ corresponding to $N_{\gamma=3\%}$ with respect to the *training dataset.*

Proposed Model	Model Parameter	Parameter Estimate	SE	*t*-statistic	*p*-value
$\frac{{\tau_{cyc}}^*}{s_{u,DSS}} = s_0 \left(\frac{N}{PI+1}\right)^{s_1}$	s_0	0.6595	0.0161	41.1	2.00e-16
	s_1	-0.0691	0.0082	-8.4	1.53e-13

Figure 5.12a compares the laboratory-based and estimated $\tau_{cyc}/s_{u,DSS}$ for specimens within the *training dataset* corresponding to $N_{\gamma=3\%}$; the goodness-of-fit metrics indicate that the model reasonably captures the observed $\tau_{cyc}/s_{u,DSS}$ in an unbiased manner *on average* ($\bar{\lambda}$ = 1.00), with less than desirable strength (R^2 = 0.49), but relatively low uncertainty ($COV_{\bar{\lambda}}$ = 0.20). Figure 5.12b examines the accuracy of the provisionally-trained coefficient and exponent using the independent *testing dataset* with *n* = 25, illustrating that on average, $\tau_{cyc}/s_{u,DSS}$ is over-predicted with similar strength and lower variability relative to the *training dataset*, characterized with R^2 = 0.51, $\bar{\lambda}$ = 0.98, and COV_λ = 0.16. The somewhat arbitrary definition of undrained shear strength, $s_{u,DSS}$ (e.g., at γ = 15%; Section 3.2) for specimens which exhibit strain hardening behavior during monotonic shearing may explain the reduced accuracy. Nonetheless, examination of the performance of Eq.

(5.9) and provisionally-fitted parameters using the independent *testing dataset* (Fig. 5.12b) indicates that the model can maintain its strength to predict $\tau_{cyc}/s_{u,DSS}$ for $N_{\gamma=3\%}$. Therefore, the fitted parameters were finalized for use in predicting $\tau_{cyc}/s_{u,DSS}$ through regression of the *combined dataset* for different magnitudes of N_{γ}.

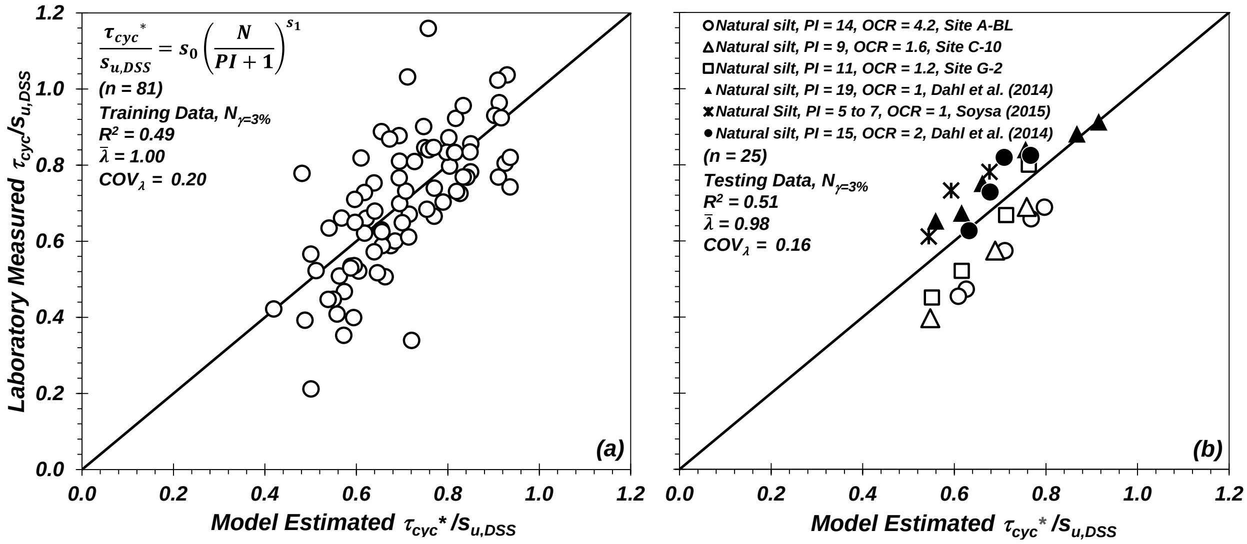

Figure 5.12 Comparison of the experimental and predicted $\tau_{cyc}/s_{u,DSS}$ with Eq. (5.9) for the: (a) *training dataset*, and (b) *testing dataset* for $N_{\gamma=3\%}$.

5.4.3 Finalized Models for Cycle- and Strain-Dependent Estimates of $\tau_{cyc}/s_{u,DSS}$

Equation (5.9) was retrained using the *combined dataset* for different magnitudes of N_{γ}. Table 5.7 presents the results of the statistical analysis conducted using the *combined dataset* including the fitted parameters and corresponding standard errors, *t*-statistics, and *p*-values. All of the fitted predictor variables exhibited statistical significance the range in N_{γ} considered.

As an alternative approach for estimating the cyclic strength ratio and as means for comparison among different approaches, $\tau_{cyc}/s_{u,DSS}$, was computed using Eq. (5.7) in conjunction with the corresponding representative monotonic, normalized undrained shear strength, $s_{u,DSS}/\sigma'_{v0}$, for a given specimen:

$$CRR = \frac{\tau_{cyc}}{\sigma'_{v0}} = \frac{\tau_{cyc}}{s_u}\cdot\frac{s_{u,DSS}}{\sigma'_{v0}} \rightarrow \frac{\tau_{cyc}}{s_{u,DSS}} = \frac{\frac{\tau_{cyc}}{\sigma'_{v0}}}{\frac{s_{u,DSS}}{\sigma'_{v0}}} = \frac{CRR}{\frac{s_{u,DSS}}{\sigma'_{v0}}} \quad (5.10)$$

where *CRR* is estimated using Eq. (5.7) and subsequently corrected to a loading frequency, *f* = 1 Hz by increasing the *CRR* by 9% for comparison to the cyclic strength ratio.

Table 5.7 Summary of the finalized fitted model parameters and associated statistical metrics for Eq. (5.9) for different cyclic shear strain failure criterion.

Cyclic Shear Strain Failure Criterion	Model Parameter	Parametr Estimate	SE	*t*-statistic	*p*-value
$N_{\gamma=1\%}$	s_0	0.5127	0.0262	19.54	2.00e-16
	s_1	-0.0805	0.0113	-7.15	1.90e-10
$N_{\gamma=2\%}$	s_0	0.6122	0.0160	38.18	2.00e-16
	s_1	-0.0638	0.0072	-8.86	3.37e-14
$N_{\gamma=3\%}$	s_0	0.6549	0.0132	49.79	2.00e-16
	s_1	-0.0702	0.0071	-9.85	2.00e-16
$N_{\gamma=3.75\%}$	s_0	0.6899	0.0142	48.55	2.00e-16
	s_1	-0.0758	0.0084	-9.02	8.60e-15
$N_{\gamma=5\%}$	s_0	0.7086	0.0130	54.20	2.00e-16
	s_1	-0.0880	0.0096	-9.33	8.79e-15
$N_{\gamma=8\%}$	s_0	0.7319	0.0161	45.50	2.00e-16
	s_1	-0.1046	0.0131	-7.96	7.09e-11
$N_{\gamma=10\%}$	s_0	0.7492	0.0178	42.22	2.00e-16
	s_1	-0.1003	0.0155	-6.47	5.70e-08

Figure 5.13 presents the performance of the finalized model parameters for Eq. (5.9) to estimate $\tau_{cyc}/s_{u,DSS}$ for the specimens within the *combined dataset* for cyclic shear strain failure criteria of 1 to 10% shear strain. In addition, *CRR*-based estimates of the $\tau_{cyc}/s_{u,DSS}$ using CRR^* estimates and Eq. (5.10) are included in Fig. 5.13. Equation (5.9) performs most poorly for $\tau_{cyc}/s_{u,DSS}$-$N_{\gamma=1\%}$ ($R^2 = 0.43, \overline{\lambda} = 1.00$, $COV_\lambda = 0.20$), similar to Eq. (5.10) as a result of the low magnitude of N for this strain amplitude (i.e., $N \leq 1$) for specimens within the *combined dataset*. However, the performance of Eq. (5.9) improves somewhat in terms of the selected goodness-of-fit metrics as the cyclic shear strain failure amplitude exceeds 1%, with R^2 ranging from 0.48 to 0.54, $\overline{\lambda} = 1.00$, and COV_λ ranging from 0.17 to 0.19. It is of interest to evaluate the prediction strength of Eqs. (5.7) and (5.10) for estimation of $\tau_{cyc}/s_{u,DSS}$, which may be useful when accurate (i.e., laboratory-based) or estimated monotonic undrained shear strengths are available. In general and for $\gamma \geq 2\%$, Eq. (5.10) seeded with the results of Eq. (5.7) performs better in the estimation of $\tau_{cyc}/s_{u,DSS}$, interpreted in terms of greater accuracy, bias nearer to unity, and similar COV_λ compared to those estimated using Eq. (5.9). Depending on the availability of the laboratory test data, either Eqs. (5.7) and (5.10) or Eq. (5.9) may be used for estimating $\tau_{cyc}/s_{u,DSS}$.

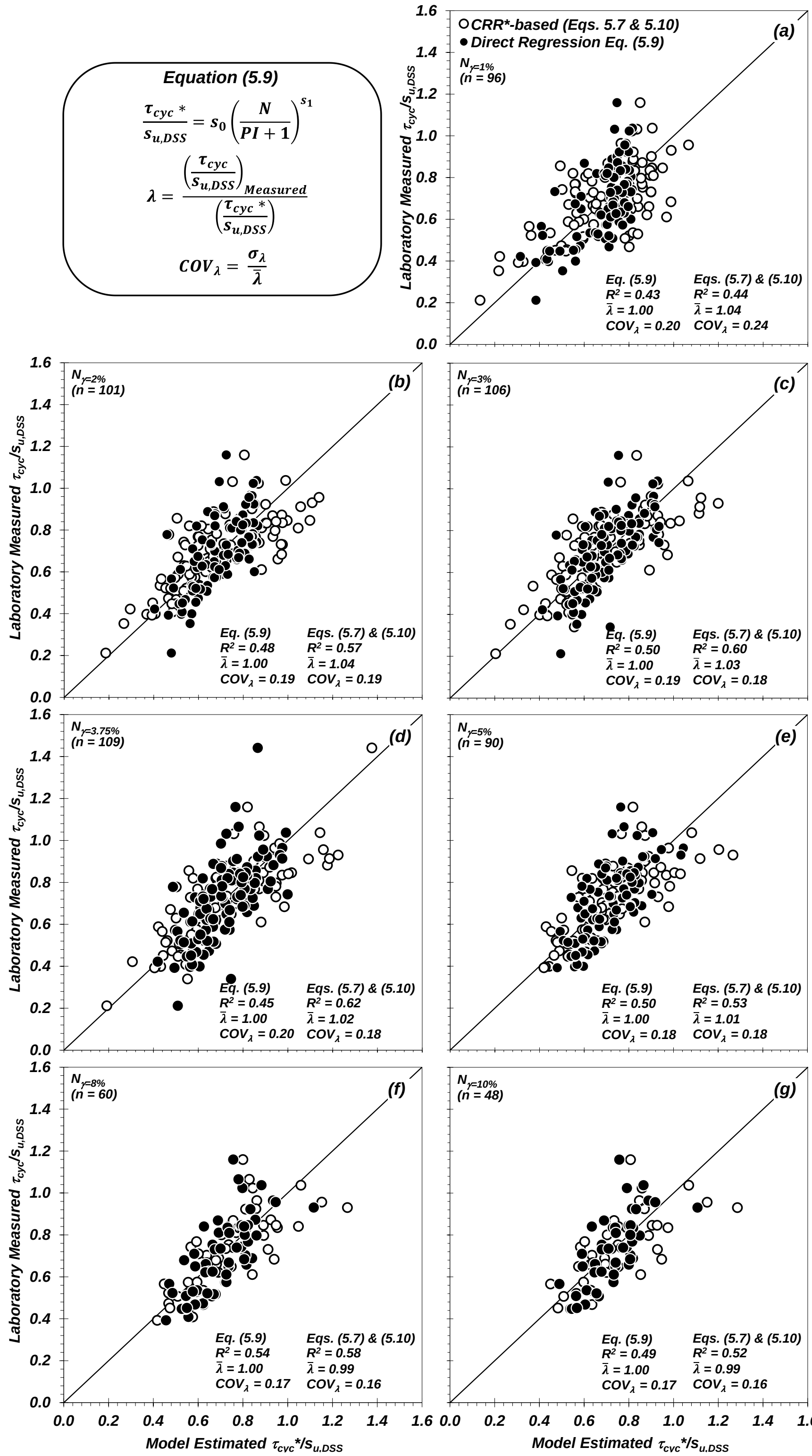

Figure 5.13 Comparison of the experimental $\tau_{cyc}/s_{u,DSS}$ and that directly estimated using Eq. (5.9), along with the product of *CRR* using Eq. (5.7) and $s_{u,DSS}/\sigma'_{vc}$, using the *combined dataset* for the cyclic shear strain failure criteria of: (a) 1%, (b) 2%, (c) 3%, (d) 3.75%, (e) 5%, (f) 8%, and (g) 10%.

Figure 5.14a presents the variation of strain-dependent $\tau_{cyc}/s_{u,DSS}$ estimated using Eq. (5.9) and the final fitted model parameters with different magnitudes of cyclic shear strain failure criteria for N = 30 and 100 and for PI of 0, 10, and 30. The estimated $\tau_{cyc}/s_{u,DSS}$ increases and decreases with increasing magnitude of N_{γ} and N, respectively, as may be expected given typical cyclic responses of soils. For example, for PI = 30, the estimated $\tau_{cyc}/s_{u,DSS}$ corresponding to $N_{\gamma=3\%}$ decreases from 0.66 to 0.60 as N increases from 30 to 100, respectively. For N = 30, the estimate of $\tau_{cyc}/s_{u,DSS}$ for $N_{\gamma=3\%}$ and $N_{\gamma=8\%}$ increases from 0.66 to 0.73. Figure 5.14b presents the $\tau_{cyc}/s_{u,DSS}$-N curves estimated using the finalized parameters for Eq. (5.9) corresponding to $N_{\gamma=3\%}$ with respect to PI. For a given N, Eq. (5.9) suggests that $\tau_{cyc}/s_{u,DSS}$ increases with increases in PI, consistent with the results of laboratory tests conducted in this study (Section 3.3.2) and others (e.g., Dahl et al. 2018; Wijewickreme et al. 2019). For example, for N = 30, an increase in PI from 0 to 10 and 10 to 30 results in increases of in $\tau_{cyc}/s_{u,DSS}$ of 18% and 8%, respectively. The increase in $\tau_{cyc}/s_{u,DSS}$ as soil composition transitions from nonplastic to low-plasticity indicates the beneficial effect of PI on cyclic resistance, which moderates as PI increases further.

Similar unexpected model estimates of $\tau_{cyc}/s_{u,DSS}$ for large cyclic shear strains and nonplastic specimens are produced with Eq. (5.9) as that for Eq. (5.7), as a result of data scarcity. The reader is referred to Section 5.3.4 for a comprehensive discussion of the impact of data limitations on model estimates.

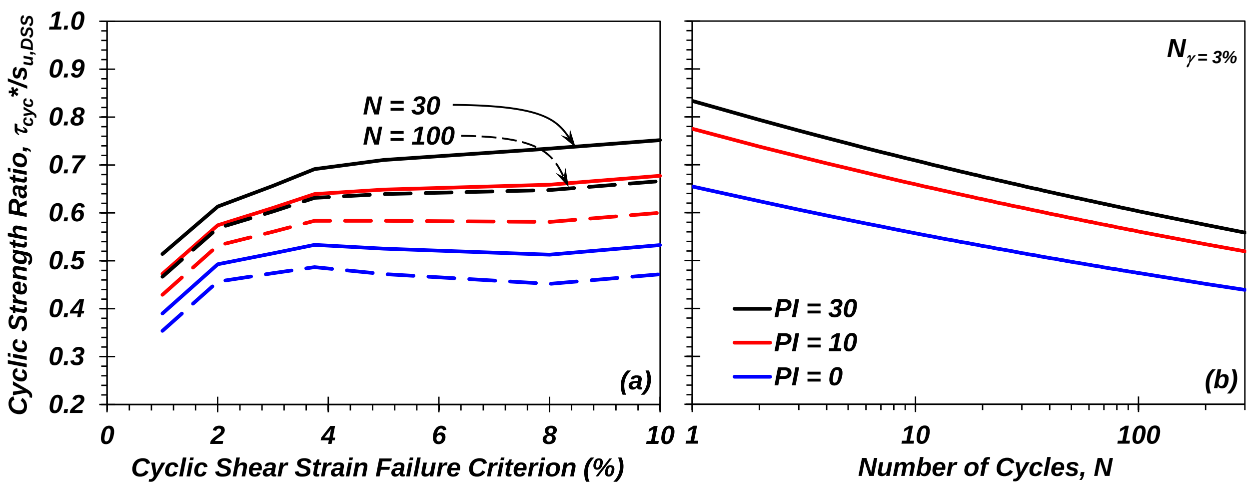

Figure 5.14 Variation of cyclic strength ratio, $\tau_{cyc/su,DSS}$, estimated using Eq. (5.9) for N = 10 and 30 with: (a) different magnitudes of cyclic shear strain failure criteria, and (b) number of loading cycles, N for $N_{\gamma=3\%}$.

Table 5.8 presents regression equations for the shear strain-dependent model parameters for Eq. (5.9) for use in estimating $\tau_{cyc}/s_{u,DSS}$ for the selected shear strain amplitudes of 1% to 10%. These equations were developed through ordinary least squares regression on the fitted model parameters tabulated in Table 5.7. Goodness-of-fit metrics for each equation are tabulated in Table 5.8 for inspection by the user, and achieve satisfactory fits across the range in shear strain investigated. Note that Eq. (5.9) was trained on data representing a cyclic loading frequency of 1 Hz.

Table 5.8 Shear strain-dependent model parameters for use with Eq. (5.9).

$\frac{\boldsymbol{\tau_{cyc}}^{*}}{\boldsymbol{s_{u,DSS}}} = \boldsymbol{s_0}\left(\frac{\boldsymbol{N}}{\boldsymbol{PI+1}}\right)^{\boldsymbol{s_1}}$	**Coefficient of Determination, R^2**	**Mean Bias, $\bar{\lambda}$**	**Coefficient of Variation in Bias, COV_λ**	**Sum of Squared Errors, SSE**
$s_0 = \frac{1.0121 \cdot \gamma^{0.9217}}{0.7176 + 1.2691 \cdot \gamma^{0.9217}}$	0.999	1.000	0.007	0.00013
$s_1 = \frac{-16.9073 - 0.0004 \cdot \gamma^{-11.700}}{145.68 + 63.619 \cdot \gamma^{\left(\frac{3.9047}{\gamma} - 0.9612\right)}}$	0.984	1.000	0.028	0.00005

6 APPLICATION OF THE SIMPLIFIED METHOD TO CYCLIC FAILURE OF SILTS FOR SUBDUCTION ZONE EARTHQUAKES

Northern California, Oregon, Washington, and British Columbia are situated in an active seismic region with crustal, intraslab, and interface earthquakes contributing to the total seismic hazard in this region. Although previous magnitude scaling factors for use in assessing the cyclic failure potential using the Simplified Method have considered available ground motion records from some or all of the types of earthquakes which are likely to strike the Pacific Northwest, the availability of the recently-curated NGA Subduction Database (Bozorgnia and Stewart 2020) allows for a critical re-examination in view of those earthquakes which heretofore have been most prevalent in the region: intraslab and interface earthquakes consistent with the Cascadia Subduction Zone (CSZ). Characteristics of such representative earthquakes could be critical where distant urban population centers may be strongly affected by fault rupture, particularly in the event of a partial or full rupture of the relatively shallow CSZ interface situated near the coast of the Pacific Northwest. In an effort to provide regionally-consistent evaluations of the seismic hazard due to cyclic failure of transitional, nonplastic and plastic silts, the authors present formulations for the number of equivalent loading cycles and magnitude scaling factors for use with the Simplified Method for cyclic failure potential and measurements or estimates of the cyclic resistance of these soils. The statistical models for cyclic resistance developed in Section 5 may be used in the absence of cyclic laboratory test data, and corresponding examples for the evaluation of cyclic failure are presented with accompanying discussion, along with some limitations of the Simplified Method for application to megathrust earthquakes.

6.1 MAGNITUDE SCALING FACTORS AND EQUIVALENT NUMBER OF LOADING CYCLES FOR SUBDUCTION ZONE EARTHQUAKES

6.1.1 Ground Motion Selection (NGA Subduction Database)

Development of the equivalent number of uniform stress cycles, N_{eq}, and magnitude scaling factors, MSFs, for application to the Simplified Method for cyclic failure potential for subduction zone earthquakes is made possible through ground motions drawn from the NGA Subduction database (Bozorgnia and Stewart 2020). Several aspects of ground motion characteristics were considered in selection of available subduction zone earthquake records for the development of MSFs and N_{eq}, including:

- **Hypocentral distance between the source and site**: rupture of the Cascadia Subduction Zone (CSZ) interface in a megathrust event may occur for a portion or the entirety of the interface. The distance between the southernmost reaches of the CSZ interface and urban population centers, such as Vancouver, British Columbia, can approach 1,000 km. Accordingly, no ground motion within the NGA Subduction database was excluded on the basis of hypocentral distance;
- **Peak ground accelerations (*PGA*s)**: The amplitudes of ground motions tend to correlate with the equivalent number of uniform loading cycles, owing in part to the source-to-site distance and corresponding attenuation of shaking intensity. Excluding low intensity ground motions could serve to artificially reduce the median N_{eq} as a result of enforcing an arbitrary *PGA* threshold. Accordingly, no ground motion within the NGA Subduction database was excluded on the basis of *PGA*;
- **Site Class**: Considering the potential ranges in thickness of deposits and typical shear wave velocities of relatively young non-plastic and plastic silt distributed throughout the Pacific Northwest, ground motions recorded at sites with Site Class C, D, and E are considered as the sites of greatest interest. Accordingly, ground motion records corresponding to Site Class A and B were excluded in the development suitable MSFs and N_{eq}; and,
- **Recording Stations**: Recording stations that strongly deviate from free-field conditions (e.g., stations fixed to bridge components, above-ground building floors, etc.) were considered inappropriate for use in assessing magnitude scaling factors and N_{eq} due to the potential for unnatural amplification of the ground motion record. Accordingly, such ground motion records were excluded from the dataset used herein.

These considerations allowed 429 two-component horizontal ground motions (858 acceleration time histories in total) to be admitted into the dataset used to develop the relationships for N_{eq} and MSF reported herein (i.e., the vertical component of the acceleration time history was neglected). Ground motions were corrected for baseline drift and filtered to minimize spurious frequencies (e.g., noise) by Bozorgnia and Stewart (2020). Table C1 summarizes the ground motions selected indicating the moment hypocentral distance, magnitude, M_w, *PGA*, and V_{S30}, among other features. Figure 6.1 presents the distribution of earthquake hypocentral distance, moment magnitude, *PGA*, and site classes for the ground motions considered in the present analysis. Approximately 36% of the motions correspond to $M_w > 8.0$, the magnitudes most consistent with CSZ ruptures. Approximately 17% of the ground motions were characterized with $PGA > 0.25g$. The percentage of recordings that represent Site Class C (360 m/s < $V_{s,30}$ < 760 m/s), Site Class D (180 m/s < $V_{s,30}$ < 360 m/s), and Site Class E ($V_{s,30}$ < 180 m/s) are 58.4%, 39.3%, and 2.3%, respectively. The reader is referred to Bozorgnia and Stewart (2020) for further information and discussions on the characteristics of these ground motions.

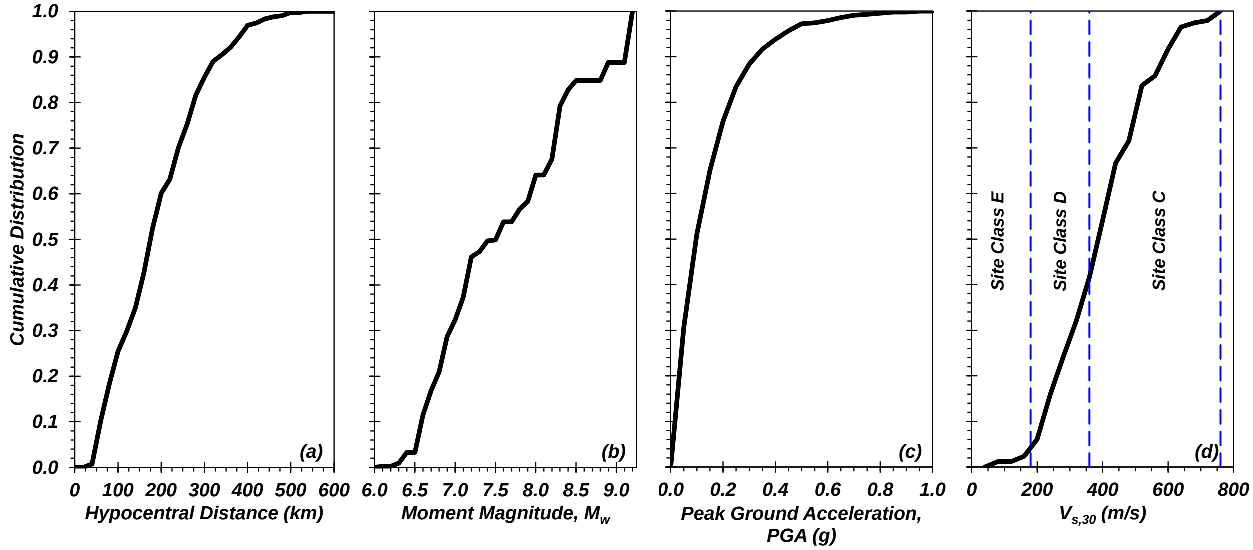

Figure 6.1 Cumulative distribution of characteristics of earthquake ground motion records considered in the development of magnitude scaling factors and the number of equivalent loading cycles: (a) hypocentral distance, (b) moment magnitude, (c) peak ground acceleration, and (d) site class.

6.1.2 Calculation of the Equivalent Number of Cycles

Although the loading of interest corresponds to that acting below the ground surface, the surface ground motion records used in this study are considered appropriate for calculation of N_{eq}, based on an assessment by Lee and Chan (1972) that indicated little variation in N_{eq} with depth for a given site and recording (Verma et al. 2019). The equivalent number of stress cycles from each acceleration time history was computed following the methodology presented by Boulanger and Idriss (2015) using a *Matlab*[2] script. The approach allowed the determination of the cyclic stress ratio, *CSR*, equal to the cyclic shear stress divided by the vertical effective stress, τ_{cyc}/σ'_{v0}, from the acceleration record using the Simplified Method of cycle counting outlined by Seed et al. (1975). In this process, it is assumed that the ratio of acceleration and the absolute maximum acceleration or *PGA* is equal to the ratio of *CSR* and the absolute maximum *CSR*, CSR_{max} (Green and Terri 2005; Verma et al. 2019) For each positive and negative half cycle, *i,* of the *CSR* time history, the *matlab* code counts and stores the absolute maximum CSR_i. Then the maximum CSR_i for the entire time history is stored in the variable CSR_{max}, which is then used to calculate a reference cyclic stress ratio, CSR_{ref}. Seed and Idriss (1971) and Seed et al. (1975) observed that the peak intensity of a ground motion was less suitable than a fraction of the peak intensity for describing the response of soil to dynamic loading over the duration of the motion, and selected 65% percent of the maximum intensity to represent the ground motion; thus, the reference intensity in terms of cyclic shear stresses was suggested as $CSR_{ref} = 0.65CSR_{max}$. This reference *CSR* was

[2] The MathWorks Inc. (2022). MATLAB version: 9.13.0 (R2022b), Natick, Massachusetts: The MathWorks Inc. https://www.mathworks.com.

implemented herein to determine N_{eq} from the *CSR* time history. Furthermore, any absolute CSR_i less than $0.1CSR_{max}$ was sequentially removed from the analysis, and the number of the half-cycles counted, *i*, updated following Boulanger and Idriss (2004) and Verma et al. (2019).

Thereafter, N_{eq} is calculated for each exponent *b* using (Boulanger and Idriss 2004):

$$N_{eq} = \frac{1}{2}\sum_{i=1}^{i}[(\frac{CSR_i}{CSR_{ref}})^{\frac{1}{b}}] \tag{6.1}$$

where *b* is the exponent in the *CRR-N* curve, described in Sections 3 and 5.

Figure 6.2 presents the variation of N_{eq} with M_w for $6 < Mw \leq 9.12$ derived for various selected magnitudes of *b* to illustrate how the shape of the *CRR-N* curve influences N_{eq}. The scatter in N_{eq} for a given M_w is due to the variability in the characteristics of the earthquake source, hypocentral distance, depth, duration, frequency content, and properties of the soil profile (e.g., Boulanger and Idriss 2015). Despite the scatter in N_{eq}, an exponential function for $N_{eq}(M_w)$ fitted to the data using ordinary least squares (OLS) regression and shown in Figure 6.2 illustrates how *b* dictates N_{eq} and allows quantification of the mean N_{eq} as function of earthquake magnitude. For a given M_w, N_{eq} decreases with increases in *b* (Kishida and Tsai 2014). Additionally, the sensitivity of N_{eq} to M_w, quantified using the coefficient on M_w in Figure 6.2, increases with increases in *b*.

Figure 6.2 also identifies the three subduction zone events within the NGA Subduction Database that are associated with the Pacific Northwest and the CSZ, for reference. These earthquakes include the 57 to 60 km deep, normal-faulting intraslab 1949 M_w 6.7 Olympia earthquake (Ichinose et al. 2006; Bozorgnia and Stewart 2020), the 53 to 60 km deep, normal-faulting intraslab 2001 M_w 6.8 Nisqually earthquake (Ichinose et al. 2006; Bozorgnia and Stewart 2020), and the 21 to 29 km deep, strike-slip intraslab 2010 M_w 6.5 Ferndale earthquake (Pitarka et al. 2013; Bozorgnia and Stewart 2020). Note that ground motion records for the1965 Seattle-Tacoma earthquake was not included the NGA Subduction Database. The variability in N_{eq} does not appear significantly different among the three CSZ earthquakes for low *b*; however, as *b* increases, N_{eq} appears to span a smaller range for the strike-slip 2010 Ferndale event relative to the 1949 Olympia and 2001 Nisqually events. This may have resulted from a variety of factors, ranging from fault mechanism, stronger basin effects for the Washington State earthquakes, and depth of rupture, among other factors, the contribution of which is beyond the scope of the current study.

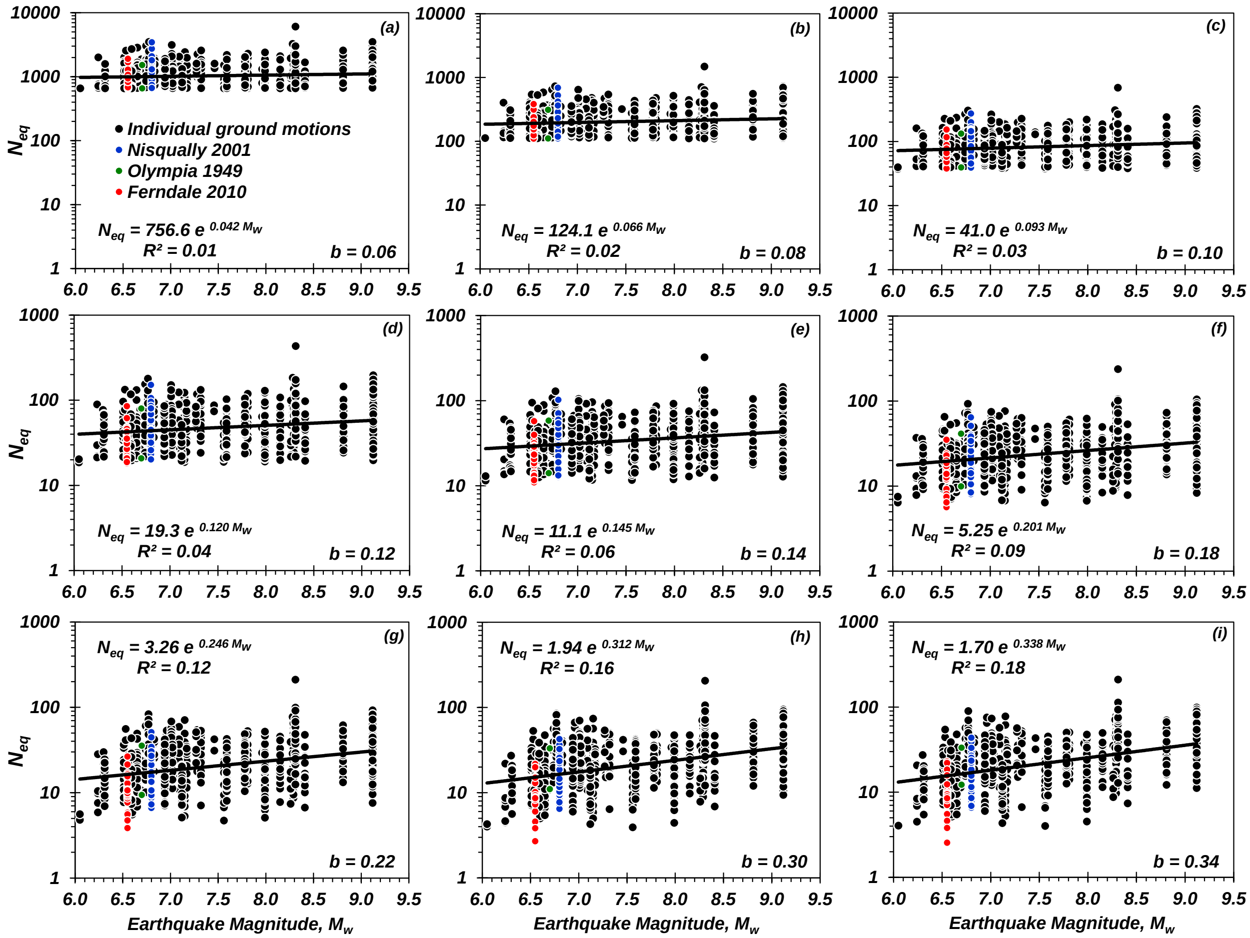

Figure 6.2 Variation of equivalent number of stress cycles, N_{eq} with subduction zone earthquake magnitude, M_w ($6 < M_w \leq 9.12$) derived for varying exponent b: (a) $b = 0.06$ (b) $b = 0.08$ (c) $b = 0.10$ (d) $b = 0.12$ (e) $b = 0.14$ (f) $b = 0.18$ (g) $b = 0.22$ (h) $b = 0.30$, and (i) $b = 0.34$.

Figure 6.3 compares the geometric mean number of equivalent stress cycles with earthquake magnitude for various specific and general soil types reported in the literature which are characterized with different exponents b. The geometric mean of N_{eq} was preferred over the arithmetic average as N_{eq} scales approximately logarithmically with M_w, and places less weight on extreme N_{eq}. In addition, the geometric mean of N_{eq} was observed to be similar to the median N_{eq} for the ground motion records considered. For the same magnitude of b, an increase in M_w results in an increase in N_{eq}. The results derived in this study, which are appropriate for application to Cascadia Subduction Zone earthquakes, are *generally similar* to the results of previous studies (e.g., Boulanger and Idriss 2004; Verma et al. 2019) for similar exponents b. The slight differences noted in Figure 6.3 are attributed to the differences in the number of ground motions evaluated and their characteristics (Green and Terri 2005; Kishida and Tsai 2014). For example, Verma et al. (2019) randomly selected 410 ground motions from 31 earthquakes with $5 < M_w \leq 9.1$ and source-to-site distance < 200 km, whereas Boulanger and Idriss (2004) used a set of 124 ground motions from 13 different earthquakes with $7 < M_w \leq 8.0$. Relevant for the silt soils at the focus of this study, the current analysis returned N_{eq} = 46 cycles for M_w = 7.5 and b = 0.12 (Figure 6.3), compared to 44 cycles for b = 0.118 reported by Verma et al. (2019; Serpentine River Sediments). Note that as the plasticity index increases, b reduces, and N_{eq} increases at an increasing rate.

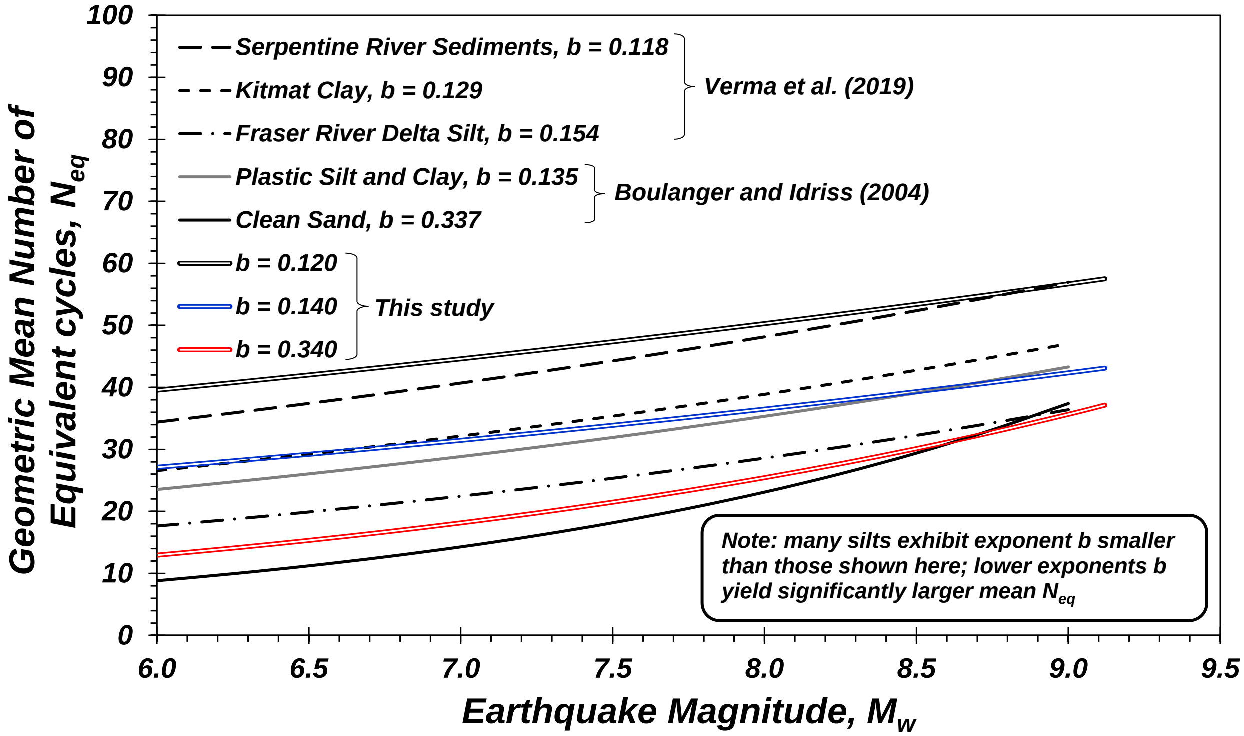

Figure 6.3 Relationship of the geometric mean number of equivalent stress cycles with earthquake magnitude for different soil types and comparison of N_{eq} to the results of previous studies.

Figure 6.4 presents the relationship between the N_{eq} with exponent b for each of the 858 ground motions with $6.0 < M_w \leq 9.12$ for four "bins" of ground motions differentiated by the range in moment magnitude. It may be observed that ground motions of given M_w can be characterized by a wide range in N_{eq}, often exceeding 100 for the silt soils of Western Oregon and Southwest Washington (i.e., b ranging from 0.05 to 0.15). The variability in N_{eq} for a given bin of M_w is evident in Figure 6.4, with an average geometric coefficient of variation in N_{eq}, $COV_g(N_{eq})$, defined as the geometric standard deviation in N_{eq} divided by the geometric mean, ranging from 0.35 to 0.71 for the four bins considered (see Fig. 6.5a for additional information). In general, the *normalized* uncertainty in N_{eq} is smaller for small b, as expressed using $COV_g(N_{eq})$, and increases with increases in b (Fig. 6.5a). For perspective, consider an intraslab event with M_w = 6.5: the geometric mean and geometric standard deviation of N_{eq} for b = 0.15 (typical non-plastic silt) is 27 cycles and 1.68 (which corresponds to 15 cycles), respectively. For a plastic silt deposit (e.g., PI = 30) with $b \approx 0.05$ (Eq. 5.3), the geometric mean and geometric standard deviation in N_{eq} is approximately 3,950 and 1.42 (equal to 1,425 cycles), respectively. Thus, the use of b-dependent average N_{eq} should be accompanied by the understanding and incorporation of the variability associated with earthquake-induced ground motions.

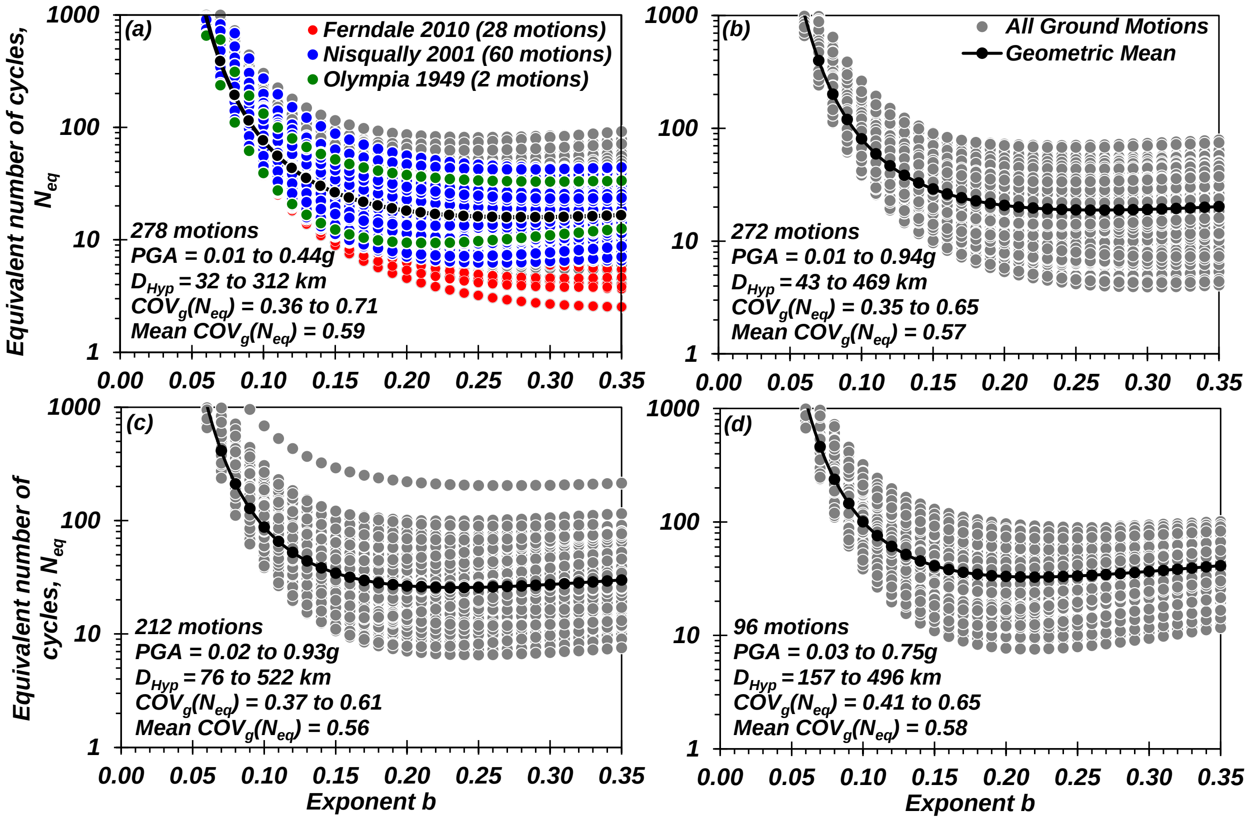

Figure 6.4 Relationship of the equivalent number of stress cycles with exponent *b* for individual ground motions and their mean response considering 858 ground motion records with $6 < M_w \leq 9.12$: (a) $M_w = 6.0$ to 7.0, (b) $M_w = 7.0$ to 8.0, (c) $M_w = 8.0$ to 9.0, and (d) $M_w = 9.12$.

The variation of the geometric mean N_{eq} and $COV_g(N_{eq})$ with exponent b and earthquake magnitude is shown in Fig. 6.5a. For any given M_w, N_{eq} rapidly increases with decreases in exponent b. For exponent $b = 0.14$, the geometric mean N_{eq} ranges from 30 to 45 corresponding to M_w of 6.0 to 9.12 respectively. The average M_w is reported for each bin for reference and indicates that M_w is not uniformly distributed within a given bin. Further, just one event comprises the entirety of the $M_w > 9$ bin (i.e., 2011 Tohoku). Megathrust earthquakes of $M_w > 9.12$ may therefore exhibit greater N_{eq} than those determined herein. Table 6.1 summarizes the geometric mean N_{eq} determined for each binned earthquake magnitude and b, which should be used to help guide termination criteria for site-specific cyclic laboratory test programs.

For ease of use in practice, the geometric mean of N_{eq} can be expressed the form:

$$\overline{N_{eq}} = exp(n_0 b^{n_1} + n_2 b^{n_3} + n_4 b^{n_5}) \tag{6.2}$$

for a given M_w bin, where n_0, n_1, …, n_5 are fitted coefficients and exponents, respectively. The goodness-of-fit is presented graphically in Figure 6.5a and reported in Table 6.2, which summarizes the fitted model parameters for use with Eq. (6.2).

Figure 6.5b compares the variation of the geometric mean N_{eq} with exponent b for M_w ~ 7.5 (represented by the bin $7.0 < M_w \leq 8$) to the results of previous studies (Kishida and Tsai 2014; Boulanger and Idriss 2015; Verma et al. 2019), indicating N_{eq} which are somewhat higher than previously-reported N_{eq}, depending on the magnitude of b. For M_w = 7.5 and b = 0.14, the mean N_{eq} is 33, compared to N_{eq} = 30 reported by Idriss and Boulanger (2008). For dense clean sands, b is suggested equal to about 0.34 (Boulanger and Idriss 2015); use of the screened NGA Subduction database resulted in N_{eq} = 20 in contrast to the previously-recommended 15 for use with the Simplified Method for liquefaction triggering (Seed and Idriss 1971; Youd et al. 2001; Boulanger and Idriss 2015). This may be due to the greater number of crustal ground motion records considered (see Table 3 in Seed et al. 1975). The larger number of equivalent loading cycles stems largely from the longer duration and larger hypocentral distances associated with subduction zone earthquakes considered in this study.

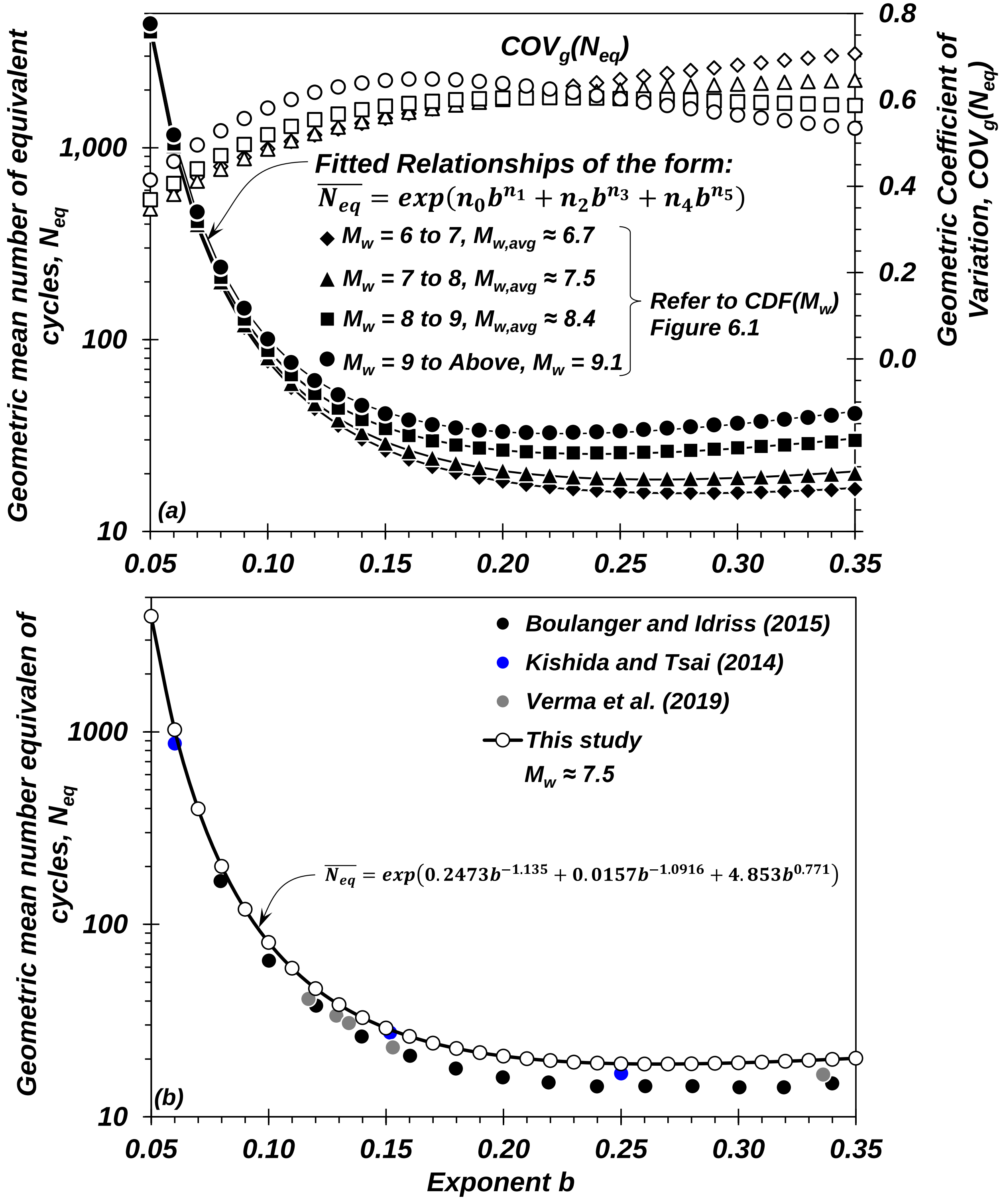

Figure 6.5 Effect of exponent *b* on the equivalent number of stress cycles for different earthquake magnitudes: (a) average N_{eq} for all 858 ground motion records corresponding M_w = 6.0 to 9.12, and (b) variation of average N_{eq} with exponent *b* for M_w ~ 7.5 and their comparison with previous studies.

Table 6.1 Equivalent number of cycles for each binned magnitude and exponent *b* shown in Figure 6.5a.

Exponent b	Geometric Mean Equivalent Number of Loading Cycles, N_{eq}			
	$6 \leq M_w \leq 7$	$7 \leq M_w \leq 8$	$8 \leq M_w \leq 9$	$9 \leq M_w \leq 9.12$
0.05	3945	3984	4020	4422
0.06	1011	1026	1048	1164
0.07	390	399	413	463
0.08	195	201	211	238
0.09	115	120	128	146
0.10	77	81	88	101
0.11	56	59	66	76
0.12	44	46	52	61
0.13	36	38	44	52
0.14	30	33	38	45
0.15	27	29	34	41
0.16	24	26	32	38
0.17	22	24	30	36
0.18	20	23	28	35
0.19	19	22	27	34
0.20	18	21	27	33
0.21	18	20	26	33
0.22	17	20	26	33
0.23	17	19	26	33
0.24	16	19	26	33
0.25	16	19	26	33
0.26	16	19	26	34
0.27	16	19	26	34
0.28	16	19	27	35
0.29	16	19	27	36
0.30	16	19	27	37
0.31	16	19	28	37
0.32	16	19	28	38
0.33	16	20	29	39
0.34	16	20	29	40
0.35	17	20	30	41

Table 6.2 Summary of fitted parameters for computing exponent b-dependent $\overline{N_{eq}}$ using Eq. (6.2) for each binned magnitude corresponding to Table 6.1.

$\overline{N_{eq}} = exp(n_0 b^{n_1} + n_2 b^{n_3} + n_4 b^{n_5})$	n_0	n_1	n_2	n_3	n_4	n_5	$\overline{\lambda}$	COV_λ
$6.0 \le M_w < 7.0$	0.2674	-1.1125	0.0158	-1.094	4.542	0.822	0.999	0.008
$7.0 \le M_w < 8.0$	0.2473	-1.1350	0.0157	-1.0916	4.853	0.771	1.000	0.010
$8.0 \le M_w < 9.0$	0.2124	-1.1792	0.0154	-1.083	5.574	0.712	1.000	0.013
$9.0 \le M_w < 9.1$	0.2093	-1.1843	0.0154	-1.0856	6.2446	0.7073	1.000	0.015

6.1.3 Magnitude Scaling Factors (MSFs) for Use with Subduction Zone Earthquakes

The Simplified Methods for liquefaction and cyclic softening potential traditionally use magnitude scaling factors to relate cyclic loading (or resistance) to earthquake magnitudes other than the standard M_w 7.5 earthquake. Magnitude scaling factors for Subduction zone earthquakes, which can exhibit significantly longer duration than crustal earthquakes, are influenced by the number of equivalent loading cycles inferred from a given ground motion, as described above. The results in Figures 6.4 and 6.5 can be distilled into subduction zone-appropriate, b-dependent *MSF*s by scaling the variation of the geometric mean N_{eq} for $M_w = 7.5$ (Fig. 6.5b) by the corresponding N_{eq} for $6 < M_w \le 9.12$ using (Idriss and Boulanger 2008; Boulanger and Idriss 2015):

$$MSF = \left[\frac{N_{eq,M_w=7.5}}{N_{eq,M_w}}\right]^b \tag{6.3}$$

where N_{eq,M_w} equals the number of equivalent cycles for a given M_w. Figures 6.6a and 6.6b presents the individual *MSFs* calculated using Eq. (6.3) for each ground motion record and M_w for $b = 0.09$, 0.15, and 0.34 to illustrate the sensitivity of the *MSF* to b. Figures 6.6a and 6.6b also indicate linear and exponential magnitude-dependent trend functions for the *MSF*s, respectively, representing the average *MSF* constrained to produce $MSF_{M_w=7.5} = 1.0$ to maintain consistency with previous Simplified Method procedures (e.g., Youd et al. 2001; Idriss and Boulanger 2008; Boulanger and Idriss 2014). These fitted trend functions representing the average *MSF* are given by:

$$MSF = p * M_w + q \tag{6.4}$$

$$MSF = r * exp^{s*M_w} \tag{6.5}$$

respectively. Figures 6.6c and 6.6d compare the variation in average *MSF* with M_w for the linear and exponential trends for silt-appropriate exponents $b = 0.09$ and 0.15, respectively, which indicate little difference in the resulting average *MSF* between the two possible trend functions. Accordingly, the use of the simpler linear approximation to the average *MSF* is recommended for use in forward analyses of cyclic failure potential.

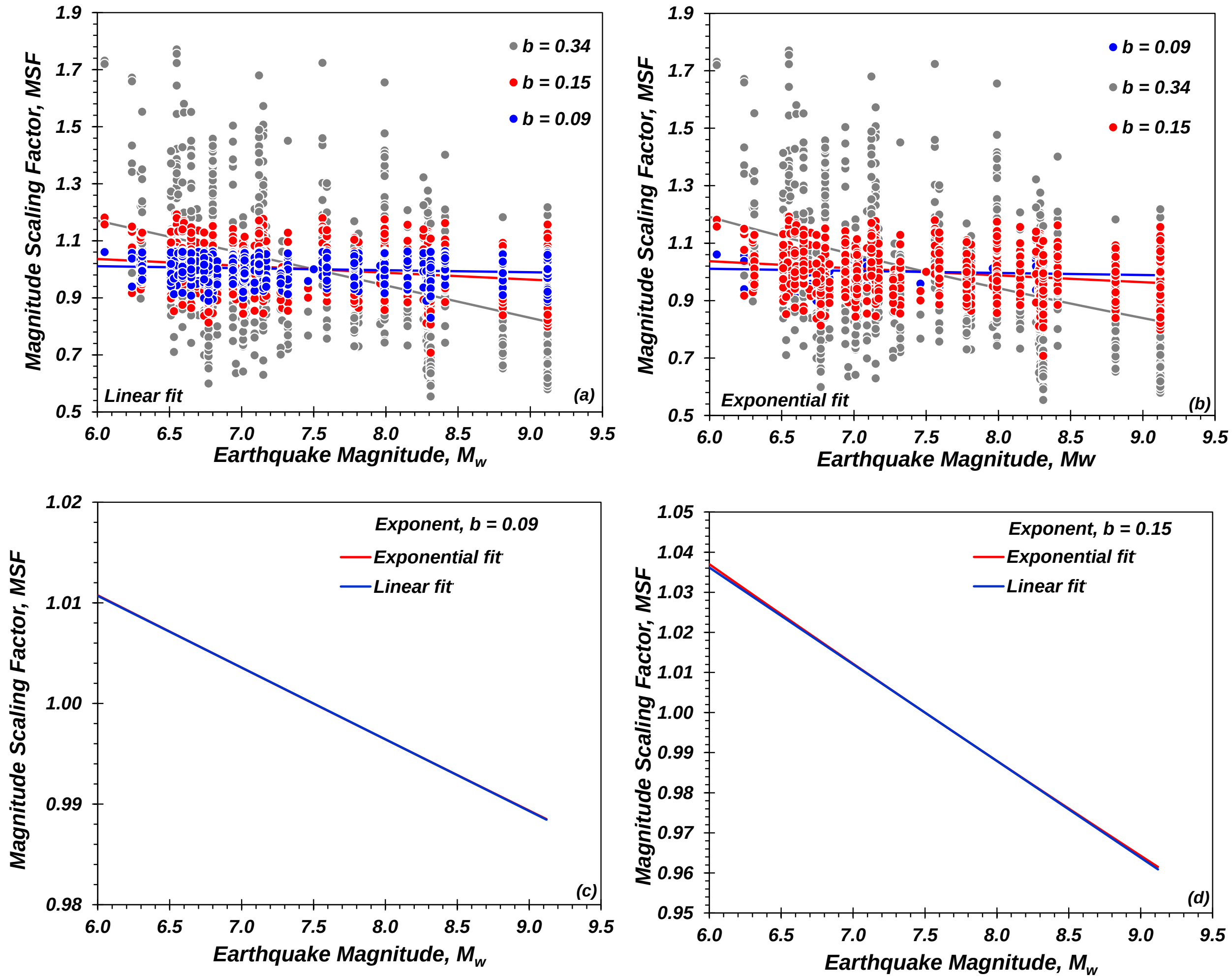

Figure 6.6 Variation of magnitude scaling factors derived for different exponents *b* with M_w = 6.0 to 9.12 (858 ground motions): (a) individual ground motions with a fitted linear trend, (b) individual ground motions with a fitted exponential trend, and comparison of *MSF* with M_w considering fitted linear and exponential trends for: (c) *b* = 0.09, and (d) *b* = 0.15.

Application of Eq. (6.4) to compute the *MSF* requires the specification of the exponent *b*-dependent linear coefficient, *p*, and intercept, *q*, for seamless use in forward analyses of cyclic failure potential. Figure 6.7a presents the variation of coefficient *p* and intercept *q* with exponent *b* for use with Eq. (6.4) derived following the analysis of *MSF*s for each ground motion record and *b* (shown in Fig. 6.6a for selected *b*). Following the evaluation of several trial functions, a second order polynomial function captured the observed relationships between *p* and *q*, and *b*, to result in:

$$p = -0.698b^2 - 0.13b + 0.0096 \tag{6.6}$$

$$q = 5.238b^2 + 0.973b + 0.928 \tag{6.7}$$

which upon substitution into Eq. (6.4) provides a convenient expression for *MSF*s in the range of $6 < M_w \leq 9.12$:

$$MSF = (-0.698b^2 - 0.13b + 0.0096) \cdot M_w + (5.238b^2 + 0.973b + 0.928) \tag{6.8}$$

Figure 6.7b presents examples of the magnitude-dependent *MSF* for a range in possible b. As implied by the preceding discussion, silt soils with high plasticity that exhibit small magnitudes of b are not sensitive to the magnitude of earthquake as shown by a near-constant $MSF \approx 1.0$. However, as the plasticity index decreases and b increases (see Section 5.2), the sensitivity of the cyclic resistance of silt to earthquake magnitude increases as indicated by the negative, non-zero slope of *MSF* with M_w. Equation (6.8) can be used to determine the adjustment to a standardized cyclic resistance of any soil that can be described by the power law-type *CRR-N* curve for use in a Simplified Method formulation, but is particularly appropriate for the silts in the Pacific Northwest, as it captures the equivalent number of cycles implied by the ground motions within the NGA Subduction database.

Figure 6.8 presents a comparison of the *MSF* computed using Eq. (6.8) for $b = 0.34$ (dense sand) and 0.135 (silty soils) to those reported by Boulanger and Idriss (2015) for M_w ranging from 6.0 to 9.12. Very little difference may be noted in the *MSF* relationships for silty soils; however, as exponent b increases (representing clean sands of increasing, inferred relative density), the MSFs deviate noticeably. This comparison simply demonstrates that magnitude scaling is significantly driven by the ground motion records and associated characteristics (frequency content, duration, site class) considered in their development, as noted nearly five decades ago (e.g., Seed et al. 1975).

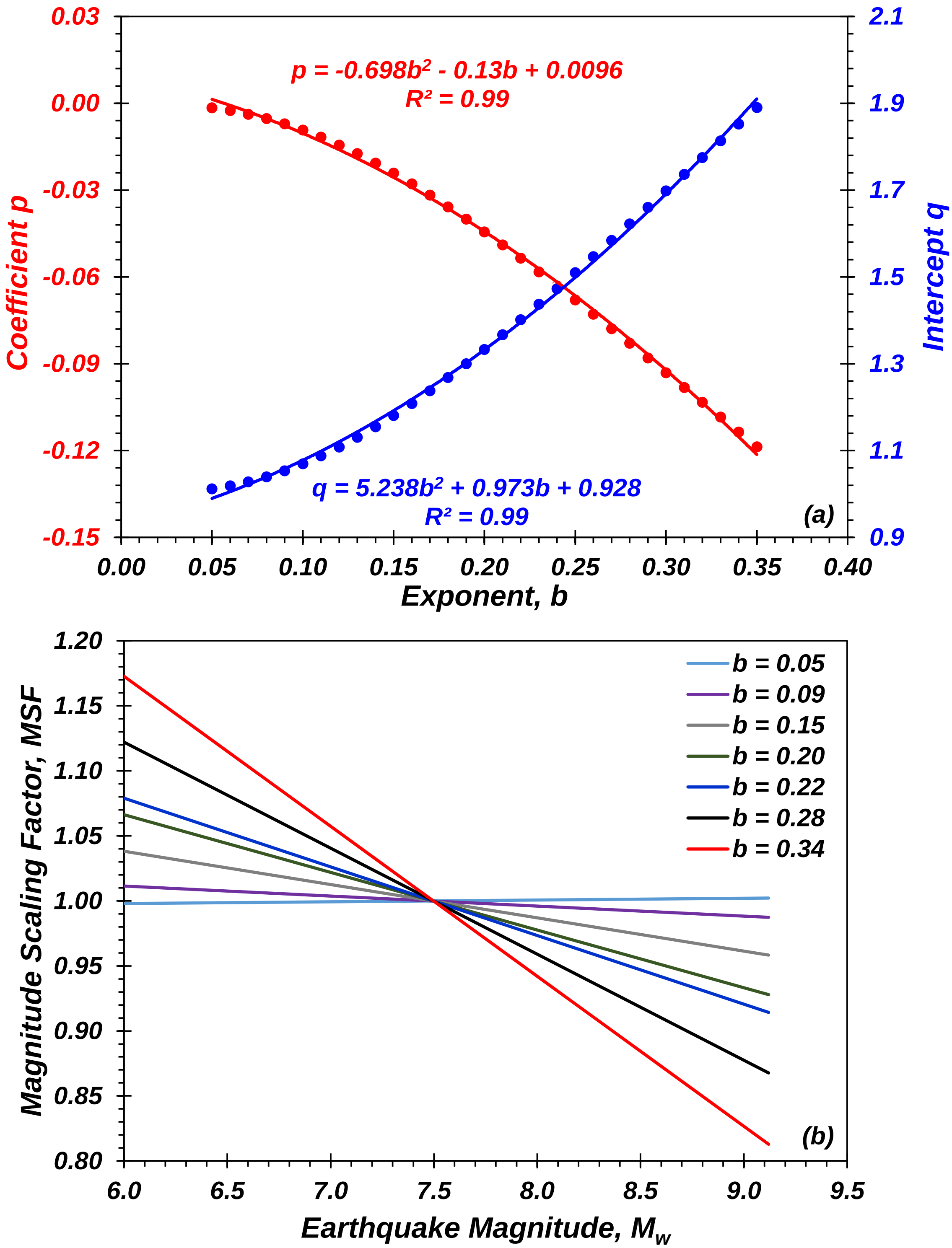

Figure 6.7 Proposed magnitude scaling factors for use with subduction zone earthquakes: (a) variation of coefficient *p* and intercept *q* with exponent *b* derived from the analysis of *b*-dependent N_{eq}, and (b) variation of *MSF* with moment magnitude M_w for soils exhibiting different exponents *b*.

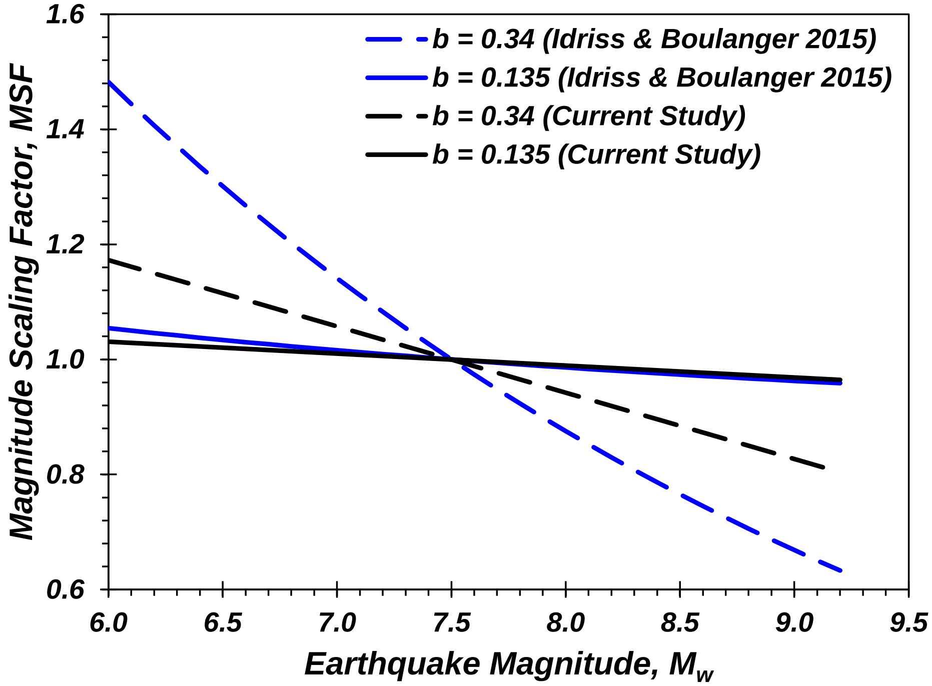

Figure 6.8 Comparison of magnitude scaling factors developed in this study (Eq. 6.8) using the NGA Subduction database to those reported by Boulanger and Idriss (2015) for selected exponents *b*.

6.2 IMPLEMENTATION OF STATISTICAL MODELS FOR CYCLIC RESISTANCE IN PRACTICE

6.2.1 Intended Use of the Statistical Models for Cyclic Resistance

The objective of this work is to propose improved estimates of cyclic resistance for evaluating the potential for cyclic failure potential for nonplastic and plastic silts during earthquakes. The work described in the previous sections support this goal to culminate in specific recommendations for evaluating the factor of safety against cyclic failure for a desired cyclic shear strain failure criterion (e.g., cyclic failure at 3% shear strain) and to provide an informed basis for increasing levels of geotechnical investigation over the course of a project where cyclic failure could occur. Specifically, the practitioner can use the recommendations summarized below for the purposes of design-level evaluations, planning of cyclic laboratory programs, and conducting site response and nonlinear deformation analyses.

Design-level evaluations: Given readily obtainable laboratory test information, including Atterberg limits data and oedemetric or preferred constant rate-of-strain compression tests to determine the preconsolidation stress and overconsolidation ratio, the statistical models presented in Section 5 can be used to:

- Estimate the exponent b and number of equivalent cycles, N_{eq}, for given earthquake magnitude, M_w. Exponent b can be estimated using Eq. (5.3) and Table 5.2. Refer to Table 6.2 and Eq. (6.2) to map b and M_w to N_{eq}. Note that the Table 6.2 and Eq. (6.2) returns the geometric average of N_{eq}, and is associated with significant variability as quantified by $COV_{N_{eq}}$;
- Estimate the variation of cyclic resistance ratio, *CRR*, of the soil with N_{eq} for a given M_w using Eq. (5.7) and Table 5.3. The *CRR* can then be used to compute the factor of safety against liquefaction triggering, FS_L, or cyclic softening, FS_{cs}, using the Simplified method (described below) for a given cyclic shear strain failure criterion. In so doing, it must be recognized that Eq. (5.7) was trained on data representing a cyclic loading frequency of 0.1 Hz. The *CRR* can therefore be increased by 9% for application to ground motions with a typical predominant frequency of 1 Hz (Idriss & Boulanger 2008);
- Estimate the variation of the cyclic strength ratio, τ/s_u, of the soil with N_{eq} for a given M_w using Eq. (5.9) and Table 5.8 and/or Eqs. (5.7) and (5.10) in conjunction with estimates or measured normalized undrained shear strengths; and,
- Based on the results of holistic design evaluations implementing the aforementioned statistical models, the practitioner can judge whether a site-specific cyclic laboratory program should be conducted in order to confirm the results of the previous design-level evaluations and the associated risk of cyclic failure and/or increase/decrease mitigation measures identified during the previous design phase.

Eq. (5.7) was developed using unidirectional cyclic DSS tests; Idriss & Boulanger (2008) recommend multiplying the unidirectional *CRR* by 0.96 to account for two-directional shearing, consistent with observations of the in-situ *CRR* determined for a plastic silt deposit based on multidirectional blast-induced ground motions (Stuedlein et al. 2023c). Other adjustments to the *CRR*, for example to account for static shear stress, may also be necessary.

Planning of cyclic laboratory programs: Design level evaluations may suggest that cyclic testing programs could shed additional light on the risk of cyclic failure. One of the key outcomes desired from a cyclic testing program is to understand the magnitude of post-cyclic settlement or post-cyclic undrained strength that is available, the magnitudes of which depend on either the threshold cyclic shear strain (or excess pore pressure) with which to terminate the cyclic test or the predefined number of cycles to which the specimen will be subjected. The latter option allows the post-cyclic performance of the specimen to be related to a specific magnitude of earthquake (and/or ground motion). Thus, upon initiating a cyclic testing program, the following could serve as a model work flow:

- *Revisit the seismic hazard*: review deterministic and/or probabilistic seismic hazard analyses to identify one or more design earthquake magnitudes (or specific ground motions) to "simulate" in the laboratory. Estimates of the cyclic shear stress (i.e., cyclic loading) from Simplified Methods or site response analyses are used to specify the range in cyclic stress ratios, *CSRs*, to be considered in the laboratory testing program;

- *Selection of the number of equivalent cycles*, N_{eq}: Estimate exponent b and N_{eq}, for given earthquake magnitude, M_w using Eq. (5.3) with Table 5.2, and Eq. (6.2) with Table 6.2, respectively. The cyclic shearing phase of the laboratory test can then be specified using the selected *CSR* and terminated upon achieving the target N_{eq}. The cyclic test termination criterion shall be communicated to laboratory personnel for each specimen; and,
- *Post-cyclic testing:* The post-cyclic phase will then commence immediately after the specimen reaches N_{eq} (following re-centering of the specimen) in order to observe the post-cyclic reconsolidation strain or post-cyclic monotonic undrained shear strength associated with the loading anticipated for the given earthquake scenario.

Alternatively, if the termination criterion for the cyclic shearing phase is set to a given cyclic shear strain failure criterion, the number of loading cycles N can be compared against the geometric average of N_{eq} (Eq. 6.2) and $COV_{N_{eq}}$ (see Figure 6.4) to assess the risk of cyclic failure for the design seismic hazard.

Site Response Analysis and Nonlinear Deformation Analysis: For cases where site-specific cyclic laboratory test programs are unable to be conducted, the results of this work can be used to inform and interpret site response and numerical deformation analyses:

- In some cases, it may be desirable to use the results of site response analyses to provide an alternate estimate of the factor of safety against cyclic failure. The maximum *CSR* within any given soil layer can be extracted from the site response analysis and factored by 65% (in accordance with the Simplified method) to provide the alternate estimate of loading. Then, the factored *CSR* can be used with the *CRR* computed with Eq. (5.7) and Table 5.3 (f = 0.1 Hz) and increased by 9% (for f = 1%) to compute FS_L or FS_{cs}. Other adjustments, for example to account for two-directional loading or static shear stresses, should be made to *CRR* as dictated by the specific project conditions.
- Dynamic, numerical, nonlinear deformation analyses require calibrated constitutive models to simulate the hysteretic response of soils. Constitutive models such as PM4SILT (Boulanger et al. 2022) can be calibrated against the estimates of *CRR* produced using Eq. (5.7).

In each of the suggested applications of the statistical models developed in this study, the limitations and uncertainties in model estimates described in Sections 5 and 6 should be directly considered in the evaluation and interpretation of analytical and laboratory results.

6.2.2 Calculation of the Cyclic Stress Ratio for Subduction Zone Earthquakes within the Simplified Method Framework

The basic framework of the Simplified Method originally proposed by Seed and Idriss (1971) consists of computing the factor of safety against cyclic failure, originally proposed for liquefaction triggering evaluation of coarse-grained soils, using:

$$FS = \frac{CRR}{CSR} \tag{6.9}$$

which requires an estimate of the cyclic resistance ratio (i.e., the resistance) and the cyclic stress ratio (i.e., the loading). The *CSR* may be computed using (Seed and Idriss 1971; Idriss and Boulanger 2008):

$$CSR = 0.65\frac{\tau_{peak}}{\sigma'_{vc}} = 0.65\frac{\sigma_{vc}}{\sigma'_{vc}}\frac{a_{max}}{g}r_d \tag{6.10}$$

where τ_{peak} = peak earthquake-induced shear stress acting on a horizontal plane, σ'_{vc} = the vertical effective (consolidation) stress, σ_{vc} = the vertical total (consolidation) stress, a_{max} = the maximum acceleration at the ground surface, g = the gravitational constant, and r_d = the depth-dependent shear stress reduction coefficient to account for the soil profile flexibility. The reference stress of 65% of τ_{peak} is aligned with the use of $CSR_{ref} = 0.65CSR_{max}$ selected for the determination of N_{eq} in Section 6.1.2.

One of the main sources of uncertainty in Eq. (6.10) in the Simplified Method for cyclic failure potential is the representativeness of the shear stress reduction factor, r_d (Youd et al. 2001). Several forms of this depth-dependent coefficient on *CSR* have been proposed in the literature (e.g., Seed and Idriss 1971, Idriss 1999, and Cetin et al. 2004) and it is generally based on equivalent linear, total stress site response analyses of simple profiles that consider a range in site periods (e.g., shear wave velocity profiles). The shear stress reduction coefficient proposed by Idriss (1999) and described in a more widely-distributed form by Idriss and Boulanger (2010), is given by:

$$r_d(z) = \exp\left(\alpha(z) + \beta(z)\cdot M_w\right) \tag{6.11}$$

where $\alpha(z)$ and $\beta(z)$ are given by:

$$\alpha(z) = -1.012 - 1.126 sin\left(\frac{z}{11.73} + 5.133\right) \tag{6.12}$$

$$\beta(z) = 0.106 - 1.118 sin\left(\frac{z}{11.28} + 5.142\right) \tag{6.13}$$

respectively, and z = depth in meters, and the elements encapsulated within the parenthesis are in radians. Idriss and Boulanger (2008) caution that while Eqs. (6.11) – (6.13) are applicable for depths smaller than or equal to 34 m, they should generally be restricted to depths of 20 m or less owing to the increased uncertainty in r_d with increased depth. It is worthwhile to note that Eq. (6.11) was calibrated to represent the 67% percentile of r_d back-calculated following the evaluation of several hundred site response analyses performed for M_w = 7.5, and represents a slightly conservative estimate of the governing cyclic loading with depth for this magnitude of earthquake (Idriss and Boulanger 2010).

It is critical to recognize that $M_w = 9^+$ earthquake motions were scarce prior to the year 2000, and as a result, there is relatively little experience with the liquefaction case history evaluation of r_d for subduction zone earthquakes. Accordingly, sole reliance on Eq. (6.11) for application to the assessment of cyclic soil failure (e.g., liquefaction, cyclic softening) associated with megathrust, interface Cascadia Subduction Zone earthquake scenarios is not recommended at this time. The results of site response analyses by Idriss (1999) and summarized in Idriss and Boulanger (2010) indicate that as the frequency of the input motion decreases (or period increases), the depth-varying shear stress reduction coefficient increases, implying that there is a frequency-dependent decrease in profile flexibility. This is a critical concern for application of Eq. (6.11) to interface subduction zone earthquakes, which often generate long period motions. Thus, it may be expected that the reduction in the cyclic loading due to soil profile flexibility may not be as large as that computed using Eq. (6.11) for such a scenario. Underestimation of r_d leads to an underestimation of the cyclic demand on the soil, and therefore the overestimation of any factor of safety against cyclic failure.

It is therefore essential that assessments of the factor of safety against cyclic failure consider the results of carefully conducted (total stress) site response analyses carried out by experienced professionals. Towards this end, the subsurface must be sufficiently characterized with site response analyses in mind; this requires that the shear wave velocity profile be measured over the entire depth of the overburden, and preferably that of the underlying basement rock. Soil layer thicknesses, and their variation across a site should ascertained with a high degree of confidence, as should the soil unit weights. Critical soil properties necessary for calibration of shear modulus reduction and damping curves must be sufficiently defined. Furthermore, a large number of input ground motions representative of the intended earthquake scenarios should be used in order to suitably quantify the uncertainty in the soil flexibility and corresponding shear stress reduction coefficient, which may be back-calculated for each input motion using (Idriss and Boulanger 2010):

$$r_d(z) = \frac{\tau_{peak}(z)}{\sigma_{vc}(z) \cdot a_{max}\,(z = 0)} \tag{6.14}$$

where $\tau_{peak}(z)$ = depth-dependent peak earthquake-induced shear stress acting on a horizontal plane within a layer of interest in the site response analyses, and σ_{vc} = the vertical total (consolidation) stress at depth z. Alternatively, and perhaps more directly useful, the results of site response analyses can be used to directly assess the variation of $\tau_{peak}(z)$ and CSR using Eq. (6.9), and its variation in regard to the input motions selected. In this manner, the sensitivity of cyclic failure potential to the uncertainty in loading may be directly quantified on a site-specific basis.

6.2.3 Direct Implementation of the Simplified Method Framework

Site-specific cyclic laboratory tests may be used to directly quantify the cyclic resistance ratio, *CRR*, for use in computing the factor of safety against cyclic softening using Eq. (6.9). Herein, the cyclic failure criterion of shear strain, γ = 3%, is assumed. The application of the direct, site-specific method requires that exponent *b* for the soil under consideration be determined directly from the laboratory cyclic test data, and then Eq. (6.2) and Table 6.2 is referenced to map *b* and design earthquake magnitude, M_w to N_{eq}. The corresponding *CRR* is then selected from the laboratory-derived *CRR-N* curve, adjusted to 1 Hz loading frequency and for multidirectional shaking, and Eq. (6.9) is used to determine the *FS*.

Illustrative Example and Discussion. *Goal:* compute the *FS* against cyclic failure, FS_{cf}, for a Cascadia Subduction Zone earthquake with M_w = 9.0 for a low plasticity silt at Site B at a depth of 5 m under σ'_{vc} = 50 kPa. Site response analyses indicate that τ_{peak} will range from 12 to 18 kPa at this depth for the ground motions evaluated. Consider the series of constant-volume, cyclic direct simple shear tests from test series B-13 (Table 3.2) on soil with *OCR* = 1.9 and *PI* = 14 to 16 and tested under σ'_{vc} = 50 kPa shown in Figure 6.9. Table 6.1 indicates that for *b* = 0.11 and M_w = 9.0, N_{eq} = 76, which corresponds to a *CRR* = 0.28 for γ = 3%. This *CRR* can be increased by 9% to account for a loading frequency of 1 Hz, and reduced by 4% to account for multidirectional shaking, to yield *CRR* = 0.293. Equation (6.10) returns effective *CSRs* (i.e., CSR_{max} factored by 65%) ranging from 0.156 to 0.234, with corresponding FS_{cf} ranging from 1.25 to 1.88.

The FS_{cf} of 1.25 may be judged as potentially lower than acceptable depending on the performance requirements for a project: FS_{cf} of 1.25 implies γ < 3%, but positive excess pore pressures are likely to be generated. Dadashiserej et al. (2022a) presents post-cyclic volumetric strain data for test series B-13, which suggest that volumetric strains ranging from about 0.33 to 1.0% may be expected for γ < 3%; this may not be desired for certain structures and/or lead to the development of dragloads on deep foundations. Similarly, Jana and Stuedlein (2021) describe cyclic and post-cyclic tests on plastic silts (average *PI* = 28; Site D in the current work), which indicate that for γ = 1 and 3%, maximum r_u ranges from 0 to 10% and 10 to 40% respectively, corresponding to post-cyclic volumetric strains of 0 to 0.4%, respectively. Jana and Stuedlein (2022) present the variation of the post-cyclic, monotonic undrained shear strength with excess pore pressure generated during the cyclic phase; for maximum r_u ranging from 0 to 40%, post-cyclic strength ranges from 100 to 80% of the initial undrained shear strength. Thus, the results of factors of safety against cyclic softening should be interpreted through the lens of the resulting consequences in terms of settlements and stability.

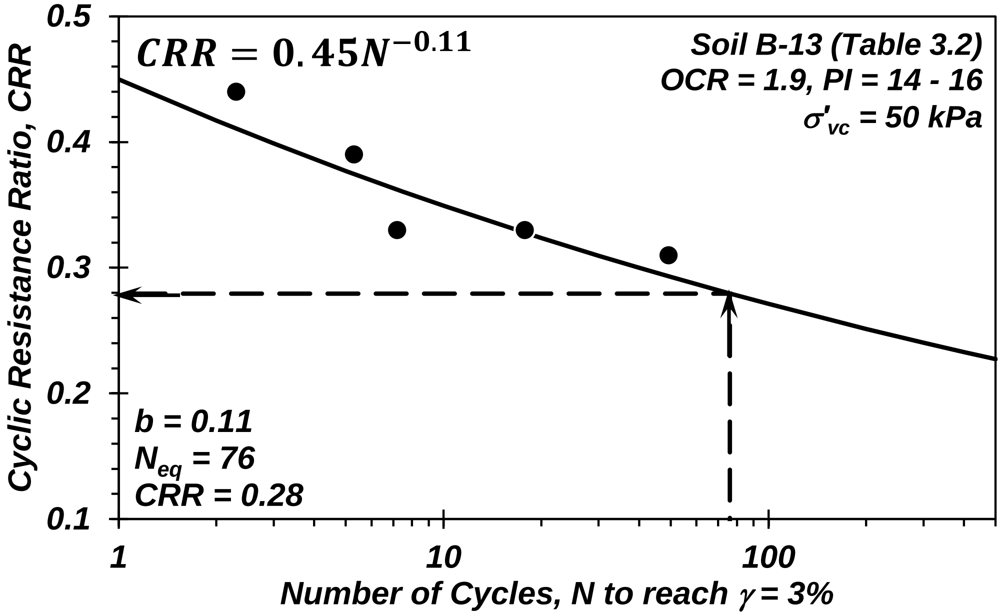

Figure 6.9 Cyclic resistance ratio (*f* = 0.1 Hz) versus number of cycles for Site B-13.

6.2.4 Direct Implementation of Statistical Models for Cyclic Resistance Ratio in the Simplified Method Framework

In the absence of site-specific cyclic laboratory tests, the statistical models developed herein may be used to estimate the likely cyclic resistance ratio, *CRR*, for use in computing the factor of safety against cyclic failure. The regression model for *CRR* (i.e., Eq. 5.7) has been developed using the cyclic shear failure criteria ranging from 1% $\leq \gamma \leq$ 10% as described in Section 5.3 and loading frequency of 0.1 Hz. In this approach, exponent *b* is estimated using Eq. (5.3), and N_{eq} computed using Eq. (6.2) and Table 6.2. Then Eq. (5.7) may be then used to determine the *CRR* corresponding to N_{eq}, adjusted for *f* = 1 Hz and two-directional shaking, and the *FS* against cyclic failure is computed using Eq. (6.9) for the selected cyclic shear strain failure criterion.

Illustrative Example and Discussion. *Goal:* compute the FS_{cf} for a Cascadia Subduction Zone earthquake with M_w = 9.0 for a low plasticity silt similar to the example described in Section 6.2.3 (i.e., *OCR* = 1.9, *PI* = 15). Site response analyses indicate that τ_{peak} will range from 12 to 18 kPa at the depth of 5.0 m and σ'_{vc} = 50 kPa. For illustrative purposes, Eq. (5.3) and Eq. (5.7) are selected to estimate exponent *b* and the cyclic resistance ratio, respectively. Equation (5.3) returns *b* = 0.10 for *PI* = 15, which is associated with N_{eq} = 99 for M_w = 9.0 (Eq. 6.2). Equation (5.7) returns a *CRR* = 0.213 for N_{eq} = 101, *OCR* = 1.9, and *PI* = 15 for γ = 3% (Figure 6.10). This *CRR* is increased by 9% and reduced by 4% to account for a loading frequency of 1 Hz and two-directional shaking to yield *CRR* = 0.223. Finally, Equation (6.1) returns *CSRs* ranging from 0.156 to 0.234, with corresponding FS_{cf} ranging from 0.95 to 1.43 (compare to 1.25 to 1.88 in the previous example).

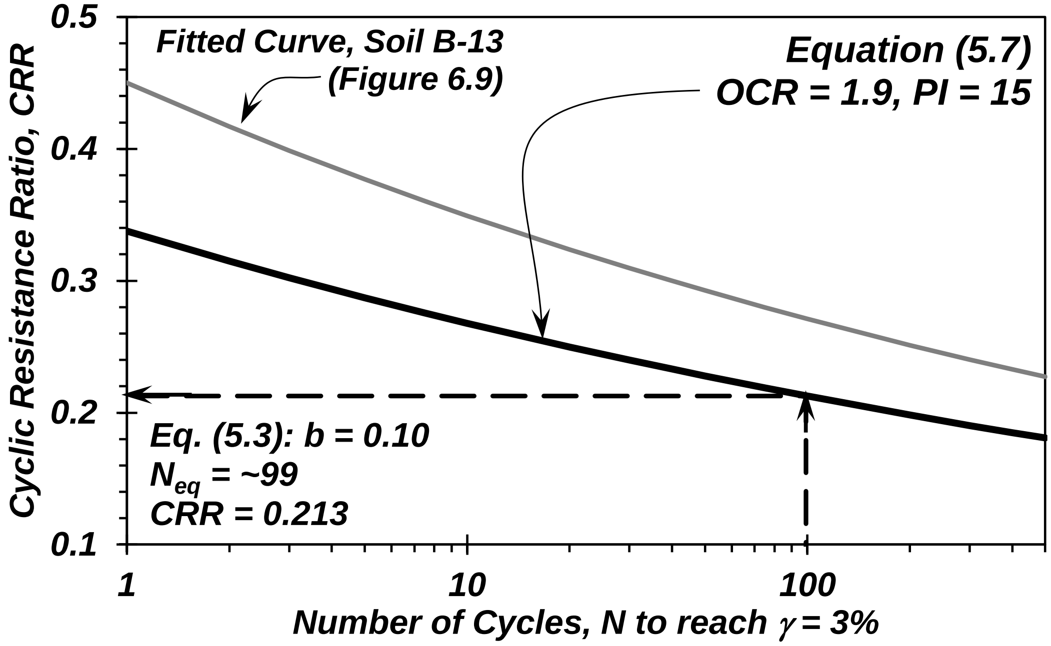

Figure 6.10 Cyclic resistance ratio versus number of cycles computed using Eq. (5.7) for *f* = 0.1 Hz.

Equation (5.3) yields a smaller *b* parameter (0.10 vs. 0.11) than that measured to result in a larger N_{eq} than that associated with laboratory test results from specimens derived from the site. Additionally, Figure 6.10 shows that Eq. (5.7) underestimates the actual cyclic resistance of the Site B soils. The magnitudes and range in FS_{cf} computed in this example and using the proposed statistical models are smaller to those computed using the results of site-specific laboratory cyclic testing. Thus, site-specific cyclic testing is preferred over model estimates where possible. Nonetheless, the statistical models can provide the practitioner with a means to make assessments prior to the development of a laboratory testing program, perhaps as part of 30% design level assessments, where such laboratory characterization data such as plasticity and stress history have been developed from baseline investigations. The results of site response analyses can be paired with the baseline investigation and the statistical models to inform decisions whether a round of selected site-specific laboratory cyclic testing would help inform seismic hazard evaluations and/or confirm that cyclic failure presents a distinct concern. Should a laboratory cyclic program be desirable, the statistical models can be used, in conjunction with site response analyses, to select preliminary *CSR*s and terminal N_{eq} prior to initiating the post-cyclic testing phase. Section 5.3.4 provides an important discussion on the limitations of the estimates of cyclic resistance for each of the available statistical models, and should be reviewed prior to the use of the models.

7 SUMMARY AND CONCLUSIONS

This report presented several advancements that should be of immediate and practical benefit to the geotechnical earthquake engineering profession, ranging from the provision of a database of laboratory cyclic data on intact silt specimens, statistical models enabling estimation of the equivalent number of cycles of loading for a given earthquake magnitude and corresponding cyclic resistance, new magnitude scaling factors leveraging the NGA Subduction Project, and guidance for the assessment of cyclic failure potential of transitional silt soils. The term cyclic failure is used throughout this report instead of liquefaction and cyclic softening, since different silt specimens in the database exhibited different cyclic failure mechanisms.

Previous recommendations for estimating the number of loading cycles for plastic silts and clays were based on a limited dataset and a single, representative exponent b for the cyclic resistance ratio-number of loading cycles (*CRR-N*) power law. The use of a single exponent represented experienced judgment based on the data available at the time. The database of cyclic loading test data assembled and evaluated in this report significantly expands the data available to re-assess trends in the curvature of the *CRR-N* relationship and culminates in a plasticity index-dependent function which can be used to estimate the exponent b in the power law describing cyclic resistance. This relationship may be used to estimate the cyclic resistance of silt soils as well as the number of equivalent loading cycles anticipated for a subduction zone earthquake.

Statistical models for the cyclic resistance ratio and cyclic strength ratio are also presented in this report. The SHANSEP-inspired functional form of these models have been trained and tested against independent datasets and finalized using a combined dataset to provide reasonable estimates of resistance based on the available data. These models can be used to provide provisional estimates of the *CRR-N* and cyclic strength ratio power laws for cyclic shear strain failure criteria ranging from 1 to 10%. An analysis of the data underlying the statistical models demonstrated that certain limitations in these statistical models exist, associated with unequal representation of data with certain stress history or material (e.g., plasticity index) characteristics for different shear strain amplitudes. Efforts to obtain laboratory-based estimates of the overconsolidation ratio (OCR) are strongly encouraged, given the critical importance of *OCR* on cyclic resistance. The statistical models developed herein are no substitute for a site-specific cyclic laboratory test program conducted on high quality samples.

The NGA Subduction Project is leveraged to examine the role of subduction zone earthquake ground motion characteristics on the number of equivalent loading cycles for a wide range of soils with exponents b ranging from 0.05 (moderate plasticity silt and clay) to 0.35 (dense sand). The number of loading cycles for a given magnitude subduction zone earthquake is larger than those previously computed. Magnitude scaling factors corresponding to the number of equivalent loading cycles presented herein span a smaller range as a result of the ground motion characteristics. Consideration of the uncertainty in the number of loading cycles is emphasized in forward analyses; sensitivity analyses can be used to inform project decisions in view of ground motion variability. Closed-form expressions are proposed to simplify calculation of the equivalent number of loading cycles and magnitude scaling factors. These findings and expressions should be of interest to those practicing in the Pacific Northwest of the United States, as well as globally-distributed subduction zones.

This work represents a first step towards improving the assessment of seismic risk at a given site where silty soils are present. No statistical model is free of error, as shown and quantified in this report, and the anticipated variability of seismic loading will also lead to further sources of uncertainty in the assessment of cyclic failure. Additional cyclic laboratory test data will no doubt become available over time and statistical models of the type presented in this report refined. Until that time, this report can provide practitioners and researchers a helpful reference for the typical ranges in cyclic resistance of intact nonplastic and plastic silts for use in assessing cyclic failure potential.

REFERENCES

Andersen, K. H., Kleven, A., and Heien, D. (1988). "Cyclic soil data for design of gravity structures." *Journal of Geotechnical engineering*, 114(5), 517-539. http://dx.doi.org/10.1061/(ASCE)0733-9410(1988)114:5(517)

Armstrong, R. J., and Malvick, E. J. (2016). "Practical Considerations in the use of liquefaction susceptibility criteria." *Earthquake Spectra*, 32(3), 1941-1950. http://dx.doi.org/10.1193/071114EQS100R

ASTM-D1587/1587M (2015). "Standard practice for thin-walled tube sampling of fine-grained soils for geotechnical purposes." West Conshohocken, PA: *ASTM*.

ASTM-D4186/4186M (2012). "Standard test method for one-dimensional consolidation properties of saturated cohesive soils using controlled-strain loading." West Conshohocken, PA: *ASTM*.

Azzouz, A. S., Malek, A. M., and Baligh, M. M. (1989). "Cyclic behavior of clays in undrained simple shear." *Journal of Geotechnical Engineering*, 115(5), 637-657. http://dx.doi.org/10.1061/(ASCE)0733-9410(1989)115:5(637)

Becker, D., Crooks, J., Been, K., and Jefferies, M. (1987). "Work as a criterion for determining in situ and yield stresses in clays." *Canadian Geotechnical Journal*, 24(4), 549-564. http://dx.doi.org/10.1139/t87-070

Bjerrum, L., and Landva, A. (1966). "Direct simple-shear tests on a Norwegian quick clay." *Geotechnique*, 16(1): 1-20. http://dx.doi.org/10.1680/geot.1966.16.1.1

Boone, S. J. (2010). "A critical reappraisal of preconsolidation pressure interpretations using the oedometer test." *Canadian Geotechnical Journal*, 47(3), 281–296. http://dx.doi.org/10.1139/T09-093

Boulanger, R. W., Meyers, M. W., Mejia, L. H., and Idriss, I. M. (1998). "Behavior of a fine-grained soil during the Loma Prieta earthquake." *Can. Geot. J*, 35(1): 146-158. http://dx.doi.org/10.1139/t97-078

Boulanger, R. W., and Idriss, I. M. (2004). "Evaluating the potential for liquefaction or cyclic failure of silts and clays." *Rep. UCD/CGM-04/01*, Center for Geotechnical Modeling, Department of Civil and Environmental Engineering, 131 pp.

Boulanger, R. W., and Idriss, I. M. (2006). "Liquefaction susceptibility criteria for silts and clays." *J. Geotech. Geoen. Eng*., 132(11): 1413-1426. http://dx.doi.org/10.1061/(ASCE)1090-0241(2006)132:11(1413)

Boulanger, R. W., and Idriss, I. M. (2007). "Evaluation of cyclic softening in silts and clays." *J.Geotech.Geoenviron.Eng*. 133(6): 641–652. http://dx.doi.org/10.1061/(ASCE)1090-0241(2007)133:6(641)

Boulanger, R. W., & Idriss, I. M. (2014). CPT and SPT based liquefaction triggering procedures. *Report No. UCD/CGM.-14*, Center for Geotechnical Modeling, Department of Civil and Environmental Engineering, University of California, Davis, California.

Boulanger, R. W., and Idriss, I. M. (2015). "Magnitude scaling factors in liquefaction triggering procedures." *Soil Dynamics and Earthquake Engineering*, 79, 296-303. http://dx.doi.org/10.1016/j.soildyn.2015.01.004

Boulanger, R. W., Ziotopoulou, K., and Oathes, T. J. (2022). "PM4SiltR (Version 1): A silt plasticity model with rate effects for slope stability applications." *Report No. UCD/CGM-22/04*, Center for Geotechnical Modeling, Department of Civil and Environmental Engineering, University of California, Davis, CA.

Bozorgnia, Y. and Stewart, J.P. (2020) "Data Resources for NGA-Subduction Project." *Report No. 2020/02*, Pacific Earthquake Engineering Research Center, Berkeley, CA.

Bray, J.D. and Sancio, R.B. (2006). "Assessment of the Liquefaction Susceptibility of Fine-Grained Soils." *J. Geotech. Geoen. Eng*.132(9): 1165-1177. http://dx.doi.org/10.1061/(ASCE)1090-0241(2006)132:9(1165)

Casagrande, A. (1936). "The determination of pre-consolidation load and it's practical significance." *Proc. Int. Conf. Soil Mech. Found. Eng*. Cambridge, Mass., 1936, 60.

Castro, G., and Poulos, S. J. (1977). "Factors affecting liquefaction and cyclic mobility." *J. Geotech. Geoen. Eng*. 103(6): 501 – 516. http://dx.doi.org/10.1061/AJGEB6.0000433

Cetin, K. O., Seed, R. B., Der Kiureghian, A., Tokimatsu, K., Harder Jr, L. F., Kayen, R. E., and Moss, R. E. (2004). "Standard penetration test-based probabilistic and deterministic assessment of seismic soil liquefaction potential." *Journal of Geotechnical and Geoenvironmental Engineering*, 130(12), 1314-1340. http://dx.doi.org/10.1061/(ASCE)1090-0241(2004)130:12(1314)

Chu, D. B., Stewart, J. P., Boulanger, R. W., & Lin, P. S. (2008). Cyclic softening of low-plasticity clay and its effect on seismic foundation performance. *Journal of Geotechnical and Geoenvironmental Engineering* 134(11), 1595-1608. http://dx.doi.org/10.1061/(ASCE)1090-0241(2008)134:11(1595)

Dadashiserej, A., Jana, A., Ortiz, S. C., Walters, J. J., Stuedlein, A. W., and Evans, T. M (2022a). "Monotonic, cyclic, and post-cyclic response of Willamette River silt at the Van Buren Bridge." In *Geo-Congress 2022: Geophysical and Earthquake Engineering and Soil Dynamics*, Geotechnical Special Publication No. 334, ASCE, Reston, VA. 431-443.

Dadashiserej, A., Jana, A., Stuedlein, A. W., and Evans, T. M. (2022b). “Effect of strain history on the monotonic and cyclic response of natural and reconstituted silts.” *Soil Dynamics and Earthquake Engineering*, 160, 107329. http://dx.doi.org/10.1016/j.soildyn.2022.107329

Dadashiserej, A., Jana, A., Evans, T. M., Stuedlein, A. W. (2022c). “Influence of natural soil fabric on the cyclic resistance of low and high plasticity soils.” *12th National Conference on Earthquake Engineering*, Salt Lake City, Utah 2022.

Dadashiserej, A., Jana, A., Stuedlein, A. W., Evans, T. M., Zhang, B., Xu, Z., Stokoe, K. H., and Cox, B. R. (2022d). “In-situ and Laboratory cyclic response of an alluvial plastic silt deposit.” *In Proceedings of the 20th International Conference on Soil Mechanics and Geotechnical Engineering*, Sydney 2021.

Dahl, K. R., Boulanger, R. W., DeJong, J. T., and Driller, M. W. (2010). “Effects of sample disturbance and consolidation procedures on cyclic strengths of intermediate soils.” *Proceedings of the 5th International Conference on Recent Advances in Geotechnical Earthquake Engineering and Soil Dynamics*, San Diego, Calif., May 2010. Paper No OSP1, pp. 1–20

Dahl, K. R., J. T. DeJong, R. W. Boulanger, R. Pyke, and Wahl. D. (2014). “Characterization of an alluvial silt and clay deposit for monotonic, cyclic, and post-cyclic behavior.” *Can. Geotech*. J. 51 (4): 432–440. http://dx.doi.org/10.1139/cgj-2013-0057

Dahl, K., Boulanger, R. W., and DeJong, J. T. (2018). “Trends in experimental data of intermediate soils for evaluating dynamic strength.” *Proc., 11th US National Conf. on Earthquake Engineering*. Los Angeles: Earthquake Engineering Research Institute.

DeJong, J. T., Krage, C. P., Albin, B. M., and DeGroot, D. J. (2018). “Work-based framework for sample quality evaluation of low plasticity soils.” *Journal of Geotechnical and Geoenvironmental Engineering*, 144(10), 04018074. http://dx.doi.org/10.1061/(ASCE)GT.1943-5606.0001941

Dyvik, R., Lacasse, S., Berre, T., and Raadim, B. (1987). “Comparison of truly undrained and constant volume direct simple shear tests.” *Géotechnique*, 37(1), 3-10. http://dx.doi.org/10.1680/geot.1987.37.1.3

El-Sekelly, W., Dobry, R., Abdoun, T., and Steidl, J. (2016). “Centrifuge modeling of the effect of preshaking on the liquefaction resistance of silty sand deposits. *Journal of Geotechnical and Geoenvironmental Engineering*, 142(6), 04016012. http://dx.doi.org/10.1061/(ASCE)GT.1943-5606.0001430

Green, R.A., and Terri, G.A. (2005). “Number of equivalent cycles concept for liquefaction evaluations—revisited.” *Journal of Geotechnical and Geoenvironmental Engineering*, 131(4): 477–488. http://dx.doi.org/10.1061/(ASCE)1090-0241(2005)131:4(477)

Hyodo, M., Yamamoto, Y., and Sugiyama, M. (1994). “Undrained cyclic shear behaviour of normally consolidated clay subjected to initial static shear stress. *Soils and Foundations*, 34(4), 1-11. http://dx.doi.org/10.3208/sandf1972.34.4_1

Ichinose, G. A., Thio, H. K., and Somerville, P. G. (2006). "Moment tensor and rupture model for the 1949 Olympia, Washington, earthquake and scaling relations for Cascadia and global intraslab earthquakes." *Bulletin of the Seismological Society of America*, 96(3), 1029-1037.

Idriss, I. M. (1999). "An update to the Seed-Idriss simplified procedure for evaluating liquefaction potential." *Proceedings, TRB Workshop on New Approaches to Liquefaction*, Publication No. FHWARD-99-165, Federal Highway Administration, January.

Idriss, I. M., and Boulanger, R. W. (2008). "Soil Liquefaction during Earthquakes. *EERI Monograph No. 12, Earthquake Engineering Research Institute*, 237 pp.

Idriss, I.M., & Boulanger, R. W. (2010). "SPT-based liquefaction triggering procedures." *Rep. UCD/CGM-10*, Center for Geotechnical Modeling, Department of Civil and Environmental Engineering, University of California, Davis, CA.

James, I. O., & Izien, O. F. (2014). "Audit firm characteristics and audit quality in Nigeria." *International Journal of Business and Economics Research*, 3(5), 187-195. http://dx.doi.org/10.11648/j.ijber.20140305.14

Jana, A., and Stuedlein, A.W. (2021). "Monotonic, Cyclic and Post-Cyclic Response of an Alluvial Plastic Silt Deposit." *J. of Geotech. Geoenv. Eng*. 147(3): 04020174. https://doi.org/10.1061/(ASCE)GT.1943-5606.0002462

Jana, A., and Stuedlein, A. W. (2022). "Dynamic, in situ, nonlinear-inelastic response and post-cyclic strength of a plastic silt deposit." *Canadian Geotechnical Journal*, 59(1), 111-128. http://dx.doi.org/10.1139/cgj-2020-0652

Kishida, T., and Tsai, C. C. (2014). "Seismic demand of the liquefaction potential with equivalent number of cycles for probabilistic seismic hazard analysis." *Journal of Geotechnical and Geoenvironmental Engineering*, 140(3), 04013023. http://dx.doi.org/10.1061/(ASCE)GT.1943-5606.0001033

Ladd, C. C., and Foott, R. (1974). "New design procedure for stability of soft clays." *J. Geotech. Engrg. Div.*, 100(7), 763–786. http://dx.doi.org/10.1061/AJGEB6.0000066

Ladd, C. C. (1991). "Stability evaluation during staged construction." *Journal of Geotechnical Engineering*, 117(4), 540-615. http://dx.doi.org/10.1061/(ASCE)0733-9410(1991)117:4(540)

Landon, M. M., DeGroot, D. J., and Sheahan, T. C. (2007). "Nondestructive sample quality assessment of a soft clay using shear wave velocity." *J. Geot. Geoenv. Eng*, 133(4), 424-432. http://dx.doi.org/10.1061/(ASCE)1090-0241(2007)133:4(424)

Lee, K.L., and Chan, K. (1972). "Number of equivalent significant cycles in strong motion earthquakes." *Proceedings of the International Conference on Microzonation for Safer Construction Research and Application*, University of Washington, Seattle, Washington, Vol. 2, pp. 609–627.

Lefebvre, G., and LeBouef, D. (1987). "Rate effects and cyclic loading of sensitive clays." *J. Geot. Geoenv. Eng*, 113 (5): 476–489. http://dx.doi.org/10.1061/(ASCE)0733-9410(1987)113:5(476)

Lefebvre, G., and Pfendler, P. (1996). "Strain rate and preshear effects in cyclic resistance of soft clay. *Journal of Geotechnical Engineering*, 122(1), 21-26. http://dx.doi.org/10.1061/(ASCE)0733-9410(1996)122:1(21)

Mitchell, J. K., and Soga, K. (2005). "Fundamentals of soil behavior. *John Wiley & Sons*, New York.

Pitarka, A., Thio, H. K., Somerville, P., & Bonilla, L. F. (2013). "Broadband ground-motion simulation of an intraslab earthquake and nonlinear site response: 2010 Ferndale, California, earthquake case study." *Seismological Research Letters*, 84(5), 785-795.

Sanin, M. V., and Wijewickreme D. (2006). "Cyclic shear response of channel-fill Fraser River Delta silt. *Soil Dyn. Earthq. Eng*. 26 (9): 854–869. http://dx.doi.org/10.1016/j.soildyn.2005.12.006

Sanin, M. V. (2010). "Cyclic shear loading response of Fraser River Delta silt." *Ph.D. dissertation*, Dept. of Civil Engineering, Univ. of British Columbia, Vancouver, BC.

Seed, H. B., and Idriss, I. M. (1971). "Simplified procedure for evaluating soil liquefaction potential. *Journal of Soil Mechanics & Foundations Division*, 97(9), 1249 – 1273. http://dx.doi.org/10.1061/JSFEAQ.0001662

Seed, H. B., Idriss I. M., Makdisi, F., and Banerjee, N. (1975). "Representation of irregular stress time histories by equivalent uniform stress series in liquefaction analyses." *Rep. No. EERC* 75-29. Univ. of California at Berkeley, Berkeley, CA:

Simpson, D., and Evans, T. M. (2015). "Behavioral thresholds in mixtures of sand and kaolinite clay." *Journal of Geotechnical and Geoenvironmental Engineering*, 142(2), 04015073. http://dx.doi.org/10.1061/(ASCE)GT.1943-5606.0001391

Soysa, A. N. (2015). "Monotonic and cyclic shear loading response of natural silts." *Ph.D. dissertation*, Dept. of Civil Engineering, Univ. of British Columbia, Vancouver, BC.

Stokoe, K.H., Roberts, J.N., Hwang, S., Cox, B.R., and Menq F. (2016). "Effectiveness of inhibiting liquefaction triggering by shallow ground improvement methods: field shaking trials with T-Rex at one area in Christchurch, New Zealand." *24th Geot. Conf. of Torino*, Turin, Italy.

Stokoe, K. H. & Santamarina, J. C. (2000). "Seismic-wave-based testing in geotechnical engineering." In *GeoEng 2000*, pp. 1490– 1536. Pennsylvania, Technomic Publishing Co., Melbourne, Australia

Stuedlein, A. W., Dadashiserej, A., Jana, A., Evans, T. M. (2023). "Liquefaction susceptibility and cyclic response of intact nonplastic and plastic silts." *J. Geotech. Geoen. Eng*., 149(1), 04022125. http://dx.doi.org/10.1061/(ASCE)GT.1943-5606.0002935

Thevanayagam, S., and Martin, G. (2002). “Liquefaction in silty soils - screening and remediation issues.” *Soil Dynamics and Earthquake Engineering*, 22(9-12), 1035-1042. http://dx.doi.org/10.1016/S0267-7261(02)00128-8

Verma, P., Seidalinova, A. and Wijewickreme, D. (2019). “Equivalent number of uniform cycles versus earthquake magnitude relationships for fine-grained soils.” *Canadian Geotechnical Journal*, 56(11), pp.1596-1608. http://dx.doi.org/10.1139/cgj-2018-0331

Wasserstein, R.L. and Lazar, N.A. (2016). “The ASA's Statement on p-Values: Context, Process, and Purpose.” *American Statistician*. 70 (2): 129–133. doi:10.1080/00031305.2016.1154108.

Wijewickreme, D., Soysa, A., and Verma, P. (2019). “Response of natural fine-grained soils for seismic design practice: A collection of research findings from British Columbia, Canada. *Soil Dyn. Earthquake Eng*. 124: 280–296. http://dx.doi.org/10.1016/j.soildyn.2018.04.053

Woodward-Clyde (1992). “California Water Operations Center—Site evaluation and remediation—Conceptual design.” *Appendix E: CWOC site characterization memo*, Woodward-Clyde Consultants, Oakland, Calif.

Youd, T. L., and Idriss, I. M. (2001). “Liquefaction resistance of soils: summary report from the 1996 NCEER and 1998 NCEER/NSF workshops on evaluation of liquefaction resistance of soils.” *Journal of geotechnical and geoenvironmental engineering*, 127(4), 297-313. http://dx.doi.org/10.1061/(ASCE)1090-0241(2001)127:4(297)

Zergoun, M., and Vaid, Y. (1994). “Effective stress response of clay to undrained cyclic loading. *Canadian Geotechnical Journal*, 31(5), 714-727. http://dx.doi.org/10.1139/t94-083

APPENDIX A

Table A1 Summary of constant-volume, monotonic DSS test results.

Test Designation	Vertical Effective Consolidation Stress, σ'_{vc} (kPa)	Over-consolidation Ratio, OCR	Undrained Shear Strength, $s_{u,DSS}$ (kPa)	Natural Moisture Content, w_n (%)	Degree of Saturation, S (%)	Plasticity Index, PI	Void Ratio, e	Fines Content, FC (%)
A-UT-M1	36	3.1	29	71	100.0	14	1.83	98
A-BL-M1	32	4.2	22	50	100.0	15	1.26	91
B-13-M1	48	2.0	21	47	93.7	13	1.33	95
B-14-M1	160	1.5	57	40	100.0	11	0.95	80
B-14-M2	100	8.0	133	42	100.0	NA[1]	0.77	NA
B-14-M3	267	3.0	163	42	100.0	11	0.81	99
C-7-M1	80	1.5	39	NA	NA	NA	NA	NA
C-10-M1	100	1.6	47	NA	NA	NA	NA	NA
D-2-M1	138	1.6	71	53	99.0	22	1.41	99
D-2-M2	106	1.9	54	86	96.0	27	2.37	91
D-2-M3	106	1.9	50	87	NA	28	NA	99
D-2-M4	262	1.0	79	74	98.5	27	1.98	95
D-2-M5	106	4.0	100	65	99.0	33	1.73	99
D-2-M6	106	3.0	83	NA	99.0	27	NA	94
D-2-M7	118	2.1	63	85	98.0	26	2.29	96
D-2-M8	102	1.9	45	70	100.0	23	1.85	99

Table A1 (Continued).

Test Designation	Vertical Effective Consolidation Stress, σ'_{vc} (kPa)	Over-consolidation Ratio, OCR	Undrained Shear Strength, $s_{u,DSS}$ (kPa)	Natural Moisture Content, w_n (%)	Degree of Saturation, S (%)	Plasticity Index, PI	Void Ratio, e	Fines Content, FC (%)
D-2-M9	100	1.9	50	69	99.6	23	1.83	99
E-1-M1	95	2.0	39	46	100.0	12	NA	98
E-1-M2	300	1.0	93	43	100.0	NA	0.98	NA
E-1-M3	75	4.0	70	43	100.0	NA	0.95	NA
E-1-M4	38	8.0	70	36	100.0	NA	0.93	NA
E-2-M1	100	2.0	46	73	100.0	28	NA	99
E-3-M1	107	2.1	50	92	100.0	24	NA	99
E-3-M2	300	1.0	91	74	100.0	25	1.62	99
E-3-M3	75	4.0	75	72	100.0	19	1.57	97
E-3-M4	38	8.0	68	58	100.0	19	1.26	96
E-5-M1	125	2.2	58	39	100.0	15	NA	98
F-1-M1	120	2.6	45	NA	NA	NP[2]	NA	34
F-2-M1	150	2.4	57	39	100.0	3	0.95	38
F-3-M1	158	2.7	63	37	100.0	20	NA	71
G-2-M1	160	1.2	65	40	100.0	NA	0.92	NA
H-5-M1	60	2.6	39	29	100.0	12	0.76	NA
H-11-M1	104	1.9	81	26	100.0	0	0.72	NA

[1]Not available.
[2]Non-plastic.

Table A2 Summary of constant-volume, stress-controlled, cyclic DSS test results interpreted for varying cyclic shear strain failure criteria comprising the ***training dataset***.

Test Designation	Sample Depth Interval (m)	Vertical Effective Consolidation Stress, σ'_{vc} (kPa)	Overconsolidation Ratio, OCR	Void Ratio, e	Fines Content, FC (%)	Plasticity Index, PI	Undrained Shear Strength Ratio, $s_{u,DSS}/\sigma'_{vc}$	Cyclic Stress Ratio, CSR	Cyclic Strength Ratio, $\tau_{cyc}/s_{u,DSS}$	$N_{\gamma=1\%}$	$N_{\gamma=2\%}$	$N_{\gamma=3\%}$	$N_{\gamma=3.75\%}$	$N_{\gamma=5\%}$	$N_{\gamma=8\%}$	$N_{\gamma=10\%}$
A-UT-4	2.6 - 3.2	36	3.1	1.44	97	14	0.77	0.38	0.53	1.2	7.3	77	NA[1]	NA	NA	NA
A-UT-6			3.2	1.39	96	12		0.42	0.59	0.24	1.3	9.3	21	26	NA	NA
A-UT-7			3.0	1.39	97	15		0.48	0.67	0.21	1.2	4.8	8	NA	NA	NA
B-13-15	2.4 - 3.2	50	1.9	1.35	91	16	0.41	0.44	1.16	0.16	1.2	2.3	4.2	7.3	12	15
B-13-18				1.38	NA	15		0.39	1.03	0.18	2.3	5.3	8.2	12	NA	NA
B-13-19				1.35	95	14		0.33	0.88	0.21	3.2	7.2	11	17	NA	NA
B-13-20				1.47	NA	15		0.31	0.82	0.75	27	49	65	84	NA	NA
B-13-21				1.50	NA	15		0.33	0.89	0.22	7.8	18	25	33	NA	NA
B-14-7	8.5 - 9.3	160	1.5	0.95	86	13	0.35	0.29	0.90	0.13	1.2	2.3	4.2	5.3	NA	NA
B-14-8				0.92	81	13		0.24	0.75	0.20	12	22	26	30	35	37
B-14-9				0.90	80	11		0.21	0.66	0.21	14	28	34	39	47	50
B-14-14				0.98	99	15		0.27	0.85	0.14	0.24	1.8	3.2	4.3	7.2	8.2
B-14-17				1.00	NA	13		0.27	0.85	0.13	0.23	2.3	4.2	6.2	NA	NA
B-14-22				0.89	98	13		0.26	0.81	0.14	0.75	6.8	11	16	24	NA
C-7-1	5.3 - 5.9	80	1.5	1.03	86	9	0.48	0.22	0.51	0.23	5.3	9.3	12	16	26	32
C-7-2				0.87	93	9		0.31	0.70	0.15	0.24	0.74	1.3	1.7	3.7	4.8
C-7-3				NA	95	9		0.17	0.40	3.3	30	45	55	70	NA	NA

Table A2 (Continued).

D-2-1		129	2.2	2.06	98	25	0.60	0.35	0.67	0.16	0.70	2.8	NA	NA	NA	NA
D-2-2		114	1.7	1.24	NA	22	0.46	0.41	0.96	0.11	0.16	0.21	0.24	0.28	2.2	4.2
D-2-3		108	2.0	2.19	99	29	0.73	0.41	0.86	0.19	0.69	0.76	1.7	6.8	NA	NA
D-2-5		100	2.1	1.28	76	14	0.38	0.47	0.93	0.10	0.13	0.16	0.18	0.21	0.26	0.31
D-2-6		100	2.1	1.79	96	31	0.67	0.39	0.77	0.14	0.22	0.30	0.82	NA	NA	NA
D-2-7		100	2.1	2.01	98	31	0.67	0.36	0.73	0.14	0.22	1.2	2.3	12	NA	NA
D-2-9		100	2.0	2.22	99	34	0.74	0.43	0.74	0.11	0.17	0.22	0.26	2.2	16	20
D-2-10	9.1 - 11.2	118	2.1	2.16	93	34	0.63	0.41	0.80	0.12	0.19	0.26	0.75	4.8	NA	NA
D-2-11		118	2.1	2.24	95	39	0.63	0.30	0.60	0.14	0.23	23	NA	NA	NA	NA
D-2-12		118	1.9	2.10	93	39	0.63	0.38	0.82	1.01	0.18	0.25	2.3	15	NA	NA
D-2-13		118	1.9	2.05	NA	28	0.58	0.37	0.78	0.13	0.19	0.74	2.8	NA	NA	NA
D-2-14		118	2.0	2.19	99	27	0.63	0.29	0.59	0.22	1.8	30	NA	NA	NA	NA
D-2-15		105	1.9	2.24	99	28	0.65	0.27	0.57	0.18	6.8	46	89	143	NA	NA
D-2-19		118	1.9	2.24	99	26	0.65	0.36	0.77	0.12	0.19	0.79	2.2	4.7	8.8	12
D-2-27		122	2.0	2.24	99	21	0.43	0.35	0.77	0.13	0.19	0.74	2.8	7.7	NA	NA
D-2-31		106	2.0	2.24	99	28	0.64	0.30	0.63	0.16	2.2	32	99	252	NA	NA
E-1-1				1.10	94	12		0.30	0.80	0.15	0.26	0.74	0.80	1.7	2.7	3.7
E-1-2		95	2.0	1.17	87	10	0.41	0.24	0.65	0.21	2.8	4.7	5.8	7.7	11	13
E-1-3				1.13	89	10		0.19	0.52	3.2	12.3	15	17	19	26	NA
E-1-4	7.3 - 7.9			1.13	100	12		0.15	0.41	106	139	150	156	164	181	NA
E-1-8				1.10	NA	11		0.20	0.70	0.14	2.8	5.7	6.8	8.7	NA	NA
E-1-9		250	1.0	1.05	NA	11	0.31	0.15	0.52	0.21	38	42	44	47	NA	NA
E-1-10				1.05	NA	11		0.25	0.87	0.11	0.19	0.72	1.3	1.7	2.7	NA
E-1-11				1.03	NA	11		0.13	0.47	0.21	83	91	93	96	101	103
E-2-1				1.92	99	26		0.36	0.83	0.13	0.22	1.7	2.8	6.8	25	36
E-2-2		100	2.0	2.01	99	28	0.47	0.40	0.92	0.12	0.18	0.25	0.80	2.8	8.8	13
E-2-3				1.98	99	28		0.29	0.68	0.16	2.8	45	149	336	559	NA
E-2-4				1.94	99	28		0.27	0.63	0.21	17	526	NA	NA	NA	NA
E-2-6	8.2 - 8.8			1.87	NA	28		0.29	1.04	0.09	0.14	0.20	0.24	1.7	4.8	6.8
E-2-7				1.95	NA	28		0.24	0.83	0.11	0.18	0.75	3.8	12	29	33
E-2-9		215	1.0	1.96	NA	28	0.31	0.21	0.73	0.10	0.18	1.2	6.3	23	62	76
E-2-10				1.98	NA	28		0.19	0.66	0.12	0.26	252	NA	NA	NA	NA
E-2-11				1.99	NA	28		0.21	0.73	0.10	0.20	10	56	NA	NA	NA

Table A2 (Continued).

E-3-1	9.4 - 10.0	107	2.1	2.33	99	24	0.47	0.31	0.73	0.16	1.8	65	217	534	NA	NA
E-3-2				2.30	99	27		0.44	1.02	0.11	0.18	0.27	1.3	4.2	12	16
E-3-3				2.19	99	27		0.36	0.84	0.14	0.71	3.7	12	46	125	147
E-3-4				2.22	94	24		0.33	0.77	0.14	0.24	12	37	103	NA	NA
E-5-1	11.4 - 12.0	125	2.2	0.99	100	15	0.46	0.39	0.92	0.13	0.20	0.74	0.81	1.8	4.7	5.7
E-5-2				0.94	99	15		0.35	0.83	0.12	0.20	0.77	1.7	2.8	5.7	6.8
E-5-3				0.94	100	15		0.35	0.83	0.12	0.19	0.76	1.7	2.8	5.7	6.7
E-5-4				0.96	99	15		0.31	0.74	0.15	0.28	1.7	2.8	4.8	10	12
E-5-5				0.68	99	15		0.22	0.51	0.21	46	162	209	241	269	277
E-5-6				1.00	98	15		0.26	0.62	0.18	3.7	18	26	36	53	56
F-1-1	6.2 – 6.9	120	2.6	0.84	62	NP[2]	0.38	0.30	0.87	0.14	0.23	0.75	0.80	1.2	1.8	2.3
F-1-2				0.95	62			0.20	0.57	16.8	46	54	58	62	67	69.3
F-1-3				0.89	47			0.24	0.71	0.19	2.7	4.3	5.3	6.7	8.8	10.7
F-1-4				0.99	47			0.18	0.52	14.3	34	39	41	45	50	NA
F-1-5				0.91	41			0.15	0.42	428	679	706	717	NA	NA	NA
F-2-1	8.5 - 9.1	150	2.4	0.84	44	6	0.38	0.29	0.85	0.12	0.19	0.73	0.78	1.2	2.2	3.2
F-2-2				0.86	48	6		0.21	0.62	0.22	11	17	19	22	27	29
F-2-3				0.81	38	3		0.19	0.54	0.23	13	19	22	25	31	33
F-2-4				0.81	30	3		0.15	0.45	25	55	61	63	67	73	76
F-2-5				0.76	36	NP		0.22	0.65	0.19	2.3	4.2	5.2	6.2	8.2	10
F-2-6				0.68	29	NP		0.14	0.39	36	73	79	82	85	90	NA
F-3-1	9.5 - 10.1	158	2.7	0.64	62	11	0.40	0.25	0.68	0.15	0.71	1.7	1.7	2.7	4.7	5.7
F-3-2				0.67	60	11		0.22	0.61	0.18	1.7	3.7	4.8	7.7	13	15
F-3-3				0.76	41	4		0.16	0.45	8.8	83	99	105	112	120	124
F-3-4				0.80	73	4		0.30	0.81	0.12	0.22	1.3	1.8	2.7	4.7	5.7
F-3-5				0.81	83	4		0.19	0.53	0.22	14	28	33	39	51	NA
F-3-7				0.88	88	20		0.35	0.96	0.11	0.19	0.70	0.72	0.8	1.8	2.7
H-5-2	3.5	60	2.6	0.87	NA	12	0.64	0.20	0.34	NA	NA	3.6	4.6	NA	NA	NA
H-11-3	7.9	104	1.9	0.69	NA	0	0.77	0.15	0.21	36	47	54	56	NA	NA	NA
H-11-4				0.74	NA	0	0.77	0.25	0.35	1.3	3.8	7.8	NA	NA	NA	NA

Table A2 (Continued).

I-1-1	9.2	158	1.0	NA	NA	29	NA	0.24	NA	2.5	13	NA	NA	NA	NA	NA
I-8-3	9.6	78	1.6	1.27	NA	0	0.42	0.23	0.59	NA	NA	NA	NA	NA	NA	NA
I-1-5	3.1	411	1.0	1.04	NA	0	0.21	0.15	0.78	NA	90	96	98	NA	NA	NA
J-1-1	4.7	82	4	0.61	NA	1	NA	0.40	NA	NA	NA	NA	0.20	NA	NA	NA
J-2-2	6.7	105	4	0.39	NA	7		0.40		0.25	0.70	1.3	NA	1.7	2.2	NA
J-2-3	6.5	105	4	0.50	NA	13		0.40		0.75	NA	2.8	3.2	NA	NA	NA
J-2-5	6.8	105	4	0.78	NA	23		0.40		1.3	6.3	NA	NA	NA	NA	NA

[1] Not available.
[2] Non-plastic.

Table A3 Summary of the constant-volume, stress-controlled cyclic DSS test results used as the *testing dataset*.

Test Designation	Sample Depth Interval (m)	Effective Consolidation Stress σ'_{v0} (kPa)	*OCR*	Void Ratio *e*	Fines Content *FC* (%)	*PI*	Undrained Shear Strength Ratio, $s_{u,DSS}/\sigma'_{v0}$	*CSR*	Cyclic Strength Ratio, $\tau_{cyc}/s_{u,DSS}$	$N_{\gamma=1\%}$	$N_{\gamma=2\%}$	$N_{\gamma=3\%}$	$N_{\gamma=3.75\%}$	$N_{\gamma=5\%}$	$N_{\gamma=8\%}$	$N_{\gamma=10\%}$	Reference
PC-A-01		231	1.0	0.73		18		0.18	0.65	NA	NA	195	NA	NA	NA	NA	
PC-A-02		231	1.0	0.87		17		0.18	0.67	6.0	26	46	51	60	NA	NA	
PC-A-03		215	1.0	0.84		27	0.24 - 0.29	0.20	0.75	NA	NA	26	NA	NA	NA	NA	
PC-A-04		215	1.0	0.79		26		0.23	0.84	NA	0.75	3.6	4.8	7.8	11	NA	
PC-A-05	1.3 – 3.4	213	1.0	0.8	93 - 100	23		0.25	0.91	NA	NA	0.20	0.25	1.3	NA	NA	
PC-A-06		241	1.0	0.66		13		0.24	0.88	NA	NA	0.25	0.25	NA	NA	NA	
PC-A-07		232	2.0	0.69		24		0.30	0.63	0.25	22	44	50	59	NA	NA	
PC-A-08		225	2.0	0.66		12	0.44 - 0.53	0.35	0.73	0.20	4.3	8.0	9.3	12	NA	NA	Dahl et al. (2014)
PC-A-09		223	2.0	0.64		9		0.40	0.82	0.20	2.2	3.2	4.7	5.7	NA	NA	
PC-A-10		239	2.0	0.66		15		0.40	0.82	NA	0.25	1.7	2.3	3.7	NA	NA	
PC-B-01		225	1.0	0.56		0		0.10		124	128	130	133	133	NA	NA	
PC-B-02		225	1.0	0.56		0		0.14		13	NA	18	NA	NA	NA	NA	
PC-B-03	4.9 – 5.4	450	1.0	0.51	35 – 77	0	NA[1]	0.14	NA	26	30	33	33	34	NA	NA	
PC-B-04		225	1.0	0.67		0		0.17		0.75	1.7	2.2	2.8	3.6	NA	NA	
PC-B-05		225	1.0	0.63		0		0.20		NA	NA	1.1	NA	NA	NA	NA	
PC-B-06		225	1.0	0.68		1		0.23		NA	NA	0.69	NA	1.3	NA	NA	
FRS100-014		101	1.0	0.97		4	0.30	0.14	0.51	NA	NA	NA	143	148	NA	NA	
FRS-100-017		101	1.0	0.89		4	0.30	0.17	0.62	NA	NA	NA	8.0	10	13	14	
FRS100-020	5.6 - 8.7	97	1.0	0.88	90	4	0.30	0.20	0.73	NA	1.8	NA	4.0	4.8	8	8.8	
FRS100-029		101	1.0	0.99		4	0.30	0.29	1.07	NA	NA	NA	1.0	1.8	3	NA	Sanin (2010)
FRS100-016		99	1.0	0.94		4	0.30	0.15	0.55	NA	NA	NA	26	NA	NA	NA	
KIN080-003		80	1.0	0.96		17	NA	0.24	NA	1.8	3.8	6.8	10	NA	NA	NA	
KIN080-001	NA	80	1.0	0.90	99	17	NA	0.26	NA	NA	NA	1.8	3.0	NA	NA	NA	
KIN080-002		81	1.0	0.89		17	NA	0.17	NA	NA	NA	NA	90	NA	NA	NA	
CT150-45		150	1.0	1.03		5	0.22	0.30	1.44	NA	NA	NA	0.30	NA	NA	NA	
CT150-30		148	1.0	1.01		5	0.22	0.20	0.98	NA	NA	NA	4.8	NA	NA	NA	
CT150-22.5	5.0 - 7.0	149	1.0	0.91	65 - 80	5	0.22	0.15	0.73	18	NA	23	24	NA	NA	NA	Soysa (2015)
CT150-20		148	1.0	1.00		5	0.22	0.14	0.66	NA	NA	NA	169	NA	NA	NA	
CT150-18.75		147	1.0	0.93		5	0.22	0.13	0.61	NA	79	81	83	NA	NA	NA	

Table A3 (Continued).

JS100-20		101	1.0	1.15		7	0.23	0.20	0.91	NA	0.75	NA	1.8	NA	NA	NA	
JS100-17		99	1.0	0.99		7	0.23	0.17	0.78	NA	NA	4.8	5.8	6.8	NA	NA	
JS100-16	4.2 -5.5	101	1.0	1.02	80	7	0.23	0.17	0.77	NA	NA	NA	14	NA	NA	NA	
JS100-15		98	1.0	1.33		7	0.23	0.16	0.72	NA	NA	NA	30	NA	NA	NA	
JS100-13		100	1.0	1.25		7	0.23	0.13	0.61	NA	NA	NA	92	NA	NA	NA	
MD075-30		77	1.0	1.70		34	NA	0.39	NA	NA	NA	NA	0.80	NA	NA	NA	
MD075-25	4.9 - 6.2	76	1.0	1.70	100	34	NA	0.33	NA	NA	NA	NA	7.8	NA	NA	NA	
MD075-20		76	1.0	1.84		34	NA	0.26	NA	NA	NA	NA	16	NA	NA	NA	
MD075-18		75	1.0	1.67		34	NA	0.24	NA	NA	NA	NA	107	NA	NA	NA	
A-BL-2				1.49	82	10		0.30	0.47	2.30	15	21	25	31	52	NA	
A-BL-3				1.41	77	11		0.37	0.57	0.27	2.3	3.7	4.8	6.8	14	NA	
A-BL-4	2.4 – 3.0	32	4.2	1.30	NA	11	0.70	0.42	0.66	0.21	0.32	1.2	1.3	2.2	4.2	6.2	Stuedlein et al. (2023)
A-BL-5				1.35	92	19		0.44	0.69	0.19	0.26	1.2	1.3	2.3	5.3	8.3	
A-BL-6				1.51	90	19		0.29	0.45	6.28	37	60	75	96	NA	NA	
C-10-1				1.03	96	9		0.24	0.57	0.20	2.8	4.7	5.7	7.7	11	13	
C-10-2	8.5 – 9.1	100	1.6	0.87	91	9	0.46	0.17	0.40	66.28	116	133	143	155	NA	NA	Current Study
C-10-3				0.95	NA	9		0.29	0.69	0.13	0.21	1.2	1.3	2.3	NA	NA	
G-2-1				0.94	70	10		0.30	0.80	0.13	0.21	1.2	1.7	2.3	4.2	5.3	
G-2-2	14.6 - 15.2	160	1.2	0.96	70	10	0.40	0.25	0.67	0.14	0.25	3.2	4.3	6.3	10	12	Current Study
G-2-4				NA	65	11		0.19	0.52	0.21	22	29	32	36	42	45	
G-2-5				NA	76	11		0.17	0.45	4.77	120	147	156	167	183	190	

[1] Not available.

APPENDIX B

Table B1 Summary of the statistical analysis conducted on linear models for exponent *b* regressed on *e*, *OCR*, and *PI* using the *training dataset* corresponding to $N_{\gamma=3\%}$.

Predictor Variable	Linear Model	Estimate		*F*-statistics	RSE	*p*-value	R^2
		a_0	a_1				
e	$b = a_0*e + a_1$	-0.0526	0.1686	22.51	0.0208	4.77e-04	0.65
PI	$b = a_0*PI + a_1$	-0.0030	0.1440	22.86	0.0207	4.48e-04	0.66
OCR	$b = a_0*OCR + a_1$	0.0049	0.0895	0.09	0.0351	7.68e-01	0.01

Table B2 Summary of the multicollinearity investigation between predictors in the linear models for exponent *b* using the *training dataset* corresponding to $N_{\gamma=3\%}$.

Linear Model	Predictor Variable	VIF	Estimate			*F*-statistics	RSE	*p*-value	R^2
			a_0	a_1	a_2				
Eq. (5.1)	*PI* *e*	5.36 5.36	-0.0016	-0.0270	0.1589	12.12	0.0206	1.66e-03	0.688
Eq. (5.2)	*PI*	1.00	-0.0030	0.1440	NA[1]	22.86	0.0207	4.48e-04	0.656

[1]Not Applicable.

Table B3 Summary of statistical analysis using software package *R* for investigation of contribution of *e*, *PI*, *OCR*, and *N* in prediction of *CRR* in linear models using the *training dataset* corresponding to $N_{\gamma=3\%}$.

Predictor Variable	Linear Model	Estimate		*F*-statistics	RSE	*p*-value	R^2
		a_0	a_1				
e	$CRR = a_0*e + a_1$	0.0603	0.2100	14.35	0.0835	2.85e-04	0.15
PI	$CRR = a_0*PI + a_1$	0.0041	0.2245	26.35	0.0786	1.78e-06	0.24
OCR	$CRR = a_0*OCR + a_1$	0.0458	0.1944	11.56	0.0844	1.03e-03	0.12
N	$CRR = a_0*N + a_1$	-0.0003	0.2992	10.38	0.0848	1.83e-03	0.11

Table B4 Summary of the multicollinearity investigation between predictors in linear models for *CRR* using the *training dataset* corresponding to $N_{\gamma=3\%}$.

Linear Model	Predictor Variable	VIF	Estimate					F-statistics	RSE	*p*-value	R^2
			b_0	b_1	b_2	b_3	b_4				
Eq. (5.4)	*e*	4.21	0.0155	0.0046	0.0688	-0.0003	0.0632	20.25	0.061	4.64e-13	0.55
	PI	4.17									
	OCR	1.10									
	N	1.03									
Eq. (5.5)	*PI*	1.13	NA	0.0053	0.0678	-0.0003	0.0743	32.45	0.061	9.03e-14	0.55
	OCR	1.12									
	N	1.01									

[1] Not Applicable.

Table B5 Summary of statistical analysis using software package *R* for investigation of contribution of *e*, *PI*, *OCR*, and *N* in estimation of $\tau_{cyc}/s_{u,DSS}$ in linear models using the *training dataset* corresponding to $N_{\gamma=3\%}$.

Predictor Variable	Linear Model	Estimate		*F*-Statistics	RSE	*p*-Value	R^2
		s_0	s_1				
e	$\tau_{cyc}/s_{u,DSS} = s_0*e + s_1$	0.1027	0.5650	8.67	0.17	4.26e-03	0.10
PI	$\tau_{cyc}/s_{u,DSS} = s_0*PI + s_1$	0.0070	0.5935	15.00	0.17	2.20e-04	0.16
OCR	$\tau_{cyc}/s_{u,DSS} = s_0*OCR + s_1$	-0.0719	0.8484	3.60	0.18	6.13e-02	0.04
N	$\tau_{cyc}/s_{u,DSS} = s_0*N + s_1$	-0.0006	0.7279	9.90	0.17	2.33e-03	0.11

APPENDIX C

Table C1 Subduction zone ground motions used to develop the number of equivalent loading cycles and magnitude scaling factors in Section 6.

NGASub RSN	Database Region	Earthquake Name	Year	Earthquake Magnitude	Hypocenter Depth (km)	Epicenter distance (km)	Hypocenter Distance (km)	Station Name	Vs30 (m/s)	PGA (g)	PGV (cm/sec)	PGD (cm)
1002304	Alaska	Aleutian Islands, Alaska	2013	7.00	26.7	119	122	ADK	635	0.023	1.036	0.271
3001943	CentralAmerica&Mexico	Michoacan, Mexico	1985	7.99	16.3	390	390	CENTRAL DE ABASTOS FRIGORIFICO	61	0.085	30.415	16.082
3001944	CentralAmerica&Mexico	Michoacan, Mexico	1985	7.99	16.3	389	389	CENTRAL DE ABASTOS OFICINAS	53	0.075	40.994	25.920
3001945	CentralAmerica&Mexico	Michoacan, Mexico	1985	7.99	16.3	379	379	CU01, IDEI LABORATORIO INSTRUMENTACION SISMICA	292	0.032	9.222	7.973
3001946	CentralAmerica&Mexico	Michoacan, Mexico	1985	7.99	16.3	379	379	CUIP, IDEI PATIO	292	0.034	9.471	7.905
3001947	CentralAmerica&Mexico	Michoacan, Mexico	1985	7.99	16.3	379	379	CUMV, MESA VIBRADORA	292	0.037	9.493	6.815
3001948	CentralAmerica&Mexico	Michoacan, Mexico	1985	7.99	16.3	385	385	SCT B-1	69	0.143	50.584	20.496
3001949	CentralAmerica&Mexico	Michoacan, Mexico	1985	7.99	16.3	469	469	SISMEX PUEBLA	429	0.032	7.323	3.277
3001950	CentralAmerica&Mexico	Michoacan, Mexico	1985	7.99	16.3	381	381	SISMEX VIVEROS	281	0.046	10.890	6.501
3001951	CentralAmerica&Mexico	Michoacan, Mexico	1985	7.99	16.3	380	381	TACUBAYA	568	0.034	10.231	8.535
3001952	CentralAmerica&Mexico	Michoacan, Mexico	1985	7.99	16.3	394	395	TLAHUAC BOMBAS	62	0.116	57.063	38.093
3001953	CentralAmerica&Mexico	Michoacan, Mexico	1985	7.99	16.3	392	392	TLAHUAC DEPORTIVO	62	0.112	37.686	19.300
3001954	CentralAmerica&Mexico	Michoacan, Mexico	1985	7.99	16.3	251	251	ATOYAC, Iglesia	429	0.055	6.038	3.605
3001955	CentralAmerica&Mexico	Michoacan, Mexico	1985	7.99	16.3	133	134	AEROPUERTO ZIHUATANEJO	392	0.147	18.769	14.164
3001957	CentralAmerica&Mexico	Michoacan, Mexico	1985	7.99	16.3	275	275	CAYACO	353	0.042	3.700	1.445
3001958	CentralAmerica&Mexico	Michoacan, Mexico	1985	7.99	16.3	291	292	COYUCA	429	0.037	6.206	2.202
3001959	CentralAmerica&Mexico	Michoacan, Mexico	1985	7.99	16.3	348	349	CERRO DE PIEDRA	392	0.021	3.030	1.074
3001960	CentralAmerica&Mexico	Michoacan, Mexico	1985	7.99	16.3	355	355	LAS MESAS	517	0.020	2.816	0.814
3001961	CentralAmerica&Mexico	Michoacan, Mexico	1985	7.99	16.3	188	189	PAPANOA	517	0.149	9.920	7.634
3001962	CentralAmerica&Mexico	Michoacan, Mexico	1985	7.99	16.3	231	231	EL SUCHIL	517	0.091	11.495	7.143
3001963	CentralAmerica&Mexico	Michoacan, Mexico	1985	7.99	16.3	332	333	TEACALCO	517	0.037	6.777	4.575
3001964	CentralAmerica&Mexico	Michoacan, Mexico	1985	7.99	16.3	84	85	LA UNION	517	0.159	17.500	9.682
3001965	CentralAmerica&Mexico	Michoacan, Mexico	1985	7.99	16.3	43	46	VILLITA MARGEN DERECHA	429	0.118	16.470	11.909
3001966	CentralAmerica&Mexico	Michoacan, Mexico	1985	7.99	16.3	324	324	LA VENTA	429	0.019	3.069	0.797
3001968	CentralAmerica&Mexico	Zihuatanejo, Mexico	1985	7.56	20.2	38	43	AEROPUERTO ZIHUATANEJO	392	0.157	16.097	4.975
3001971	CentralAmerica&Mexico	Zihuatanejo, Mexico	1985	7.56	20.2	88	90	PAPANOA	517	0.240	8.222	6.358
3001972	CentralAmerica&Mexico	Zihuatanejo, Mexico	1985	7.56	20.2	132	133	EL SUCHIL	517	0.075	6.639	3.482
3001992	CentralAmerica&Mexico	Michoacan, Mexico	1985	7.99	16.3	266	267	EL PARAISO	519	0.081	6.448	1.672
3001996	CentralAmerica&Mexico	Zihuatanejo, Mexico	1985	7.56	20.2	153	155	ATOYAC, Iglesia	429	0.075	3.331	0.418

3001998	CentralAmerica&Mexico	Zihuatanejo, Mexico	1985	7.56	20.2	173	174	EL PARAISO	519	0.353	8.108	0.372
3001999	CentralAmerica&Mexico	Zihuatanejo, Mexico	1985	7.56	20.2	43	47	LA UNION	517	0.069	4.979	1.282
4000016	Japan	Tohoku, Japan	2011	9.12	17.5	185	185	41207	349	0.217	27.973	52.657
4000025	Japan	Tohoku, Japan	2011	9.12	17.5	172	173	41216	428	0.569	28.356	20.682
4000026	Japan	Tohoku, Japan	2011	9.12	17.5	348	349	41301	216	0.204	24.940	44.939
4000087	Japan	Tohoku, Japan	2011	9.12	17.5	238	238	42205	360	0.151	16.139	34.142
4000092	Japan	Tohoku, Japan	2011	9.12	17.5	156	157	42211	186	0.352	55.496	146.840
4000101	Japan	Tohoku, Japan	2011	9.12	17.5	269	270	42221	401	0.057	11.651	33.661
4000106	Japan	Tohoku, Japan	2011	9.12	17.5	247	248	42226	508	0.401	34.022	36.557
4000108	Japan	Tohoku, Japan	2011	9.12	17.5	307	308	42301	262	0.448	39.298	55.737
4000113	Japan	Tohoku, Japan	2011	9.12	17.5	276	277	42308	411	0.240	24.392	45.738
4000115	Japan	Tohoku, Japan	2011	9.12	17.5	354	354	42310	208	0.155	18.502	40.419
4000124	Japan	Tohoku, Japan	2011	9.12	17.5	367	367	42319	356	0.070	14.077	75.685
4000158	Japan	Tohoku, Japan	2011	9.12	17.5	277	277	47241	634	0.038	8.968	30.841
4000161	Japan	Tohoku, Japan	2011	9.12	17.5	180	181	47245	398	0.309	20.405	39.740
4000163	Japan	Tohoku, Japan	2011	9.12	17.5	367	368	47253	332	0.033	11.697	25.076
4000183	Japan	Tohoku, Japan	2011	9.12	17.5	275	276	47351	634	0.073	6.440	27.476
4000224	Japan	Tohoku, Japan	2011	9.12	17.5	169	170	47590	364	0.353	55.866	171.140
4000244	Japan	Tohoku, Japan	2011	9.12	17.5	317	317	47648	249	0.146	16.956	38.056
4000321	Japan	Tohoku, Japan	2011	9.12	17.5	267	267	NISHISENBOKU	375	0.073	16.748	66.821
4000322	Japan	Tohoku, Japan	2011	9.12	17.5	250	250	NAKASEN	289	0.100	15.076	65.303
4000348	Japan	Tohoku, Japan	2011	9.12	17.5	319	319	CHOUSHI-C	201	0.153	17.768	45.355
4000359	Japan	Tohoku, Japan	2011	9.12	17.5	275	275	AIZUTAKADA	246	0.179	15.456	55.937
4000369	Japan	Tohoku, Japan	2011	9.12	17.5	218	219	FUKUSHIMA	532	0.275	23.083	76.869
4000427	Japan	Tohoku, Japan	2011	9.12	17.5	315	315	HASAKI2	244	0.208	22.867	84.620
4000457	Japan	Tohoku, Japan	2011	9.12	17.5	224	225	YAHABA	338	0.202	17.378	115.190
4000482	Japan	Tohoku, Japan	2011	9.12	17.5	428	429	FUJINO	388	0.098	11.764	44.593
4000521	Japan	Tohoku, Japan	2011	9.12	17.5	173	174	IWANUMA	203	0.265	36.188	259.010
4000557	Japan	Tohoku, Japan	2011	9.12	17.5	287	287	ASAHI	360	0.039	12.126	99.403
4000560	Japan	Tohoku, Japan	2011	9.12	17.5	334	334	KAMO	336	0.040	9.135	89.362
4000684	Japan	Tohoku, Japan	2011	9.12	17.5	249	250	NISHIKAWA-W	311	0.078	12.748	136.430
4000729	Japan	Tohoku, Japan	2011	9.12	17.5	377	377	KAWAUCHI	272	0.059	8.166	58.327
4000789	Japan	Tohoku, Japan	2011	9.12	17.5	170	171	HARAMACHI	535	0.591	39.561	59.952
4000809	Japan	Tohoku, Japan	2011	9.12	17.5	304	305	NANGOH	344	0.070	10.859	32.070
4000836	Japan	Tohoku, Japan	2011	9.12	17.5	384	385	SHIBUKAWA	277	0.091	13.942	35.341
4000842	Japan	Tohoku, Japan	2011	9.12	17.5	392	392	TAKASAKI	264	0.180	23.185	56.014
4001060	Japan	Tohoku, Japan	2011	9.12	17.5	173	174	TAIWA	579	0.458	36.693	318.950

4001066	Japan	Tohoku, Japan	2011	9.12	17.5	171	172	IWANUMA	235	0.406	64.556	258.170
4001098	Japan	Tohoku, Japan	2011	9.12	17.5	292	292	MURAKAMI	310	0.040	10.210	27.282
4001102	Japan	Tohoku, Japan	2011	9.12	17.5	297	298	KANOSE	228	0.083	13.221	42.523
4001158	Japan	Tohoku, Japan	2011	9.12	17.5	496	496	FUJINOMIYA	318	0.074	13.733	31.557
4001181	Japan	Tohoku, Japan	2011	9.12	17.5	311	312	UTSUNOMIYA	567	0.181	19.810	84.026
4001223	Japan	Tohoku, Japan	2011	9.12	17.5	443	443	OHTSUKI	300	0.067	10.901	51.233
4001239	Japan	Tohoku, Japan	2011	9.12	17.5	215	216	HIGASHINE	341	0.203	19.152	56.092
4001240	Japan	Tohoku, Japan	2011	9.12	17.5	249	250	NAKAMURA	282	0.082	12.824	34.956
4001245	Japan	Tohoku, Japan	2011	9.12	17.5	268	269	OGUNI	444	0.059	9.554	32.313
4022792	Japan	Tokachi-oki, Japan	2003	8.29	25.0	265	266	OOMA	302	0.062	6.434	9.836
4022796	Japan	Tokachi-oki, Japan	2003	8.29	25.0	243	244	ROKKASYO	386	0.052	4.449	8.466
4022853	Japan	Tokachi-oki, Japan	2003	8.29	25.0	222	223	OIWAKE	307	0.139	17.359	52.750
4022859	Japan	Tokachi-oki, Japan	2003	8.29	25.0	266	268	OOTAKI	259	0.079	10.312	21.766
4022901	Japan	Tokachi-oki, Japan	2003	8.29	25.0	237	238	BIEI-W	356	0.039	6.355	53.636
4022902	Japan	Tokachi-oki, Japan	2003	8.29	25.0	219	221	NAKAFURANO	538	0.119	9.906	51.537
4022907	Japan	Tokachi-oki, Japan	2003	8.29	25.0	148	151	AKAN-S	219	0.395	44.261	45.339
4022909	Japan	Tokachi-oki, Japan	2003	8.29	25.0	167	169	SHIBECHA-S	189	0.273	29.400	33.198
4022913	Japan	Tokachi-oki, Japan	2003	8.29	25.0	134	137	SHIRANUKA-S	230	0.412	67.653	48.336
4022977	Japan	Tokachi-oki, Japan	2003	8.29	25.0	235	236	KURIYAMA	241	0.125	22.239	39.802
4022988	Japan	Tokachi-oki, Japan	2003	8.29	25.0	191	192	RIKUBETSU	445	0.140	19.854	19.326
4022989	Japan	Tokachi-oki, Japan	2003	8.29	25.0	179	181	ASYORO-E	441	0.168	20.375	21.698
4022990	Japan	Tokachi-oki, Japan	2003	8.29	25.0	174	176	ASYORO-W	372	0.151	15.923	24.178
4028438	Japan	Tokachi-oki, Japan	2003	8.29	25.0	246	247	MUTSU	293	0.064	10.466	9.232
4028441	Japan	Tokachi-oki, Japan	2003	8.29	25.0	248	249	YOKOHAMA	374	0.052	6.931	7.892
4028544	Japan	Tokachi-oki, Japan	2003	8.29	25.0	276	277	AIDOMARI	302	0.108	8.900	6.252
4028557	Japan	Tokachi-oki, Japan	2003	8.29	25.0	136	139	KUSHIRO	214	0.325	41.874	23.411
4028559	Japan	Tokachi-oki, Japan	2003	8.29	25.0	175	177	SHIBECCHA	215	0.192	24.819	21.059
4028563	Japan	Tokachi-oki, Japan	2003	8.29	25.0	163	165	TSURUI	533	0.195	29.798	26.804
4028564	Japan	Tokachi-oki, Japan	2003	8.29	25.0	148	151	AKAN	219	0.358	43.541	33.961
4028567	Japan	Tokachi-oki, Japan	2003	8.29	25.0	153	155	FUTAMATA	422	0.255	26.779	23.144
4028568	Japan	Tokachi-oki, Japan	2003	8.29	25.0	190	192	RIKUBETSU	494	0.165	14.192	17.281
4028569	Japan	Tokachi-oki, Japan	2003	8.29	25.0	168	170	ASHORO	382	0.244	26.345	26.393
4028572	Japan	Tokachi-oki, Japan	2003	8.29	25.0	138	140	IKEDA	255	0.614	56.689	36.624
4028574	Japan	Tokachi-oki, Japan	2003	8.29	25.0	169	171	SHIHORO	324	0.118	20.055	28.876
4028581	Japan	Tokachi-oki, Japan	2003	8.29	25.0	181	183	HIDAKA	360	0.075	12.403	25.375
4028587	Japan	Tokachi-oki, Japan	2003	8.29	25.0	136	138	MITSUISHI	280	0.162	23.903	35.146
4028591	Japan	Tokachi-oki, Japan	2003	8.29	25.0	72	76	ERIMOMISAKI	294	0.119	17.251	24.010

4028592	Japan	Tokachi-oki, Japan	2003	8.29	25.0	74	78	MEGURO	600	0.183	17.688	22.442
4028603	Japan	Tokachi-oki, Japan	2003	8.29	25.0	194	195	HOBETSU	222	0.142	20.940	29.448
4028605	Japan	Tokachi-oki, Japan	2003	8.29	25.0	222	223	OIWAKE	351	0.107	16.867	20.631
4028609	Japan	Tokachi-oki, Japan	2003	8.29	25.0	257	259	NOBORIBETSU	431	0.084	7.122	11.933
4028612	Japan	Tokachi-oki, Japan	2003	8.29	25.0	266	267	OHTAKI	372	0.114	7.600	12.664
4028634	Japan	Tokachi-oki, Japan	2003	8.29	25.0	281	282	NANAE	341	0.034	4.345	8.934
4028662	Japan	Tokachi-oki, Japan	2003	8.29	25.0	246	248	SHIKOTSUKOHAN	313	0.129	10.932	14.586
4032535	Japan	Tokachi-oki, Japan	2003	8.29	25.0	227	228	41109	282	0.110	19.621	10.617
4032536	Japan	Tokachi-oki, Japan	2003	8.29	25.0	275	276	41110	282	0.049	8.575	12.223
4032539	Japan	Tokachi-oki, Japan	2003	8.29	25.0	232	234	51108	270	0.120	18.226	7.994
4032540	Japan	Tokachi-oki, Japan	2003	8.29	25.0	218	219	51109	357	0.096	11.709	8.701
4032552	Japan	Tokachi-oki, Japan	2003	8.29	25.0	108	111	51562	451	0.383	44.943	32.294
4032564	Japan	Tokachi-oki, Japan	2003	8.29	25.0	154	156	42109	348	0.258	24.724	27.029
4032570	Japan	Tokachi-oki, Japan	2003	8.29	25.0	243	244	42203	337	0.044	4.108	3.038
4032577	Japan	Tokachi-oki, Japan	2003	8.29	25.0	136	139	47418	260	0.283	36.834	16.445
4032588	Japan	Tokachi-oki, Japan	1968	8.26	7.9	298	298	muroran-s	254	0.174	26.558	16.232
4032589	Japan	Tokachi-oki, Japan	1968	8.26	7.9	249	249	aomori-s	186	0.212	37.259	19.748
4032590	Japan	Tokachi-oki, Japan	1968	8.26	7.9	186	186	hachinohe-s	231	0.196	34.632	24.699
4040369	Japan	Tohoku, Japan	2011	9.12	17.5	175	176	GN4	399	0.231	24.825	45.173
4040370	Japan	Tohoku, Japan	2011	9.12	17.5	175	176	GN5	399	0.244	22.089	37.006
4040371	Japan	Tohoku, Japan	2011	9.12	17.5	176	177	GS1	389	0.486	54.538	45.610
4040373	Japan	Tohoku, Japan	2011	9.12	17.5	176	177	GS3	389	0.259	28.020	41.973
5000314	NewZealand	Fiordland, NewZealand	2003	7.17	22.1	142	144	QTPS	350	0.109	6.891	0.937
5000323	NewZealand	Fiordland, NewZealand	2003	7.17	22.1	229	230	HDWS	210	0.073	6.034	1.816
5000324	NewZealand	Fiordland, NewZealand	2003	7.17	22.1	172	174	ICCS	210	0.023	4.484	2.655
5000328	NewZealand	Fiordland, NewZealand	2003	7.17	22.1	218	219	MECS	270	0.035	5.865	2.095
5000329	NewZealand	Fiordland, NewZealand	2003	7.17	22.1	116	118	MOSS	400	0.073	8.218	3.060
5000331	NewZealand	Fiordland, NewZealand	2003	7.17	22.1	142	144	QTPS	350	0.098	6.389	2.102
5000333	NewZealand	Fiordland, NewZealand	2003	7.17	22.1	68	72	TAFS	298	0.156	18.501	13.022
5000335	NewZealand	Fiordland, NewZealand	2003	7.17	22.1	188	190	WNPS	330	0.051	9.766	3.873
5000540	NewZealand	Tasman Sea, NewZealand	2004	7.09	5.9	180	180	RRKS	270	0.069	4.266	1.681
5001756	NewZealand	Fiordland, NewZealand	2009	7.81	20.9	181	182	GORS	400	0.034	4.033	2.391
5001758	NewZealand	Fiordland, NewZealand	2009	7.81	20.9	147	148	ICCS	210	0.024	5.416	2.115
5001764	NewZealand	Fiordland, NewZealand	2009	7.81	20.9	126	128	MOSS	400	0.037	5.936	4.163
5001767	NewZealand	Fiordland, NewZealand	2009	7.81	20.9	158	160	NZAS	210	0.025	2.186	1.865
5001769	NewZealand	Fiordland, NewZealand	2009	7.81	20.9	182	183	QTPS	350	0.041	4.110	2.007
5001770	NewZealand	Fiordland, NewZealand	2009	7.81	20.9	73	76	RRKS	270	0.134	7.518	6.758

5001772	NewZealand	Fiordland, NewZealand	2009	7.81	20.9	96	99	TAFS	298	0.082	26.223	14.506
6000319	SouthAmerica	Iquique, Chile	2014	8.15	20.1	170	171	GO01	415	0.351	10.728	4.950
6001018	SouthAmerica	South Coast, Peru	2001	8.41	28.8	307	308	MOQ1	542	0.285	27.670	5.307
6001019	SouthAmerica	South Coast, Peru	2001	8.41	28.8	411	412	TAC1	568	0.025	4.608	1.966
6001020	SouthAmerica	South Coast, Peru	2001	8.41	28.8	433	434	ARICA	432	0.246	22.648	28.776
6001021	SouthAmerica	South Coast, Peru	2001	8.41	28.8	433	434	ARICA CEMENTERIO	432	0.285	29.536	69.278
6001022	SouthAmerica	South Coast, Peru	2001	8.41	28.8	432	433	ARICA COSTANERA 2	389	0.304	26.362	11.071
6001023	SouthAmerica	South Coast, Peru	2001	8.41	28.8	491	491	CUYA MUNICIPALIDAD	415	0.140	9.104	5.160
6001024	SouthAmerica	South Coast, Peru	2001	8.41	28.8	522	522	PISAGUA RETEN DE CARABINEROS	605	0.038	3.717	1.652
6001025	SouthAmerica	South Coast, Peru	2001	8.41	28.8	452	453	POCONCHILE RETEN DE CARABINEROS (ETNA)	560	0.239	29.108	11.675
6001026	SouthAmerica	South Coast, Peru	2001	8.41	28.8	485	486	PUTRE RETEN DE CARABINEROS (SMA-1)	415	0.189	11.503	7.144
6001373	SouthAmerica	Iquique, Chile	2014	8.15	20.1	120	122	HMBCX	743	0.252	19.456	8.617
6001374	SouthAmerica	Iquique, Chile	2014	8.15	20.1	140	142	MNMCX	415	0.450	16.478	7.501
6001378	SouthAmerica	Iquique, Chile	2014	8.15	20.1	307	308	PB04	414	0.034	4.198	4.678
6001381	SouthAmerica	Iquique, Chile	2014	8.15	20.1	251	252	PB07	745	0.051	5.062	4.800
6001382	SouthAmerica	Iquique, Chile	2014	8.15	20.1	183	184	PB08	415	0.092	6.489	4.168
6001386	SouthAmerica	Iquique, Chile	2014	8.15	20.1	125	127	PB12	586	0.100	6.734	5.495
6001388	SouthAmerica	Iquique, Chile	2014	8.15	20.1	200	201	PB16	605	0.030	5.612	7.430
6001390	SouthAmerica	Iquique, Chile	2014	8.15	20.1	96	98	T03A	613	0.059	2.607	1.266
6001393	SouthAmerica	Iquique, Chile	2014	8.15	20.1	181	183	T13A	378	0.034	1.760	1.031
6001395	SouthAmerica	Iquique, Chile	2014	8.15	20.1	190	191	TAC1	568	0.072	5.999	4.413
6001396	SouthAmerica	Iquique, Chile	2014	8.15	20.1	192	193	TAC2	382	0.070	6.703	5.999
6001799	SouthAmerica	Maule, Chile (2844986)	2010	8.81	30.4	72	78	CONCEPCIÓN-Colegio San Pedro de la Paz	303	0.588	41.465	244.850
6001800	SouthAmerica	Maule, Chile (2844986)	2010	8.81	30.4	378	379	LRNA	574	0.272	31.081	18.883
6001802	SouthAmerica	Maule, Chile (2844986)	2010	8.81	30.4	371	373	SNJM	495	0.479	45.333	30.435
6001804	SouthAmerica	Maule, Chile (2844986)	2010	8.81	30.4	362	363	ANTU	622	0.253	23.494	41.527
6001805	SouthAmerica	Maule, Chile (2844986)	2010	8.81	30.4	383	384	LCON	619	0.200	30.090	44.578
6001806	SouthAmerica	Maule, Chile (2844986)	2010	8.81	30.4	351	352	CASB	315	0.304	29.350	89.032
6001807	SouthAmerica	Maule, Chile (2844986)	2010	8.81	30.4	322	324	MELP	598	0.735	36.958	198.370
6001808	SouthAmerica	Maule, Chile (2844986)	2010	8.81	30.4	393	394	OLMU	391	0.290	26.249	33.635
6001809	SouthAmerica	Maule, Chile (2844986)	2010	8.81	30.4	69	76	CONCEPCIÓN-Colegio Inmaculada Concepción	415	0.324	56.692	57.089
6001812	SouthAmerica	Maule, Chile (2844986)	2010	8.81	30.4	178	180	ANGOL HOSPITAL	358	0.807	36.139	40.582
6001813	SouthAmerica	Maule, Chile (2844986)	2010	8.81	30.4	109	113	CONT	278	0.632	64.706	17.237
6001815	SouthAmerica	Maule, Chile (2844986)	2010	8.81	30.4	206	209	CURICO HOSPITAL	514	0.463	35.589	38.290
6001816	SouthAmerica	Maule, Chile (2844986)	2010	8.81	30.4	172	175	HUAL	530	0.467	36.899	13.301
6001817	SouthAmerica	Maule, Chile (2844986)	2010	8.81	30.4	313	315	LLOLLEO LICEO SANTA TERESITA	345	0.466	30.799	6.145
6001818	SouthAmerica	Maule, Chile (2844986)	2010	8.81	30.4	269	270	MAT	379	0.320	36.778	23.585

6001825	SouthAmerica	Maule, Chile (2844986)	2010	8.81	30.4	145	148	TALCA COLEGIO INTEGRADO SAN PIO X	465	0.474	31.421	12.356
6001826	SouthAmerica	Maule, Chile (2844986)	2010	8.81	30.4	404	405	VALD	274	0.112	18.571	20.825
6002199	SouthAmerica	Iquique, Chile	2014	8.15	20.1	150	151	AP01	355	0.131	12.698	4.820
6002200	SouthAmerica	Iquique, Chile	2014	8.15	20.1	128	129	T07A	326	0.587	36.266	13.862
6002203	SouthAmerica	Iquique, Chile	2014	8.15	20.1	117	118	T10A	336	0.796	44.498	13.328
6002232	SouthAmerica	Coastal, Chile	2015	8.31	29.8	289	290	LMEL	415	0.039	2.199	2.283
6002237	SouthAmerica	Coastal, Chile	2015	8.31	29.8	377	378	AC04	605	0.053	6.545	13.895
6002239	SouthAmerica	Coastal, Chile	2015	8.31	29.8	320	321	BO01	421	0.062	13.979	14.990
6002241	SouthAmerica	Coastal, Chile	2015	8.31	29.8	122	126	CO03	704	0.699	30.104	16.988
6002252	SouthAmerica	Coastal, Chile	2015	8.31	29.8	259	261	MT01	479	0.042	3.960	4.291
6002253	SouthAmerica	Coastal, Chile	2015	8.31	29.8	222	224	MT05	571	0.124	9.109	6.356
6002254	SouthAmerica	Coastal, Chile	2015	8.31	29.8	255	256	MT09	479	0.066	6.034	4.895
6002260	SouthAmerica	Coastal, Chile	2015	8.31	29.8	234	235	VA05	485	0.065	6.590	5.819
6002262	SouthAmerica	Coastal, Chile	2015	8.31	29.8	175	177	GO04	605	0.292	34.386	13.757
6005357	SouthAmerica	Coastal, Chile	2015	8.31	29.8	191	193	C01O	447	0.168	10.191	8.550
6005358	SouthAmerica	Coastal, Chile	2015	8.31	29.8	232	234	C09O	754	0.177	6.064	5.025
6005360	SouthAmerica	Coastal, Chile	2015	8.31	29.8	117	121	C11O	632	0.744	34.974	14.082
6005391	SouthAmerica	Coastal, Chile	2015	8.31	29.8	166	169	V01A	607	0.044	3.073	2.289
6005392	SouthAmerica	Coastal, Chile	2015	8.31	29.8	164	166	V02A	596	0.109	4.014	3.073
6005393	SouthAmerica	Coastal, Chile	2015	8.31	29.8	166	169	V09A	212	0.056	5.547	3.250
7004744	Taiwan	Hualien, Taiwan (2944860)	2002	7.12	33.0	58	67	ILA007	432	0.232	20.571	7.053
7004755	Taiwan	Hualien, Taiwan (2944860)	2002	7.12	33.0	78	85	ILA028	218	0.169	30.070	12.227
7004767	Taiwan	Hualien, Taiwan (2944860)	2002	7.12	33.0	52	62	ILA050	627	0.271	13.201	2.058
7004772	Taiwan	Hualien, Taiwan (2944860)	2002	7.12	33.0	73	81	ILA055	266	0.168	27.110	13.264
7004776	Taiwan	Hualien, Taiwan (2944860)	2002	7.12	33.0	51	60	ILA062	597	0.199	16.005	3.889
7004777	Taiwan	Hualien, Taiwan (2944860)	2002	7.12	33.0	53	62	ILA065	566	0.183	9.451	2.383
7004778	Taiwan	Hualien, Taiwan (2944860)	2002	7.12	33.0	51	61	ILA066	478	0.178	11.482	2.635
7004779	Taiwan	Hualien, Taiwan (2944860)	2002	7.12	33.0	58	67	ILA068	364	0.174	20.053	7.877
7004830	Taiwan	Hualien, Taiwan (2944860)	2002	7.12	33.0	115	119	TAP022	181	0.191	32.767	8.629
1000040	Alaska	Fox Island, Alaska	2011	7.28	74.2	220	232	NIKH	635	0.030	2.474	0.486
1002186	Alaska	Fox Island, Alaska	2011	7.28	74.2	337	345	ADK	635	0.014	0.853	0.259
1002402	Alaska	Aleutian, Alaska	2014	7.96	103.8	305	322	ADK	635	0.016	1.360	0.964
1002800	Alaska	Iniskin, USA	2016	7.15	129.4	143	193	BRLK	665	0.107	2.357	0.633
1002801	Alaska	Iniskin, USA	2016	7.15	129.4	152	200	BRSE	665	0.032	2.155	1.172
1002808	Alaska	Iniskin, USA	2016	7.15	129.4	125	180	CNP	455	0.055	3.970	1.571
1002818	Alaska	Iniskin, USA	2016	7.15	129.4	243	275	FIRE	399	0.045	8.858	5.711
1002829	Alaska	Iniskin, USA	2016	7.15	129.4	101	164	HOM	455	0.206	11.850	2.850

1002865	Alaska	Iniskin, USA	2016	7.15	129.4	228	262	SWD	360	0.053	3.488	1.262
1002911	Alaska	Iniskin, USA	2016	7.15	129.4	78	151	O19K	453	0.015	1.747	0.910
1002922	Alaska	Iniskin, USA	2016	7.15	129.4	293	320	ARTY	750	0.310	10.559	1.494
1002947	Alaska	Iniskin, USA	2016	7.15	129.4	253	284	AK:Anchorage;Klatt Elem Sch	428	0.069	7.309	2.448
1002955	Alaska	Iniskin, USA	2016	7.15	129.4	253	284	AK:Anchorage;NOAA Weather Fac	328	0.124	12.526	3.574
1002957	Alaska	Iniskin, USA	2016	7.15	129.4	253	285	AK:Anchorage;FS 07 (new)	332	0.203	17.705	3.710
1002962	Alaska	Iniskin, USA	2016	7.15	129.4	216	251	AK:Kodiak;Fire Dept HQ	455	0.010	0.950	0.703
1002964	Alaska	Iniskin, USA	2016	7.15	129.4	220	255	AK:Kodiak Is;USCG AS Hanger 1	455	0.050	4.038	0.757
1002965	Alaska	Iniskin, USA	2016	7.15	129.4	241	274	Mt Kiliak, Eagle River, AK	455	0.093	7.019	1.373
1002977	Alaska	Iniskin, USA	2016	7.15	129.4	250	282	AK:Anchorage;Kincaid Prk	361	0.020	3.619	1.960
2000001	Cascadia	Olympia, USA	1949	6.70	57.2	19	60	OLY0	399	0.213	17.895	5.469
2000015	Cascadia	Nisqually, USA	2001	6.80	53.2	54	75	HAR	131	0.206	27.368	6.784
2000019	Cascadia	Nisqually, USA	2001	6.80	53.2	56	77	MAR	228	0.119	10.469	3.237
2000020	Cascadia	Nisqually, USA	2001	6.80	53.2	56	77	NOR	225	0.218	22.170	3.991
2000023	Cascadia	Nisqually, USA	2001	6.80	53.2	54	76	SDS	200	0.216	35.623	8.355
2000029	Cascadia	Nisqually, USA	2001	6.80	53.2	57	78	UNR	216	0.241	22.574	4.210
2000030	Cascadia	Nisqually, USA	2001	6.80	53.2	51	74	WEK	399	0.206	17.855	3.968
2000034	Cascadia	Nisqually, USA	2001	6.80	53.2	73	90	BRKS	228	0.097	10.227	2.952
2000036	Cascadia	Nisqually, USA	2001	6.80	53.2	81	97	EARN	506	0.058	5.575	2.394
2000037	Cascadia	Nisqually, USA	2001	6.80	53.2	71	89	ELW	438	0.055	3.699	1.278
2000041	Cascadia	Nisqually, USA	2001	6.80	53.2	51	73	HOLY	348	0.092	7.652	3.013
2000042	Cascadia	Nisqually, USA	2001	6.80	53.2	179	187	KEEL	233	0.014	2.117	0.657
2000049	Cascadia	Nisqually, USA	2001	6.80	53.2	80	96	LEOT	420	0.065	5.770	2.342
2000052	Cascadia	Nisqually, USA	2001	6.80	53.2	10	54	MURR	521	0.061	5.081	1.893
2000053	Cascadia	Nisqually, USA	2001	6.80	53.2	67	86	NOWS	275	0.080	10.305	4.129
2000054	Cascadia	Nisqually, USA	2001	6.80	53.2	30	61	PCEP	375	0.195	13.117	2.509
2000055	Cascadia	Nisqually, USA	2001	6.80	53.2	26	59	PCFR	437	0.129	11.789	2.457
2000062	Cascadia	Nisqually, USA	2001	6.80	53.2	166	175	ROSS	333	0.019	1.260	0.393
2000063	Cascadia	Nisqually, USA	2001	6.80	53.2	69	87	RWW	455	0.067	5.720	1.840
2000065	Cascadia	Nisqually, USA	2001	6.80	53.2	55	76	SP2	453	0.256	16.530	2.736
2000066	Cascadia	Nisqually, USA	2001	6.80	53.2	26	59	TBPA	230	0.063	10.136	4.005
2000067	Cascadia	Nisqually, USA	2001	6.80	53.2	51	74	TKCO	292	0.218	16.653	3.269
2000071	Cascadia	Nisqually, USA	2001	6.80	53.2	91	105	BEVT	632	0.050	4.235	1.722
2000072	Cascadia	Nisqually, USA	2001	6.80	53.2	182	190	CSO	334	0.012	0.713	0.146
2000080	Cascadia	Nisqually, USA	2001	6.80	53.2	21	57	2101	186	0.205	17.457	3.294
2000081	Cascadia	Nisqually, USA	2001	6.80	53.2	8	54	2130	399	0.140	7.713	1.662
2000089	Cascadia	Nisqually, USA	2001	6.80	53.2	109	121	WA: Pt Townsend;Ft Worden St Pk	386	0.044	3.696	0.903

2000093	Cascadia	Nisqually, USA	2001	6.80	53.2	151	160	7033	294	0.031	2.408	0.461
2000097	Cascadia	Nisqually, USA	2001	6.80	53.2	94	108	7039	358	0.018	1.277	0.605
2000098	Cascadia	Nisqually, USA	2001	6.80	53.2	78	94	7040	285	0.055	4.141	1.021
2000888	Cascadia	Ferndale, USA	2010	6.55	21.7	95	97	89146	665	0.014	1.205	0.423
2000889	Cascadia	Ferndale, USA	2010	6.55	21.7	47	52	89255	362	0.144	11.305	2.388
2000890	Cascadia	Ferndale, USA	2010	6.55	21.7	47	52	89486	362	0.131	11.680	2.342
2000891	Cascadia	Ferndale, USA	2010	6.55	21.7	49	53	89509	285	0.242	24.152	6.620
2000893	Cascadia	Ferndale, USA	2010	6.55	21.7	49	53	89781	362	0.297	23.682	6.111
2000897	Cascadia	Ferndale, USA	2010	6.55	21.7	36	42	KCT	427	0.089	16.231	5.322
2000899	Cascadia	Ferndale, USA	2010	6.55	21.7	37	43	CA: Ferndale;FS	223	0.330	34.769	6.989
2000900	Cascadia	Ferndale, USA	2010	6.55	21.7	57	61	CA: Arcata;Humboldt State Univ	362	0.072	5.894	1.841
2000902	Cascadia	Ferndale, USA	2010	6.55	21.7	38	44	1584	427	0.082	9.974	2.885
2000903	Cascadia	Ferndale, USA	2010	6.55	21.7	40	45	CA: Loleta;FS	418	0.177	23.238	6.426
2000904	Cascadia	Ferndale, USA	2010	6.55	21.7	31	38	1725	427	0.292	32.394	8.338
2000905	Cascadia	Ferndale, USA	2010	6.55	21.7	47	51	1746	362	0.130	12.468	2.675
2001631	Cascadia	Ferndale, USA	2010	6.55	21.7	36	42	KCT	427	0.089	16.171	5.383
2001636	Cascadia	Ferndale, USA	2010	6.55	21.7	117	119	KRMB	565	0.011	0.807	0.406
2001983	Cascadia	Nisqually, USA	2001	6.80	53.2	74	91	WA: Wynoochee Dam, Abutment	358	0.017	0.910	0.186
3000001	CentralAmerica&Mexico	Guaymas, Mexico	1988	6.60	60.0	73	94	2841	517	0.100	7.868	1.701
3000098	CentralAmerica&Mexico	Offshore Chiapas, Mexico (38)	1992	6.51	79.0	111	136	3567	568	0.125	4.427	0.993
3000099	CentralAmerica&Mexico	Offshore Chiapas, Mexico (38)	1992	6.51	79.0	89	119	3568	519	0.020	2.673	1.265
3000100	CentralAmerica&Mexico	Offshore Chiapas, Mexico (38)	1992	6.51	79.0	91	120	3570	429	0.062	5.587	1.789
3000101	CentralAmerica&Mexico	Offshore Chiapas, Mexico (38)	1992	6.51	79.0	62	100	2857	519	0.038	4.093	1.121
3000102	CentralAmerica&Mexico	Offshore Chiapas, Mexico (38)	1992	6.51	79.0	65	103	2893	517	0.020	2.643	0.619
3000103	CentralAmerica&Mexico	Offshore Chiapas, Mexico (38)	1992	6.51	79.0	57	97	2894	586	0.097	10.450	2.423
3000104	CentralAmerica&Mexico	Offshore Chiapas, Mexico (38)	1992	6.51	79.0	40	89	2897	429	0.098	8.925	1.565
3000105	CentralAmerica&Mexico	Offshore Chiapas, Mexico (38)	1992	6.51	79.0	40	89	2898	519	0.053	6.256	1.612
3000106	CentralAmerica&Mexico	Offshore Chiapas, Mexico (38)	1992	6.51	79.0	51	94	3563	568	0.052	5.241	1.108
3000107	CentralAmerica&Mexico	Offshore Chiapas, Mexico (38)	1992	6.51	79.0	23	82	448	382	0.102	8.848	1.821
3000185	CentralAmerica&Mexico	Ometepec, Guerrero, Mexico (69)	1982	7.31	72.8	40	83	2747	519	0.193	26.453	9.434
3000191	CentralAmerica&Mexico	Chinandega, Nicaragua	1978	6.54	70.0	46	84	3547	281	0.062	2.530	0.249
3000192	CentralAmerica&Mexico	Chinandega, Nicaragua	1978	6.54	70.0	15	72	3548	382	0.144	4.326	0.351
3001283	CentralAmerica&Mexico	Guaymas, Mexico	1988	6.60	60.0	73	94	1	517	0.098	7.834	1.267
3001286	CentralAmerica&Mexico	Guaymas, Mexico	1988	6.60	60.0	39	71	0	519	0.050	3.559	0.802
3001293	CentralAmerica&Mexico	Guerrero, Mexico	2014	7.32	40.8	173	178	643	429	0.051	3.980	1.264
3001294	CentralAmerica&Mexico	Guerrero, Mexico	2014	7.32	40.8	125	131	644	517	0.074	4.543	1.726
3001296	CentralAmerica&Mexico	Guerrero, Mexico	2014	7.32	40.8	150	155	646	517	0.059	4.378	1.540

3001303	CentralAmerica&Mexico	Guerrero, Mexico	2014	7.32	40.8	131	137	2062	429	0.084	9.700	3.426
3001306	CentralAmerica&Mexico	Guerrero, Mexico	2014	7.32	40.8	176	180	3115	568	0.049	3.647	1.067
3001307	CentralAmerica&Mexico	Guerrero, Mexico	2014	7.32	40.8	208	212	3116	568	0.039	2.465	0.497
3001311	CentralAmerica&Mexico	Guerrero, Mexico	2014	7.32	40.8	140	146	3295	281	0.084	7.357	2.136
3001313	CentralAmerica&Mexico	Guerrero, Mexico	2014	7.32	40.8	199	203	3687	382	0.056	3.905	1.222
3001314	CentralAmerica&Mexico	Guerrero, Mexico	2014	7.32	40.8	173	178	6357	586	0.040	3.308	1.046
3001482	CentralAmerica&Mexico	Michoacan, Mexico	1997	7.15	35.0	273	275	ATYC	429	0.010	0.455	0.268
3001493	CentralAmerica&Mexico	Michoacan, Mexico	1997	7.15	35.0	107	112	LA UNION	517	0.078	8.363	2.319
3001494	CentralAmerica&Mexico	Michoacan, Mexico	1997	7.15	35.0	65	74	VILE	429	0.102	8.569	3.572
3001522	CentralAmerica&Mexico	Michoacan, Mexico	1997	6.51	60.0	77	97	LA UNION	517	0.046	3.504	0.603
3001523	CentralAmerica&Mexico	Michoacan, Mexico	1997	6.51	60.0	92	110	VILE	429	0.029	2.337	0.384
3001576	CentralAmerica&Mexico	Puebla, Mexico	1999	6.96	63.0	272	279	POZU	517	0.021	0.701	0.285
3001587	CentralAmerica&Mexico	Oaxaca, Mexico	1999	7.46	40.0	229	232	COPL	460	0.027	1.727	0.858
4007219	Japan	Miyagi, Japan	2011	7.15	66.4	186	198	NAKASEN	289	0.112	6.769	2.697
4007388	Japan	Miyagi, Japan	2011	7.15	66.4	133	148	NARUKO	399	0.083	4.102	1.781
4016832	Japan	Miyagi, Japan	2011	7.15	66.4	297	305	CHOHSHI	478	0.011	1.171	0.694
4022455	Japan	South Sanriku, Japan	2003	7.03	65.2	233	242	AJIGASAWA	298	0.011	3.529	2.078
4027357	Japan	Geiyo, Japan	2001	6.83	45.9	33	57	HIGASHIHIROSHIMA	349	0.274	9.127	1.313
4027364	Japan	Geiyo, Japan	2001	6.83	45.9	19	50	KURE	263	0.406	20.100	2.532
4028046	Japan	South Sanriku, Japan	2003	7.03	65.2	199	209	NOSHIRO	218	0.018	5.276	2.723
4028050	Japan	South Sanriku, Japan	2003	7.03	65.2	189	200	OGA	446	0.012	2.823	1.821
4028080	Japan	South Sanriku, Japan	2003	7.03	65.2	223	232	AOMORI	182	0.019	3.871	1.615
4028405	Japan	South Sanriku, Japan	2003	7.03	65.2	161	174	SAKATA	190	0.023	11.084	7.262
4032457	Japan	Kushiro-oki, Japan	1993	7.59	107.2	192	220	D4F	345	0.012	3.123	2.783
4032458	Japan	Kushiro-oki, Japan	1993	7.59	107.2	126	165	47409	414	0.021	2.589	4.195
4032459	Japan	Kushiro-oki, Japan	1993	7.59	107.2	252	274	47412	293	0.030	7.455	3.829
4032460	Japan	Kushiro-oki, Japan	1993	7.59	107.2	11	108	47418	260	0.968	66.404	7.361
4032461	Japan	Kushiro-oki, Japan	1993	7.59	107.2	107	151	47420	262	0.201	11.405	3.967
4032462	Japan	Kushiro-oki, Japan	1993	7.59	107.2	231	255	47424	256	0.116	17.576	10.324
4032463	Japan	Kushiro-oki, Japan	1993	7.59	107.2	157	190	47426	394	0.268	25.230	12.272
4032464	Japan	Kushiro-oki, Japan	1993	7.59	107.2	324	341	47430	369	0.038	4.308	1.285
4032477	Japan	Hokkaido.East, Japan	1994	8.28	27.5	257	258	47409	414	0.043	6.843	10.265
4032479	Japan	Hokkaido.East, Japan	1994	8.28	27.5	262	263	47418	260	0.484	51.822	29.839
4032480	Japan	Hokkaido.East, Japan	1994	8.28	27.5	157	159	47420	262	0.388	29.825	33.849
4032521	Japan	Geiyo, Japan	2001	6.83	45.9	22	51	973	396	0.228	12.167	1.507
4032616	Japan	ChibaEastoff, Japan	1987	6.53	50.4	111	122	hitachinaka-f	333	0.040	2.959	0.615
4032628	Japan	Kushiro-oki, Japan	1993	7.59	107.2	104	149	hanasaki-f	321	0.163	7.759	3.853

4032630	Japan	Kushiro-oki, Japan	1993	7.59	107.2	157	190	urakawa-s	400	0.248	18.742	6.388
4032632	Japan	Kushiro-oki, Japan	1993	7.59	107.2	290	309	muroran-g	254	0.142	8.846	2.786
4032652	Japan	Hokkaido.East.off	1994	8.28	27.5	158	161	hanasaki-f	321	0.393	29.121	31.991
5000042	NewZealand	Te Anau, NewZealand	1988	6.69	60.0	56	82	TAFS	298	0.098	9.446	2.688
5000043	NewZealand	Te Anau, NewZealand	1988	6.69	60.0	162	173	WNPS	330	0.034	4.330	1.431
5000049	NewZealand	Weber, NewZealand	1990	6.24	23.0	58	62	032A	495	0.168	11.132	1.199
5000050	NewZealand	Weber, NewZealand	1990	6.24	23.0	22	32	033A	367	0.223	13.652	1.676
5000052	NewZealand	Weber, NewZealand	1990	6.24	23.0	30	38	120A	290	0.182	14.806	1.855
5000128	NewZealand	Ormond, NewZealand	1993	6.30	39.0	16	42	GISS	138	0.201	14.439	1.740
5000133	NewZealand	Ormond, NewZealand	1993	6.30	39.0	17	43	016A	480	0.156	10.449	1.288
5000134	NewZealand	Ormond, NewZealand	1993	6.30	39.0	16	42	GISS	138	0.187	12.205	1.535
5001478	NewZealand	Gisborne, NewZealand	2007	6.65	33.0	51	61	GISS	138	0.213	26.713	3.610
5001480	NewZealand	Gisborne, NewZealand	2007	6.65	33.0	255	257	DVHS	360	0.010	0.852	0.254
5001482	NewZealand	Gisborne, NewZealand	2007	6.65	33.0	294	296	FAHS	270	0.018	1.092	0.722
5001484	NewZealand	Gisborne, NewZealand	2007	6.65	33.0	51	61	GISS	138	0.264	22.469	4.686
5001485	NewZealand	Gisborne, NewZealand	2007	6.65	33.0	61	69	GWTS	245	0.146	15.992	3.637
5001486	NewZealand	Gisborne, NewZealand	2007	6.65	33.0	168	172	HCDS	182	0.015	1.979	0.831
5001487	NewZealand	Gisborne, NewZealand	2007	6.65	33.0	167	170	HNPS	425	0.015	1.432	1.436
5001488	NewZealand	Gisborne, NewZealand	2007	6.65	33.0	183	186	KAFS	220	0.022	2.357	0.578
5001489	NewZealand	Gisborne, NewZealand	2007	6.65	33.0	188	192	KFHS	760	0.018	0.932	0.320
5001495	NewZealand	Gisborne, NewZealand	2007	6.65	33.0	155	158	NAMS	268	0.030	1.486	0.634
5001497	NewZealand	Gisborne, NewZealand	2007	6.65	33.0	157	161	NCHS	200	0.026	1.888	0.874
5001500	NewZealand	Gisborne, NewZealand	2007	6.65	33.0	146	150	OPCS	210	0.028	2.360	0.447
5001505	NewZealand	Gisborne, NewZealand	2007	6.65	33.0	197	200	RPCS	210	0.012	2.268	0.911
5001506	NewZealand	Gisborne, NewZealand	2007	6.65	33.0	157	160	RUAS	270	0.020	2.259	0.539
5001507	NewZealand	Gisborne, NewZealand	2007	6.65	33.0	61	69	TBAS	210	0.150	18.887	3.484
5001509	NewZealand	Gisborne, NewZealand	2007	6.65	33.0	141	144	TDHS	210	0.017	1.520	0.441
5001515	NewZealand	Gisborne, NewZealand	2007	6.65	33.0	220	223	WAKS	555	0.018	0.821	0.198
5001519	NewZealand	Gisborne, NewZealand	2007	6.65	33.0	170	173	WKHS	210	0.019	1.425	0.231
5003312	NewZealand	Eketahuna, NewZealand	2014	6.31	34.2	31	46	WDPS	270	0.211	12.709	1.793
5003313	NewZealand	Eketahuna, NewZealand	2014	6.31	34.2	37	50	PNMS	210	0.149	12.003	2.739
5003314	NewZealand	Eketahuna, NewZealand	2014	6.31	34.2	37	51	PNBS	270	0.119	9.734	2.173
5003316	NewZealand	Eketahuna, NewZealand	2014	6.31	34.2	43	55	CPFS	350	0.159	10.781	2.119
5003320	NewZealand	Eketahuna, NewZealand	2014	6.31	34.2	52	62	FAHS	270	0.140	10.206	1.794
5003329	NewZealand	Eketahuna, NewZealand	2014	6.31	34.2	79	87	PAPS	200	0.159	10.421	1.259
5003337	NewZealand	Eketahuna, NewZealand	2014	6.31	34.2	100	106	NBSS	190	0.102	6.277	0.740
5003989	NewZealand	SE of St Arnaud, NewZealand	2015	6.05	51.5	16	55	MOLS	700	0.305	15.679	1.963

6000989	SouthAmerica	Punitaqui, Chile	1997	7.09	68.0	68	96	ILLAPEL COMISARIA	486	0.364	13.107	3.937
6000991	SouthAmerica	Punitaqui, Chile	1997	7.09	68.0	277	286	STGO CENTRO	489	0.018	1.455	0.407
6001141	SouthAmerica	Tarapaca, Chile	2005	7.78	110.0	245	269	TAC1	568	0.099	6.292	3.433
6001142	SouthAmerica	Tarapaca, Chile	2005	7.78	110.0	246	270	TAC2	382	0.117	7.704	3.400
6001143	SouthAmerica	Tarapaca, Chile	2005	7.78	110.0	203	231	ARICA CEMENTERIO	432	0.170	13.415	29.278
6001145	SouthAmerica	Tarapaca, Chile	2005	7.78	110.0	205	232	ARICA COSTANERA 2	389	0.158	16.814	19.231
6001146	SouthAmerica	Tarapaca, Chile	2005	7.78	110.0	272	294	CALAMA HOSPITAL	745	0.071	3.240	2.327
6001147	SouthAmerica	Tarapaca, Chile	2005	7.78	110.0	135	174	CUYA MUNICIPALIDAD	415	0.429	19.887	13.369
6001148	SouthAmerica	Tarapaca, Chile	2005	7.78	110.0	175	207	EL LOA ADUANA (SMA-1)	586	0.109	8.347	17.707
6001150	SouthAmerica	Tarapaca, Chile	2005	7.78	110.0	92	144	IQUIQUE IDIEM	605	0.201	16.327	4.849
6001151	SouthAmerica	Tarapaca, Chile	2005	7.78	110.0	93	144	IQUIQUE PLAZA	650	0.256	17.172	47.407
6001154	SouthAmerica	Tarapaca, Chile	2005	7.78	110.0	109	155	PISAGUA RETEN DE CARABINEROS	605	0.349	16.546	29.110
6001155	SouthAmerica	Tarapaca, Chile	2005	7.78	110.0	194	223	POCONCHILE RETEN DE CARABINEROS (ETNA)	560	0.356	15.583	9.167
6001156	SouthAmerica	Tarapaca, Chile	2005	7.78	110.0	206	234	PUTRE RETEN DE CARABINEROS (SMA-1)	415	0.105	6.936	3.627
6001242	SouthAmerica	Antofagasta, Chile	2007	6.74	45.2	30	54	MEJILLONES HOSPITAL	745	0.097	15.002	8.528
6001243	SouthAmerica	Antofagasta, Chile	2007	6.74	45.2	26	52	MEJILLONE	745	0.150	16.916	9.378
6001246	SouthAmerica	Antofagasta, Chile	2007	6.74	45.2	96	106	TOCOPILLA PUERTO (SOQUIMICH)	605	0.071	4.475	0.931
6001504	SouthAmerica	San Antonio , Columbia	1997	6.77	206.0	208	293	CANDE	517	0.011	0.550	0.208
6001509	SouthAmerica	San Antonio , Columbia	1997	6.77	206.0	234	312	CBORD	517	0.016	1.183	0.250
6001512	SouthAmerica	San Antonio , Columbia	1997	6.77	206.0	79	221	CCALA	519	0.014	0.602	0.193
6001530	SouthAmerica	San Antonio , Columbia	1997	6.77	206.0	187	278	CPENS	519	0.011	0.541	0.105
6001535	SouthAmerica	San Antonio , Columbia	1997	6.77	206.0	179	273	CPOP2	519	0.013	1.260	0.283
6001540	SouthAmerica	San Antonio , Columbia	1997	6.77	206.0	86	223	CROLD	517	0.016	0.348	0.101
6001541	SouthAmerica	San Antonio , Columbia	1997	6.77	206.0	193	283	CROSA	568	0.043	2.709	0.495
6001546	SouthAmerica	San Antonio , Columbia	1997	6.77	206.0	120	238	CSTRC	517	0.036	3.092	0.409
6001549	SouthAmerica	San Antonio , Columbia	1997	6.77	206.0	115	236	CTORI	519	0.010	0.680	0.219
6001550	SouthAmerica	San Antonio , Columbia	1997	6.77	206.0	82	222	CTRUJ	517	0.015	0.794	0.174
6001551	SouthAmerica	San Antonio , Columbia	1997	6.77	206.0	235	312	CTUTU	425	0.016	0.725	0.193
6001680	SouthAmerica	LaVega, Columbia	2012	7.27	155.2	124	199	CPAS2	517	0.013	1.891	0.867
6001684	SouthAmerica	LaVega, Columbia	2012	7.27	155.2	67	169	CPOP3	425	0.015	2.249	1.353
6001687	SouthAmerica	LaVega, Columbia	2012	7.27	155.2	196	250	CRICA	519	0.047	2.052	0.212
6001714	SouthAmerica	Pasto, Columbia	2013	7.01	144.2	27	147	CPAS3	429	0.017	2.082	0.741
6001716	SouthAmerica	Pasto, Columbia	2013	7.01	144.2	30	147	CPAS5	517	0.012	1.745	0.469
6001717	SouthAmerica	Pasto, Columbia	2013	7.01	144.2	29	147	CPAS6	517	0.019	2.032	0.592
6001723	SouthAmerica	Pasto, Columbia	2013	7.01	144.2	63	157	CRICA	519	0.034	1.642	0.415
6001732	SouthAmerica	Pasto, Columbia	2013	7.01	144.2	280	315	RAC02	382	0.027	3.604	0.633
6003444	SouthAmerica	Antofagasta, Chile	2007	6.74	45.2	70	83	PB04	414	0.121	2.149	0.463

6003445	SouthAmerica	Antofagasta, Chile	2007	6.74	45.2	12	47	PB05	745	0.087	2.210	0.490
6003446	SouthAmerica	Antofagasta, Chile	2007	6.74	45.2	70	84	PB06	489	0.090	2.165	0.289
6003926	SouthAmerica	Araucania, Chile (3316325)	2011	6.56	128.7	199	237	PB08	415	0.013	0.845	0.299
7005060	Taiwan	Hualien, Taiwan (7418598)	2004	6.59	88.0	243	258	CHY103	224	0.022	1.546	0.479
7005081	Taiwan	Hualien, Taiwan (7418598)	2004	6.59	88.0	128	155	HWA012	410	0.028	1.723	0.419
7005096	Taiwan	Hualien, Taiwan (7418598)	2004	6.59	88.0	135	162	HWA029	597	0.031	1.328	0.270
7005162	Taiwan	Hualien, Taiwan (7418598)	2004	6.59	88.0	95	130	ILA060	444	0.071	3.753	0.419
7005221	Taiwan	Hualien, Taiwan (7418598)	2004	6.59	88.0	138	163	TAP022	181	0.183	8.327	1.039
7005842	Taiwan	Pingtung, Taiwan	2006	7.02	44.1	204	209	CHY002	230	0.023	1.202	0.408
7005904	Taiwan	Pingtung, Taiwan	2006	7.02	44.1	166	172	CHY087	508	0.027	1.142	0.345
7005932	Taiwan	Pingtung, Taiwan	2006	7.02	44.1	130	137	CHY125	272	0.021	2.367	1.432
7005934	Taiwan	Pingtung, Taiwan	2006	7.02	44.1	22	49	HEN	198	0.189	30.198	8.579
7006061	Taiwan	Pingtung, Taiwan	2006	7.02	44.1	91	101	KAU060	246	0.045	2.620	0.682
7006078	Taiwan	Pingtung, Taiwan	2006	7.02	44.1	18	48	KAU082	493	0.224	26.744	12.682
7006163	Taiwan	Pingtung, Taiwan	2006	7.02	44.1	219	224	TCU079	354	0.015	0.889	0.197
7006328	Taiwan	Pingtung, Taiwan	2006	6.94	33.8	97	103	CHY065	223	0.086	5.288	2.127
7006331	Taiwan	Pingtung, Taiwan	2006	6.94	33.8	108	113	CHY068	196	0.061	3.368	0.880
7006355	Taiwan	Pingtung, Taiwan	2006	6.94	33.8	133	137	CHY100	344	0.074	5.052	1.431
7006358	Taiwan	Pingtung, Taiwan	2006	6.94	33.8	186	189	CHY103	224	0.050	2.929	1.091
7006378	Taiwan	Pingtung, Taiwan	2006	6.94	33.8	35	49	HEN	198	0.223	37.308	12.811
7006501	Taiwan	Pingtung, Taiwan	2006	6.94	33.8	48	58	KAU043	378	0.177	20.078	6.353
7006502	Taiwan	Pingtung, Taiwan	2006	6.94	33.8	47	58	KAU044	216	0.082	10.571	5.742
7006504	Taiwan	Pingtung, Taiwan	2006	6.94	33.8	35	49	KAU046	198	0.220	38.291	13.759
7006518	Taiwan	Pingtung, Taiwan	2006	6.94	33.8	67	75	KAU062	196	0.109	9.959	2.307
7006531	Taiwan	Pingtung, Taiwan	2006	6.94	33.8	32	46	KAU080	399	0.288	30.064	10.707
7006532	Taiwan	Pingtung, Taiwan	2006	6.94	33.8	35	49	KAU081	381	0.236	31.562	12.497
7006533	Taiwan	Pingtung, Taiwan	2006	6.94	33.8	35	49	KAU082	493	0.185	36.293	14.502
7006538	Taiwan	Pingtung, Taiwan	2006	6.94	33.8	50	60	KAU089	191	0.073	8.432	4.019
7006610	Taiwan	Pingtung, Taiwan	2006	6.94	33.8	293	295	TCU047	523	0.017	0.733	0.270
7006685	Taiwan	Pingtung, Taiwan	2006	6.94	33.8	221	223	TCU148	514	0.020	0.992	0.454

The Pacific Earthquake Engineering Research Center (PEER) is a multi-institutional research and education center with headquarters at the University of California, Berkeley. Investigators from over 20 universities, several consulting companies, and researchers at various state and federal government agencies contribute to research programs focused on performance-based earthquake engineering.

These research programs aim to identify and reduce the risks from major earthquakes to life safety and to the economy by including research in a wide variety of disciplines including structural and geotechnical engineering, geology/seismology, lifelines, transportation, architecture, economics, risk management, and public policy.

PEER is supported by federal, state, local, and regional agencies, together with industry partners.

PEER Core Institutions

University of California, Berkeley (Lead Institution)
California Institute of Technology
Oregon State University
Stanford University
University of California, Davis
University of California, Irvine
University of California, Los Angeles
University of California, San Diego
University of Nevada, Reno
University of Southern California
University of Washington

Pacific Earthquake Engineering Research Center
University of California, Berkeley
325 Davis Hall, Mail Code 1792
Berkeley, CA 94720-1792
Tel: 510-642-3437
Email: peer_center@berkeley.edu

ISSN 2770-8314
https://doi.org/10.55461/ZKVV5271